UNIVERSITY OF OKLAHOMA

GRADUATE COLLEGE

UNDERSTANDING THE LOWERMOST STRATOSPHERE IN CURRENT AND FUTURE CLIMATES: COMPOSITION, DEFINITION, AND TROPOPAUSE-OVERSHOOTING CONVECTION

A DISSERTATION

SUBMITTED TO THE GRADUATE FACULTY

in partial fulfillment of the requirements for the

degree of

Doctor of Philosophy

By

EMILY NICOLE TINNEY
Norman, Oklahoma
2023

UNDERSTANDING THE LOWERMOST STRATOSPHERE IN CURRENT AND FUTURE CLIMATES: COMPOSITION, DEFINITION, AND TROPOPAUSE-OVERSHOOTING CONVECTION

A DISSERTATION APPROVED FOR THE
SCHOOL OF METEOROLOGY

BY THE COMMITTEE CONSISTING OF

Dr. Cameron Homeyer, Chair

Dr. Elinor Martin

Dr. James Ruppert

Dr. Megan Elwood Madden

Acknowledgments

The past five and a half years I've spent at the University of Oklahoma have been the most challenging and rewarding of my entire life. To think that this chapter is coming to a close is mind-boggling and surreal. As I sit here and reflect upon this journey, I am overwhelmed at the idea of trying to adequately thank all of the people who have helped me along the way, but I will do my best. Please note that these acknowledgements are in no particular order and they are by no means an exhaustive list.

There are very few people who have had as big of an impact on my life as my advisor and "science dad", Dr. Cameron Homeyer. It really is impossible to put into words how much I owe to your encouragement, guidance, and belief in my abilities. From our very first meeting at Visiting Students Weekend, your passion for your science and your students have inspired me. As a person who struggles with self-confidence, I cannot emphasize how helpful it has been to never doubt that you believe in me. I have never once felt that I've had to work to earn your respect or approval, so instead I've just been able to work on being the best scientist I can be. I am so incredibly thankful for you supporting my scientific curiosities that largely shaped how my dissertation turned out to be. Most importantly, outside of your *record-breakingly* successful scientific career, you are an amazing human being. Your dedication to your beautiful family, your community, and your values is inspiring. Learning from you has been the honor of a lifetime.

Throughout my academic journey, I have had a number of other mentors, teachers, and supporters that were instrumental in shaping me into the scientist I am today. Thank you to my PhD Committee, Dr. Elinor Martin, Dr. James Ruppert, and Dr. Megan Elwood-Madden for your encouragement, advice, and support throughout this process. Thank you Dr. John Allen for teaching me the foundations of being a researcher and for encouraging me to pursue opportunities that always felt so far out of reach (like attending graduate school at OU, for instance). Thank you Dr. Jimmy Correia for your ongoing mentorship and for teaching me the most important rules of all. Thank you to my CMU professors, Dr. Marty Baxter, Dr. Daria Kluver, Dr.

Richard Mower, and Dr. John Allen for setting me up for success in this field. Thank you to the many other mentors I have had along the way, especially Dr. Daphne LaDue, Dr. Amanda Kis, Dr. Marcela Loría-Salazar, Dr. Naoko Sakaeda, and Dr. Steven Cavallo. Thank you Mr. Roger Lawrence for instilling in me a love for math and for teaching me that: "A.I.E. – Attitude Is Everything" more than a decade ago. Recently, I was also able to experience being a mentor for the first time thanks to the NWC REU program. To my wonderful student, Lexy Elizalde: watching your skills, curiosity, and confidence grow throughout the program gave me a sense of pride that I had not ever felt before. Working with you has truly charted my path moving forward, as I know that my future career will be fulfilling as long as I get to mentor students like you. Thank you.

My graduate school journey has been profoundly shaped by the incredible individuals who have shared it with me. Specifically, I want to thank past and present members of the CCC Research Group: Tao, Thea, Elisa, Amanda, Andrea, Hannah, and Cole. Their unwavering support and valuable guidance have been pillars of strength for me throughout the past 5.5 years. I want to extend a special acknowledgement to Andrea Gordon, who joined the CCC group at the same time as me. From laying on the office floor in the evenings, to working over cups of coffee and relaxing over baskets of tacos, to traveling across the world together, your friendship has been so incredibly dear to me. I also must express my gratitude to my office mates of 5700 — Tripp, Melanie, Bryony, Margaret, Alethia, and Ben — for their continual ability to brighten my days.

In addition to the support I've received at both of my academic institutions, my greatest supporters over the past 27 years of my life have been in my family. My biggest thanks of all goes to my mom, Susan Tinney. Throughout my life, you have been an unending source of love, strength, and wisdom. Your work ethic is unmatched, yet you never fail to put your family above all. You are selflessness personified. Everything I am is because of you; every success of mine belongs to you. To my big sister Chelsea, thank you for always watching over me (even if I didn't always want you to); I am so grateful that you are not only my sister, but my friend. To my Dad, Scott, and to my step-family, Liz and Parisa, thank you for the many wonderful memories, the constant support of and interest in my education, and for always being just a phone call away. I also want to thank Bubu, my grandmother, for being a guiding light for our whole family; phone calls with you are always the highlight of my week. To all of my aunts,

uncles, and cousins, I miss you all dearly as our lives pull us all in different directions, but I know that your love is ever-present and I am so thankful for each of you. I also want to thank Joan Backhaus for welcoming me into her family; I am incredibly grateful for all of the love, joy, humor, and delicious cookies that you bring into my life. To the many friends who have supported me over the years, especially Cherish, Anna, and Olivia, thank you for always being there. Lastly, I want to acknowledge some of my loved ones that have passed along the way: Gigi, Emily Rapson, Uncle John, Uncle Larry, Uncle Jack, Grandpa Bruce, and Grandma June. Thank you for watching over me, and know that you will never be forgotten.

Finally, I want to acknowledge the family that I have in Owen Sanchez and our two wonderful kitties, Gizmo and Leia. Owen, there are no words to express how thankful I am to have you as my life partner. For more than 8 years now, you have been my shoulder to cry on. You never fail to make me smile and laugh, even when I don't want to. You have given me unconditional support as I pursue my dreams and have let me drag you around the country. You remind me that there is more to life than research, and you encourage me to be the best person I can be. You've opened my mind and my heart to things I never knew I would appreciate so dearly — *"This world is cruel, but it is also very beautiful"*. And you are an amazing cat dad to our perfect kitties, which brings me to my final acknowledgements: Gizmo and Leia. Gizmo has blessed me with his presence in my life for more than 17 years now. I grew up with him — from Murphy Elementary School in Haslett to finishing my PhD at the University of Oklahoma in Norman. He has been my emotional support through it all, and he is perfection (purr-fection?) personified. My world really does revolve around him, and I wouldn't have it any other way; I don't think anyone will ever truly understand the bond that we share. Leia has been with us for almost four years now. She is incredibly funny, hungry, sweet, and resilient. What she may lack in common sense, she makes up for with her keen emotional intelligence. She has been such a source of comfort through graduate school — she has an uncanny ability to tell when I am extra stressed and will immediately come to cuddle with me. She also happens to be the best biscuit-maker around. Owen, Gizmo, and Leia — thank you. I love you all so incredibly much.

The work in this dissertation would not be possible without my many collaborators and coauthors. In addition to my advisor (Cameron), I want to extend a thank you Lexy Elizalde, Dale Hurst, Anne Thompson, Ryan Stauffer, Holger Vömel, and Henry

Selkirk for their contributions to Chapter 3 of this dissertation, and to Kristopher Bedka and Benjamin Scarino for their contributions to Chapter 4. This work would not possible without funding by the National Aeronautics and Space Administration (NASA) under Award 80NSSC18K0746 and 80NSSC19K0347, by the National Science Foundation (NSF) under Grant AGS-1560419, and by the University of Oklahoma through the Nancy L. Mergler Dissertation Completion Fellowship.

Table of Contents

Acknowledgments **iv**

List Of Tables **x**

List Of Figures **xi**

Abstract **xvii**

1 Introduction **1**
1.1 The Upper Troposphere and Lower Stratosphere 1
1.1.1 The Tropopause 1
1.1.2 Composition 2
1.1.3 Stratosphere-Troposphere Exchange 3
1.2 Tropopause-Overshooting Convection 4
1.3 A Changing Climate 5
1.4 Study Objectives 7
1.4.1 Study 1: Water Vapor Extremes in the Lower Stratosphere . . . 7
1.4.2 Study 2: Stability-based Tropopause Definition 7
1.4.3 Study 3: Climate Impacts on Overshooting Convection 8

2 Climatology, Sources, and Transport Characteristics of Observed Water Vapor Extrema in the Lower Stratosphere **9**
2.1 Background and Motivation 9
2.2 Data and Methods 11
2.2.1 Reanalysis 11
2.2.2 Global H_2O Observations 11
2.2.3 Stratospheric H_2O Extrema Identification 12
2.2.4 Trajectory Analysis 14
2.2.5 Observations of Convection 15
2.3 Results 15
2.3.1 Extrema Frequency 17
2.3.2 Transport Characteristics 21
2.3.3 Transport in Additional Regions 29
2.3.4 Annual Cycles in Monsoon-Related Regions 30
2.4 Discussion 38

3 A Modern Approach to Stability-Based Definition of the Tropopause 41
3.1 Background and Motivation . . . 41
3.2 Data and Methods . . . 46
3.2.1 Balloon Observations . . . 46
3.2.2 Reanalysis Output . . . 51
3.3 Results . . . 52
3.3.1 Composition-Stability Relationships . . . 52
3.3.2 The Potential Temperature Gradient Tropopause Algorithm . . . 59
3.3.3 Evaluation of the Tropopause Algorithm . . . 61
3.3.3.1 Application to Observations . . . 61
3.3.3.2 Observations of Multiple Tropopauses . . . 71
3.3.3.3 Application to Reanalysis Output . . . 76

4 The Response of Tropopause-Overshooting Convection over North America to Climate Change 82
4.1 Background and Motivation . . . 82
4.2 Data and Methods . . . 84
4.2.1 Model Output and Overshoot Identification . . . 84
4.2.2 Observations and Overshoot Identifications . . . 86
4.3 Results . . . 87
4.3.1 Model Validation . . . 87
4.3.2 Overshoot Frequency . . . 96
4.3.3 Tropopause and Overshoot Characteristics . . . 99
4.4 Discussion . . . 108

5 Summary and Conclusions 111
5.1 Summary of Findings . . . 111
5.1.1 Lowermost Stratosphere Water Vapor Extrema . . . 111
5.1.2 The Potential Temperature Gradient Tropopause . . . 113
5.1.3 Overshooting Convection in a Warming Climate . . . 115
5.2 Looking Forward . . . 116

Reference List 119

List Of Tables

3.1 The total number of balloon observations at least 18 km in depth by type (ECC or O_3-only, FPH/CFH or H_2O-only, and both) and location. 48
3.2 The frequency of double tropopause identifications in the observed profiles. For each site, the double tropopause frequency based on the LRT definition, PTGT definition, and both definitions is given. 72

List Of Figures

2.1 Binned frequency of H_2O extrema ($\geq$ 8 ppmv) as observed by MLS for (a) layers classified as stratospheric, (b) overworld layers only, and (c) the 100 hPa layer only. Eight local maxima are classified into regions (gold) for further analysis. 16

2.2 Binned frequencies of MLS H_2O extrema ($\geq$ 8 ppmv) separated seasonally into December, January, and February (DJF; top row), March, April, and May (MAM; second row), June, July, and August (JJA; third row), and September, October, and November (SON; bottom row) for (left) lower stratospheric layers and (right) stratospheric overworld layers only. 19

2.3 Isentropic backwards trajectory analysis for H_2O extrema in the CEA region (blue box) in JJA. The normalized density of trajectories at initialization and at 2, 4, 6, 8, and 10 days prior is shown by the color-fill, with the maximum density value given in the initialization panel. The seasonal frequency of tropopause-overshooting convection as detected by GPM is given by the golden contours at intervals of $5 * 10^{-5}$ overshoots per observation (lighter gold) and $10 * 10^{-5}$ overshoots per observation (darker gold). The seasonal average tropopause break (i.e. the location of the sharp discontinuity between tropical and extratropical tropopause heights) for each hemisphere is indicated by the solid black line. 22

2.4 As in Fig. 2.3, but for the NP region in JJA. 23

2.5 As in Fig. 2.3, but for the SC region in JJA. 26

2.6 The binned percentage of H_2O extrema trajectories classified as large-scale TST at their initialized location for (a) DJF, (b) MAM, (c) JJA, and (d) SON. To restrict the analysis to bins with sufficient sampling of extrema, percentages are only shown for bins with $\geq$ 20 observations for the corresponding season. 28

2.7 As in Fig. 2.3, but for the NA region in JJA. 31

2.8 As in Fig. 2.3, but for the SA region in SON. 32

2.9 As in Fig. 2.3, but for the GC region in JJA. 33

2.10 As in Fig. 2.3, but for the SP region in DJF. 34

2.11 As in Fig. 2.3, but for the SI region in DJF. 35

2.12 Two average annual cycles of (a) the number of H_2O extrema per grid point, (b) the average regional number H_2O extrema, and (c) the percentage of extrema with a large-scale transport history are given for the Asian Monsoon Anticyclone (AMA; 20°N – 40°N, 30°E – 130°E; purple), the North American Monsoon Anticyclone (NAMA; 20°N – 45°N, 230°E – 290°E; blue) and the South American Monsoon Anticyclone (SAMA; 20°S – 40°S, 260°E – 320°E; red). For (a) and (b), the number of observations for the total lower stratosphere is given by the solid line and the number of observations in the stratospheric overworld only is given by the dotted line. The region boundaries for each monsoon described above are given in (d). 37

3.1 Sites of the balloon observations used in this study. Yellow stars indicate sites with ozonesonde-only observations and purple stars indicate sites that also have water vapor data. 47

3.2 Stacked bar charts indicating the number of balloon profiles reaching at least 18 km above the surface, as a function of year for the 6 balloon sounding sites used. Yellow bars indicate the total number of ozonesonde-only observations, blue the total number of FPH/CFH-only observations, and purple the total number of balloon observations with both instruments. Note that the ordinate varies by observation site. . . 49

3.3 As in Fig. 3.2, but by season. Note that the disproportionate number of ECC soundings at South Pole Station during SON is due to an increased frequency of soundings each year during the formation and evolution of the polar ozone holes. 50

3.4 Example ozonesonde profiles of (from left to right) temperature (T; blue) and potential temperature (θ; red), vertical gradients of T ($\Delta T/\Delta z$) and θ ($\Delta\theta/\Delta z$), the Brunt-Väisälä frequency N, and ozone volume mixing ratio (purple). For the T, θ, and stability profiles, the raw data are shown by the black and gray profiles in the background, while colored lines show 2-σ Gaussian smoothing of the raw T and θ data. In the second panel, vertical blue and red dashed lines are given at constant values of $\Delta T/\Delta z = -2$ K km^{-1} and $\Delta\theta/\Delta z = 10$ K km^{-1}, respectively. The profiles are sourced from (top) South Pole Station, Antarctica on 11 October 2006 at 20:22 UTC, (middle) Boulder, Colorado on 28 June 2019 at 16:24 UTC, and (bottom) San José, Costa Rica on 10 March 2010 at 13:51 UTC. 54

3.5 Two-dimensional frequency distributions of ozone vs. (left) potential temperature gradient $\Delta\theta/\Delta z$, (middle) Brunt-Väisälä frequency N, and (right) temperature gradient $\Delta T/\Delta z$ for all measurements from each observation site. Ozone is placed into logarithmic bins of size 0.1, while $\Delta\theta/\Delta z$, $\Delta T/\Delta z$, and N are placed into bins of size 2 K km^{-1}, 1 K km^{-1}, and 0.002 s^{-1}, respectively. Contours represent the frequency of observations relative to the maximum value within any 2-D bin in each panel, with shading at 1, 3, 6, 10, 30, and 60%. Gray horizontal lines are given in each panel at constant values of $\Delta\theta/\Delta z$ = 10 K km^{-1}, N = 0.017 s^{-1}, and $\Delta T/\Delta z = -2$ K km^{-1}, for reference. 57
3.6 Values of $\Delta\theta/\Delta z$ as a function of (a) $\Delta T/\Delta z$ and pressure, and (b) N and θ. Black vertical lines are given at constant values of (a) $\Delta T/\Delta z = -2$ K and (b) N = 0.017 s^{-1}. 59
3.7 For the same profiles in Fig. 3.4: (left) profiles of temperature (T; blue) and potential temperature (θ; red) and (right) profiles of ozone volume mixing ratio. Altitudes of objectively diagnosed lapse-rate tropopauses (LRT; gray) and potential temperature gradient tropopauses (PTGT; green) are superimposed. 62
3.8 Scatterplots comparing PTGT and LRT altitudes for all balloon observations used in this study, separated by observation site. The solid black lines are 1-to-1 lines and the dashed black lines show the boundaries of ± 1 km altitude differences. Red contours indicate the density of observations in 1-km × 1-km bins as the fraction of the total number of profiles, doubling in magnitude from 0.5 to 8 % (i.e., 0.5, 1, 2, 4, and 8 %). 64
3.9 For all profiles with ozone from each observation site: tropopause-relative profiles of (left) ozone, (middle) potential temperature, and (right) temperature. Thin lines bounding the color-fill in each panel span the 10th- to 90th-percentile observations for each variable, while thick lines superimposed on the color-fill represent the median value. Blue profiles are relative to the LRT, while red profiles are relative to the PTGT. 67
3.10 As in Fig. 3.9, but only for instances where the PTGT is located more than 1 km below the LRT. 68

3.11 Locations of identified PTGTs and LRTs in tracer–tracer space for co-located observations of ozone and water vapor from the Boulder, Hilo, San José, and Lauder stations for (a) high-tropopause (tropical) environments, (b) low-tropopause (extratropical) environments, and (c) environments where a tropical and extratropical tropopause are identified by the LRT and PTGT definitions, respectively. Gray shading indicates the number of 250-m layer observations placed into each water vapor-ozone (0.1 log(ppmv) x 75 ppbv sized) bin, and red and blue contours represent the frequency of PTGT and LRT definitions in tracer–tracer space (in %), respectively. The number of profiles contributing to each panel are: (a) 358, (b) 332, and (c) 59. 70
3.12 As in Fig. 3.7, but for select profiles with a double tropopause identification: (a,b) LRT-only, (c,d) PTGT-only, and (e,f) LRT and PTGT. Secondary tropopauses are given by the dashed horizontal lines. 74
3.13 Frequency distributions of tropopause altitude differences for profiles with a double tropopause (DT), using data from the six balloon sites. From left to right: profiles with a DT identified by only the LRT definition, only the PTGT definition, and both the LRT and PTGT definitions. For cases where only one tropopause definition identifies a DT, black solid lines indicate differences between the primary tropopause altitudes of the two definitions and dashed gray lines indicate differences between the secondary tropopause and the primary tropopause identified by the other definition. For cases where both the LRT and PTGT identify a DT, solid black lines indicate differences between primary tropopauses and dashed gray lines indicate differences between secondary tropopauses. The number of profiles used in each panel is noted. 76
3.14 Maps of primary tropopause altitude diagnosed by the PTGT and LRT definitions for four select MERRA-2 reanalysis times: (top to bottom) 15 January 2020, 15 April 2020, 15 July 2020, and 15 October 2020. Thick yellow lines in each panel correspond to the locations of the vertical cross-sections in Fig. 3.16. 78
3.15 As in Fig. 3.14, but for secondary tropopause altitude when present. . . 79
3.16 Pole-to-pole vertical cross-sections of MERRA-2 output for the four times in Fig. 3.14. Horizontal wind speeds are shown by the red color-filled contours (every 10 m s^{-1}, starting at 20 m s^{-1}), potential temperature (in K) by the black contours, potential vorticity above 4 km by the purple contours (every 2 PVU from ±2–6 PVU), PTGT altitudes by the green circles, PTGT secondary tropopause altitudes by the green diamonds, LRT altitudes by the gray circles, and LRT secondary tropopause altitudes by the gray diamonds. 81

4.1 The average number of overshoots per year placed into 0.4° latitude-longitude bins for (a) GridRad, (b) GOES, (c) the WRF CTRL experiment, and (d) the WRF PGW experiment. The domain bounds of each individual dataset are indicated by the blue dashed lines. 89
4.2 The average annual cycle of (blue) the CTRL experiment, (green) GridRad, and (red) GOES across their respective domains shown in Fig. 4.1 displayed as both the total counts of overshoots (left) and as normalized frequencies (right). 91
4.3 As in Fig. 4.2, but for the diurnal cycle. 92
4.4 The change in the number of overshoots per year from the CTRL experiment to the PGW experiment in 0.4° latitude-longitude bins. Only bins in which the PGW experiment mean exceeds 2 standard deviations (left) and three standard deviations (right) of the CTRL experiment are shown. Regions of large increases are identified by the black polygons for further regional analysis: the Sierra Madre (SM), the Northern Plains (NP), the Southern Plains (SP), the Gulf Coast (GC), the East Coast (EC), and the domain that is common to and well sampled by all three datasets (Common Domain, CD). The model domain is indicated by the blue dashed lines. 93
4.5 The average annual cycle of (blue) the CTRL experiment, (green) GridRad, and (red) GOES for the (a) Common Domain, (b) Sierra Madre, (c) Northern Plains, (d) Southern Plains, (e) Gulf Coast, and (f) East Coast regions as identified in Fig. 4.4. 94
4.6 As in Fig. 4.5, but for the diurnal cycle. 95
4.7 The average annual cycle of (blue) the CTRL experiment and (pink) the PGW experiment displayed as both the total counts of overshoots (left) and as normalized frequencies (right). 97
4.8 As in Fig. 4.7, but for the diurnal cycle. 98
4.9 The average annual cycle of (blue) the CTRL experiment and (pink) the PGW experiment for the (a) Common Domain, (b) Sierra Madre, (c) Northern Plains, (d) Southern Plains, (e) Gulf Coast, and (f) East Coast regions as identified in Fig. 4.4. 100
4.10 As in Fig. 4.9, but for the diurnal cycle. 101
4.11 The change in average PTGT altitude from the CTRL experiment to the PGW experiment (color shading) with average CTRL PTGT heights overlaid as black contours for (a) the full year, (b) December, January, and Febuary (DJF), (c) March, April, May (MAM), (d) June, July, August (JJA), and (e) September, October, November (SON). 103
4.12 Histograms of overshooting depth for the CTRL experiment (blue) and the PGW experiment (pink), with 0.5 km bin sizes. Note that the ordinate is logarithmic. 104

4.13 Histograms of overshooting depth for the CTRL experiment (blue) and the PGW experiment (pink), with 0.5 km bin sizes for the (a) Common Domain, (b) Sierra Madre, (c) Northern Plains, (d) Southern Plains, (e) Gulf Coast, and (f) East Coast regions as identified in Fig. 4.4. Note that the ordinates are logarithmic. 105
4.14 Frequency histograms of PTGT altitude during overshooting events for the CTRL experiment (blue) and the PGW experiment (pink), with 1 km bin sizes. 107

Abstract

The troposphere and the stratosphere are two separate layers of the atmosphere whose dynamics, composition, and chemistry are fundamentally different. This leads to the upper troposphere and lower stratosphere (UTLS) being a complex region of the atmosphere that is critically important to both weather and climate. The upper troposphere is separated from the lower stratosphere by an identified 'tropopause', and any transfer of air across this interface is therefore considered to be stratosphere-troposphere exchange (STE). The difference in composition between the troposphere and the stratosphere makes processes that facilitate STE essential to the climate system. Specifically, the transport of water vapor from the relatively moist troposphere to the much drier lower stratosphere, where water vapor functions as a powerful greenhouse gas, can contribute substantially to the warming climate at the surface. The sources of stratospheric water vapor are still a topic of debate in the scientific community, where the specific contributions of larger-scale processes like the global atmospheric circulation and smaller-scale processes like tropopause-overshooting convection remain unclear, though recent evidence has demonstrated the latter to be more important than was previously thought. This dissertation seeks to clarify the role that tropopause-overshooting convection has in modulating the lower stratospheric water vapor budget in both the present and in the future.

The first component of this dissertation is the creation of a climatology of extreme water vapor concentrations within the lowermost stratosphere, with a complementary analysis exploring the sources and transport pathways of these extreme concentrations. Stratospheric water vapor is a substantial component of the global radiation budget, and therefore important to variability of the climate system. Efforts to understand the distribution, transport, and sources of stratospheric water vapor have increased in recent years, with many studies utilizing long-term satellite observations. Previous work to examine stratospheric water vapor extrema has typically focused on the stratospheric overworld (pressures $\leq$ 100 hPa) to ensure the observations used are truly stratospheric. However, this leads to the broad exclusion of the lowermost stratosphere, which can extend over depths more than 5 km below the 100 hPa level in

the midlatitudes and polar regions and has been shown to be the largest contributing layer to the stratospheric water vapor feedback. Moreover, focusing on the overworld only can lead to a large underestimation of stratospheric water vapor extrema occurrence. Therefore, this dissertation expands on previous work by examining 16 years of Microwave Limb Sounder (MLS) observations of water vapor extrema ($\geq$ 8 ppmv) in both the stratospheric overworld and the lowermost stratosphere to create a new lower stratosphere climatology. The resulting frequency of H_2O extrema increases by more than 300% globally compared to extrema frequencies within stratospheric overworld observations only, though the percentage increase varies substantially by region and season. Additional context is provided to this climatology through a backward isentropic trajectory analysis to identify potential sources of the extrema. It is shown that, in general, tropopause-overshooting convection presents as a likely source of H_2O extrema in much of the world, while meridional isentropic transport of air from the tropical upper troposphere to the extratropical lower stratosphere is also possible.

The second dissertation component takes a step back to examine challenges related to definition of the tropopause. Any study which examines cross-tropopause transport, like the first component of this dissertation, is reliant on an accurately identified tropopause in order to correctly assess STE. Thus, proper definition of the tropopause has far reaching implications for our understanding of Earth's radiation budget and climate. Definition of the tropopause has remained a focus of atmospheric science since its discovery near the beginning of the 20th century. Few universal definitions (those that can be reliably applied globally and to both common observations and numerical model output) exist and many definitions with unique limitations have been developed over the years. The most commonly used universal definition of the tropopause is the temperature lapse-rate definition established by the World Meteorological Organization (WMO) in 1957 (the LRT). Despite its widespread use, there are recurrent situations where the LRT definition fails to reliably identify the tropopause. Motivated by increased availability of coincident observations of stability and composition, this study seeks to re-examine the relationship between stability and composition change in the tropopause transition layer and identify areas for improvement in stability-based definition of the tropopause. In particular, long-term (40+ years) balloon observations of temperature, ozone, and water vapor from six locations across the globe are used

to identify co-variability between several metrics of atmospheric stability and composition. The results demonstrate that the vertical gradient of potential temperature is a superior stability metric to identify the greatest composition change in the tropopause transition layer, which is used to propose a new universally applicable potential temperature gradient tropopause (PTGT) definition. Application of the new definition to both observations and reanalysis output reveals that the PTGT largely agrees with the LRT, but more reliably identifies tropopause-level composition change when the two definitions differ greatly.

The final component of this dissertation examines the response of tropopause-overshooting convection to a warming climate. Recent field campaigns, observational studies, and modeling work, in addition to the first component of this dissertation, have demonstrated that extratropical tropopause-overshooting convection has a substantial, and previously underestimated impact on UTLS composition, especially stratospheric water vapor. This necessitates improved understanding of how tropopause-overshooting convection may change in a warming climate. A growing body of research indicates that environments conducive to severe thunderstorms will occur more often and be increasingly unstable in the future, but no study has examined how this may be related to increased overshooting. To rectify this, this study leverages an existing pseudo-global warming (PGW) experiment to evaluate potential future changes in tropopause-overshooting convection over North America. The PGW technique applies monthly, three-dimensional projected climate changes in state variables (temperature, humidity, wind, etc.) from global climate models to a weather and research forecasting (WRF) convection-allowing model simulation with a 4-km grid. Specifically, I examine two 10-year simulations consisting of (1) a retrospective period (2003 – 2012) forced by ERA-interim initial and boundary conditions (the control simulation), and (2) the same retrospective period with CMIP5 ensemble-mean high-end emission scenario climate changes added to the initial and boundary conditions (the PGW simulation). Tropopause-overshooting convection is identified as model cloud tops exceeding the potential temperature gradient tropopause, with overshooting in the control simulation validated against observed overshoots from both ground-based radar observations in the United States and GOES satellite observations over North America. The model is shown to effectively simulate the observed regional distribution, annual cycle, and diurnal cycle of tropopause-overshooting convection. The projected response of

tropopause-overshooting convection in the PGW simulation is found to be a more than 250% increase across the model domain, and the projected seasonal period of frequent tropopause-overshooting convection was shown to extend into late-summer. Additionally, tropopause-overshooting convection with extreme tropopause-relative heights (> 4 km) are more frequent in a warmed climate scenario.

In summary, this dissertation (1) examines extreme water vapor concentrations in the lowermost stratosphere and how they relate to tropopause-overshooting convection, (2) introduces an improved stability-based tropopause definition to improve future studies of stratosphere-troposphere exchange, and (3) investigates for the first time how tropopause-overshooting convection will respond to climate change.

Chapter 1

Introduction

1.1 The Upper Troposphere and Lower Stratosphere

1.1.1 The Tropopause

The complex transition layer that separates the upper troposphere and the lower stratosphere is known as the tropopause. Since its discovery in the early 20$^{\text{th}}$ century (see Hoinka (1997) for a review), various approaches to define the tropopause transition layer have been proposed. Most proposed definitions, for convenience or simplicity, define the tropopause as a boundary, despite increasing recognition that it is best characterized as a layer of depth ranging from tens of meters to several kilometers (e.g., Hoinka 1997; Hegglin et al. 2009; Homeyer et al. 2010; Tilmes et al. 2010; Pan et al. 2014). Some notable findings of global tropopause characteristics since its discovery include: i) tropopause altitudes are uniformly high in the tropics and uniformly low in the extratropics, with a discontinuity in altitude occurring near the subtropical jet that is known as the "tropopause break" (Palmén 1948; Danielsen 1959; Randel et al. 2007a), ii) the tropopause can become significantly deformed and difficult to identify in highly dynamic situations (and, often, stratosphere–troposphere exchange events) such as within tropopause folds driven by ageostrophic circulations near upper tropospheric jets and in regions impacted by Rossby wave breaking that contain widespread vertical lamination of tropical upper troposphere air and extatropical lower

stratosphere air (Reed 1955; Danielsen 1968; Shapiro 1980; Browell et al. 1987; Newman and Schoeberl 1995; Vaughan and Timmis 1998; Olsen et al. 2008; Pan et al. 2009), iii) the extratropical tropopause is characterized by a strong temperature inversion ∼2–3 km in depth, referred to as the "tropopause inversion layer" or TIL, which is driven by radiative processes and dynamic processes such as downwelling and column stretching/shrinking (Birner 2006; Randel et al. 2007b; Son and Polvani 2007; Peevey et al. 2014), and iv) long-term changes in tropopause altitude can be used as an indicator of global climate change (Seidel et al. 2001; Shepherd 2002; Santer et al. 2003; Seidel and Randel 2006; Xian and Homeyer 2019; Meng et al. 2021; Thompson et al. 2021). While dozens of tropopause definitions have been proposed over the years, they can be separated into three main categories: stability-based, dynamics-based, and composition-based definitions.

1.1.2 Composition

The troposphere and stratosphere are fundamentally different in their composition of atmospheric trace gases. For example, while abundant in the troposphere, water vapor in the stratosphere is uniformly low and can therefore be considered a 'tropospheric tracer'. Similarly, carbon monoxide is a primarily human-generated pollutant that is rare in the stratosphere and can therefore be considered both a tropospheric and a boundary-layer tracer. Alternatively, the stratosphere is rich in ozone — making ozone a common tracer of stratospheric air. Given these sharp composition gradients across the tropopause, stratosphere-troposphere exchange (STE), or transport between these airmasses, can significantly and rapidly alter the composition and therefore radiative forcing of the upper troposphere and lower stratosphere (UTLS).

The LS can be categorized into two separate regions: the extratropical lowermost stratosphere (LMS) and the stratospheric overworld. The stratospheric overworld is

conventionally defined where potential temperature, θ, is at least 380 K, such that isentropes of the stratospheric overworld remain above the tropopause globally (e.g., Hoskins 1991; Holton et al. 1995; Stohl et al. 2003). The remaining portion of the stratosphere is the LMS, which lies above the extratropical tropopause but below the 380 K isentrope (i.e. below the height of the tropical tropopause). Therefore, the total LS can be thought of as the combination of the LMS and the lower part (i.e., $\theta \leq 450$ K, or $\sim$ 2–3 km above the tropical tropopause) of the stratospheric overworld. The concentration of water vapor in the overworld is strongly correlated to and controlled by tropical tropopause temperatures, via the freeze-drying of air across the tropical tropopause as part of the ascending branch of the Brewer–Dobson circulation (e.g., Randel and Park 2019; Mote et al. 1996). Alternatively, water vapor in the LMS is impacted by both the downwelling branch of the Brewer–Dobson circulation and frequent STE, specifically troposphere-to-stratosphere transport (TST; Holton et al. 1995; Stohl et al. 2003), though the contributions of specific processes are still not well understood.

1.1.3 Stratosphere-Troposphere Exchange

At larger scales, enhancements in LMS water vapor concentrations can be linked to isentropic cross-tropopause transport. So-called "tropospheric intrusions" are driven by poleward Rossby wave breaking events and transport tropical upper troposphere air to the extratropical LMS across the tropopause break near the subtropical jet (Pan et al. 2009; Homeyer et al. 2011; Homeyer and Bowman 2013; Ploeger et al. 2013; Langille et al. 2020). Note that while a small population of these events have been shown to substantially moisten the LMS, tropospheric intrusions are frequently related to decreases in LMS water vapor (Schwartz et al. 2015). Large-scale cross-tropopause transport can also be facilitated by isentropic ascent along the warm conveyor belts of

midlatitude cyclones, which has been shown to transport water vapor and boundary-layer pollutants into the LMS (Roiger et al. 2011; Stohl 2001; Wernli and Bourqui 2002). Isentropic transport related to monsoon dynamics — which is intrinsically linked with smaller-scale monsoon convection — has also been shown to substantially contribute to LMS water vapor enhancements (e.g., Randel et al. 2010; Pan et al. 2016; Honomichl and Pan 2020; Pan et al. 2022).

Tropopause-overshooting convection typically results in the most extreme localized stratospheric hydration. While some studies identify a minimal role of convective contributions to stratospheric water vapor ($\sim$10%), these are typically restricted in focus to tropical convection and impacts on the stratospheric overworld (e.g., Dauhut and Hohenegger 2022; Ueyama et al. 2023, and references therein). Studies that focus on convection within extratropical environments, subtropical environments, and monsoon regions often show substantial contributions from convection to the LMS water vapor concentration locally (Hanisco et al. 2007; Dessler and Sherwood 2004; Smith et al. 2017; Jensen et al. 2020; Tinney and Homeyer 2021; Gordon and Homeyer 2022; Phoenix and Homeyer 2021; Homeyer et al. 2014; Hegglin et al. 2004; Mullendore et al. 2005; Schwartz et al. 2013; Werner et al. 2020; O'Neill et al. 2021; Homeyer et al. 2023). Overall, the contributions of any specific process to the stratospheric water vapor budget, especially deep convection, remain a topic of scientific debate.

1.2 Tropopause-Overshooting Convection

Ground-based radar observations and satellite-based precipitation and cloud observations have been examined to establish global and regional climatologies of tropopause-overshooting convection in recent years (e.g., Homeyer and Bowman 2021; Liu et al. 2020; Clapp et al. 2019; Liu and Liu 2016; Solomon et al. 2016; Pan and Munchak

2011; Bedka et al. 2010; Liu and Zipser 2005). In both tropical and midlatitude environments, tropopause-overshooting convection most frequently occurs over land (e.g., Liu et al. 2020). A number of studies have demonstrated that the contiguous United States (CONUS) is one of the most active overshooting regions in the world — in terms of both frequency and in depth — where vast majority of overshooting occurs over the central Great Plains. Cooney et al. (2018) demonstrated that approximately half of overshoots in CONUS reach the stratospheric overworld, and the overshoot potential can be greater in environments with a low-stability layer above the primary tropopause (Homeyer et al. 2014). Additionally, there exists a strong seasonal cycle where the occurrence of tropopause-overshooting convection peaks in the late spring/early summer (e.g., Solomon et al. 2016). Occasionally, overshooting convection injects ice above the broader storm anvil, producing an above anvil cirrus plume made of ice. Plumes occur relatively frequently in strong, tropopause-overshooting convection that produces severe weather (∼75% of the time; Bedka et al. 2018).

1.3 A Changing Climate

The Earth's surface has warmed 1.1°C by 2020 compared to a 1850–1900 baseline — primarily driven by human activities and greenhouse gas emissions (Arias et al. 2021). The initial radiative imbalance caused by greenhouse gas emissions is compounded by climate feedbacks that can act to either accelerate or mitigate the warming. Of particular interest to this dissertation is the stratospheric water vapor feedback, which describes how the stratosphere is expected to warm in response to anthropogenic climate change, which in turn can increase the concentration of stratospheric water vapor, leading to additional warming (Nowack et al. 2023; Konopka et al. 2022; Li and Newman 2020; Banerjee et al. 2019; Dessler et al. 2013). Banerjee et al. (2019) found that

the stratospheric water vapor feedback is the same order of magnitude as the surface albedo feedback and the cloud feedback, demonstrating that improved understanding of this response is necessary in order to validate and refine projections of the changing climate. Recent work has also shown that the LMS contains a majority of the stratospheric water vapor feedback (Konopka et al. 2022; Li and Newman 2020; Banerjee et al. 2019; Dessler et al. 2013). This implies that troposphere-to-stratosphere transport and water vapor enhancements driven by midlatitude tropopause-overshooting convection now and in the future are a potentially important component of this feedback.

Though the response of extratropical tropopause-overshooting convection to climate change has not been explored previously in the literature, a number of studies have examined the relationship between climate change and the occurrence of severe weather. Specifically, research has focused on the response of environmental parameters that are conducive to severe weather — and therefore deep convection — to climate change, like convective available potential energy (CAPE) and deep-layer wind shear (Brooks et al. 2003). Many recent studies have focused on environments in the CONUS where severe weather is frequent, and are nearly unanimous in projecting an increase of CAPE in the future (e.g., Diffenbaugh et al. 2013). While surface warming and tropospheric destabilization are both important factors in increasing CAPE, the overall trend has been found to be largely a result of increasing low-level moisture (Hoogewind et al. 2017; Diffenbaugh et al. 2013; Trapp et al. 2009). In addition to examining environmental parameters, a number of studies have employed the computationally-expensive method of dynamically downscaling climate models to directly simulate convection in a projected future climate and have shown variable changes to the location and seasonal timing of severe weather events (e.g., Hoogewind et al. 2017; Gensini and Mote 2015, 2014). On its own, increasing tropospheric instability would act to increase the likelihood of tropopause-overshooting convection, however, a warming climate has also

been shown to be associated with higher tropopause heights (Meng et al. 2021; Xian and Homeyer 2019; Lorenz and DeWeaver 2007; Santer et al. 2003; Shepherd 2002), which would make overshooting more difficult. These competing changes imply the response of tropopause-overshooting convection to climate change is not easily inferred from existing understanding of related Earth system changes.

1.4 Study Objectives

Motivated by the current state of the research, this dissertation seeks to fill a gap in the literature as it relates to the lowermost stratosphere, convection, and climate change. The dissertation is comprised of three individual studies, each with their own unique research questions.

1.4.1 Study 1: Water Vapor Extremes in the Lower Stratosphere

In Chapter 2, a climatology of water vapor extremes in the lowermost stratosphere is compiled. Specifically, this study seeks to address the following questions:

1. What does the distribution of water vapor extrema in the lowermost stratosphere look like and how does it differ from the stratospheric overworld?

2. What are the large-scale transport pathways to regions of frequent extreme values and what are the likely sources of extreme water vapor concentrations?

1.4.2 Study 2: Stability-based Tropopause Definition

In Chapter 3, the relationship between UTLS composition change and common metrics of atmospheric stability is evaluated. Specifically, this study seeks to address the following questions:

1. Which stability metric best corresponds to the tropopause-level composition change in the UTLS?

2. Is it possible to improve upon the known limitations of existing definitions by designing an alternative, universally applicable stability-based tropopause definition?

1.4.3 Study 3: Climate Impacts on Overshooting Convection

In Chapter 4, the response of tropopause-overshooting convection to a changing climate is evaluated for the first time. Specifically, this study seeks to address the following questions:

1. How does the frequency and distribution of tropopause-overshooting convection change in a warmed climate scenario?

2. How do tropopause characteristics and overshoot characteristics change in response to the prescribed warming signal?

Chapter 2

Climatology, Sources, and Transport Characteristics of Observed Water Vapor Extrema in the Lower Stratosphere

This chapter is based on and reproduced from the following published peer-reviewed journal article:

> Tinney, E. N., and C. R. Homeyer, 2023: Climatology, sources, and transport characteristics of observed water vapor extrema in the lower stratosphere. *Atmospheric Chemistry and Physics*, **23**, 14375–14392, https://doi.org/10.5194/acp-23-14375-2023.

Some sections of Chapter 1 are based upon this article as well.

2.1 Background and Motivation

As noted in Chapter 1, the composition of trace gases in the troposphere and stratosphere are fundamentally different, which makes composition in the UTLS especially sensitive to STE. In the lower stratosphere (LS), the per molecule radiative forcing of water vapor (H_2O) is maximized, where even small increases (on the order of $<$ 1 ppmv) can lead to substantial surface warming (Solomon et al. 2010; Dessler et al. 2013; Wang et al. 2017). An understanding of the sources and controls of stratospheric

water vapor is therefore essential for improving our understanding of the climate system. This is especially valuable due to the implications of stratospheric H_2O acting as a positive climate feedback, where stratospheric H_2O concentrations increase in response to anthropogenic global warming (Dessler et al. 2013; Banerjee et al. 2019; Konopka et al. 2022; Nowack et al. 2023).

An important instrument that has been frequently employed in studying the global LS H_2O is NASA's Microwave Limb Sounder (MLS). For example, Schwartz et al. (2013) and Werner et al. (2020) use MLS observations to assess the global distribution of high H_2O concentrations at a pressure level of 100 hPa, which is commonly found at a similar level to the 380 K isentrope. Both studies show that high H_2O concentrations ($\geq$8 ppmv) are most frequent in monsoon-related active convection regions and therefore contribute to the growing body of evidence suggesting that convection is a substantial contributor to LS H_2O, especially at a regional level. However, such studies do not evaluate the frequency of H_2O enhancements in the LMS, which can encompass a layer 5 km or deeper below the 100 hPa and 380 K levels (Holton et al. 1995). Higher MLS pressure levels have not been considered in previous studies due to large latitudinal and seasonal variations in tropopause heights complicating the diagnosis of LMS layers. Unfortunately, this choice is likely to lead to substantial underestimations of both the frequency and the magnitude of enhanced LMS H_2O concentrations. The potential for underestimation of convection-driven extrema specifically is expected to be impacted the most since convection-driven enhancements are typically confined to only a few kilometers above the tropopause (e.g., Tinney and Homeyer 2021).

Therefore, this study expands upon previous work by examining 16 years (2005–2020) of MLS H_2O observations to create a climatology of H_2O extrema in both the lowermost and the overworld stratosphere. To achieve this, reanalysis data is used to diagnose whether individual layers in an MLS profile are stratospheric, allowing

for accounting of observed LMS H_2O extrema for the first time. Additional context is provided for these observations through an isentropic back-trajectory analysis of common transport pathways and discussion of the potential roles of large-scale vs. convective sources.

2.2 Data and Methods

2.2.1 Reanalysis

Three-hourly assimilations of the global atmosphere are employed from the NASA Modern-Era Retrospective Analysis for Research and Applications, version 2 (MERRA-2; Gelaro et al. 2017). Temperature, pressure, potential vorticity (PV), and wind fields are used in this study. MERRA-2 lapse-rate tropopause (LRT) heights and pressures are calculated according to the World Meteorological Organization (WMO) definition (World Meteorological Organization 1957). MERRA-2 is available from 1979–present on an approximately 0.5° x 0.625° longitude-latitude grid with 72 vertical model levels, which corresponds to ∼1.1 km vertical resolution in the UTLS.

2.2.2 Global H_2O Observations

Measurements of H_2O in the UTLS are sourced from the Earth Observing System (EOS) Microwave Limb Sounder (MLS) v5.0x dataset. The MLS is aboard the Aura spacecraft as part of the NASA A-Train constellation of sun-synchronous satellites, and has Equator crossing times of 0130 and 1330 LT. The instrument performs a continuous vertical scan of the atmosphere (surface–90 km) in the forward direction of orbital motion, completing ∼3600 profiles per day with a 1.5° along-track separation between each scan (Livesey et al. 2020). Concentrations of 16 different trace gases

have been collected globally by MLS since August 2004. The MLS retrieval range of H_2O is 316–0.001 hPa, with measurements at 12 levels per decade of pressure in the UTLS. The precision, accuracy, horizontal resolution and vertical resolution of the H_2O measurement vary with height, ranging from 4–65%, 4–25%, 168–400 km, and 1.3–3.5 km, respectively, for pressures 316–1.0 hPa before degrading at lower pressures. Only MLS layers with pressures of 147 hPa and less are analyzed here, where the precision and accuracy of the measurement are more suitable for this study. The data are quality-controlled following the recommendations of Livesey et al. (2020). The MLS v5.0x has a number of improvements from previous data versions, including partial amelioration of a calibration-related drift in the H_2O measurement.

2.2.3 Stratospheric H_2O Extrema Identification

MLS observations from 2005–2020 are utilized in conjunction with MERRA-2 data to assess the frequency of H_2O extrema in the stratosphere. MERRA-2 LRT pressure, PV, and potential temperature (θ) are linearly interpolated in space and time to each MLS profile location, and logarithmically interpolated vertically to the individual layers of each MLS profile. These atmospheric parameters are then employed to diagnose whether any individual MLS layer is located in the stratosphere. The most important aspect of this method is to balance the objective of retaining as many LMS observations as possible for analysis with the necessary condition that the identified stratospheric layers are free of tropospheric contamination (which would result in artificially high frequencies of stratospheric H_2O extrema, especially in the LMS). This is particularly important due to the relative thickness of MLS layers and potential uncertainties in tropopause identification.

Employing a singular criterion, like a requirement that MLS layers be above the LRT, proved to be insufficient as LRT errors along the tropopause break led to large

swaths of nonphysical extrema occurrences. Similarly, a single PV-based requirement showed clear tropospheric contamination in regions with frequent stratospheric intrusions (or tropopause folding events). Ultimately, a combination of multiple requirements is required to ensure that the limitations of any single stratospheric parameter do not lead to tropospheric contamination within the analysis. To determine appropriate thresholds for each requirement, the analysis was performed and subjectively evaluated with dozens of different threshold combinations until a suitable final set of criteria were selected. These criteria were chosen as they allowed for as many layers in the analysis as possible while still limiting tropospheric contamination (which is characterized by widespread, uniformly high frequencies of H_2O extrema).

Therefore, based on the rigorous testing and evaluation described above, it is required that layers meet a set of three criteria to be classified as wholly stratospheric: (1) $PV \geq 6$ PVU, (2) $log(P_{MLS}) \leq log(P_{LRT}) - 0.075$ (i.e. the layer must be at least ~ 1 km above the LRT), and (3) $\theta \geq 340$ K. While these criteria are applicable in the middle and high latitudes, they are inappropriate for application to tropical profiles due to PV converging to zero in this region. Therefore, MLS layers are also considered to be stratospheric if $\theta \geq 380$ K. As an upper limit for layers to be included in the analysis, it is additionally required that layers have $\theta \leq 450$ K to restrict the analysis to lower stratosphere layers only. This set of stringent criteria allows us to analyze observations characteristic of the extratropical LMS and ensure that tropospheric contamination is minimized. In a few rare circumstances, these criteria can be met within the deep tropics; an example of this is discussed in detail in Sect. 2.3.2.

For analysis, the wettest identified stratospheric MLS layers from each profile are collected in 5° latitude-longitude bins (i.e., only one layer from each profile is used). The frequency of H_2O extrema (exceeding a given threshold) in each bin is then calculated.

To quantify how inclusion of the LMS impacts the distribution and frequency of extrema identification, the same binning process is completed for stratospheric overworld ($\theta \geq 380$ K) observations only. Due to seasonal variation in the frequency, location, and magnitude of stratospheric H_2O extrema, analysis is conducted separately for DJF (December, January, February), MAM (March, April, May), JJA (June, July, August), and SON (September, October, November) when necessary.

2.2.4 Trajectory Analysis

To provide context for the LMS H_2O extrema climatology, large-scale transport characteristics are explored via isentropic trajectory analyses. Trajectories are initialized at the latitude, longitude, and θ of stratospheric H_2O extrema that occur within eight identified high-frequency regions shown in Fig. 2.1. Using the TRAJ3D trajectory model (Bowman 1993; Bowman and Carrie 2002), particles are advected backward in time using MERRA-2 winds for up to 10 days, with positions saved every 6 hours along the trajectory path. Two-dimensional (latitude-longitude) frequency distributions of trajectory particle locations at multiple time intervals are used to identify common pathways to regions of frequent extrema. Given the MERRA-2 spatiotemporal resolution and wind field uncertainties, horizontal displacement errors of individual trajectories are expected to be $\sim$60 km per day (Bowman et al. 2013; Stohl et al. 1995), but these errors are largely irrelevant for examining the bulk transport behavior sought here. Evaluating the recent history of identified H_2O extrema air masses helps to provide context for their potential (or likely) sources.

2.2.5 Observations of Convection

Observations of tropopause-overshooting convection are sourced from NASA's Global Precipitation Measurement (GPM) mission. The GPM core satellite was launched in 2014 and is able to measure precipitation characteristics in three dimensions, allowing for the detection of precipitation features from the tropics to the middle and high latitudes (Hou et al. 2014; Skofronick-Jackson et al. 2017; Nesbitt et al. 2000; Liu et al. 2008). These precipitation features can be used in combination with tropopause altitudes to identify overshooting convection. An extended record (2015–2020) of GPM overshoots that was originally produced for and analyzed in Liu et al. (2020) is used, which has been updated to use the newer ECMWF Reanalysis version 5 (ERA5) LRT as a reference (Hersbach et al. 2020). Any precipitation feature (radar echo >20 dBZ) found at an altitude above the ERA5 LRT altitude is classified as an overshoot. The resulting seasonal geographic distributions of overshoot frequency are used to provide context for the transport analysis in this study.

2.3 Results

The analysis presented here was completed for three different thresholds of H_2O extrema (8, 10, and 12 ppmv). As expected, the frequency of extrema identification decreases as the threshold increases. In general, the choice of threshold does not have a substantial impact on the global and seasonal distributions of extrema. For simplicity, I therefore present here the results for H_2O extrema exceeding 8 ppmv only, as this is the most commonly used extrema threshold in prior work and provides the largest sample of extrema for analysis. Relevant discussion of sensitivities to the extrema threshold can be found in Sect. 2.4.

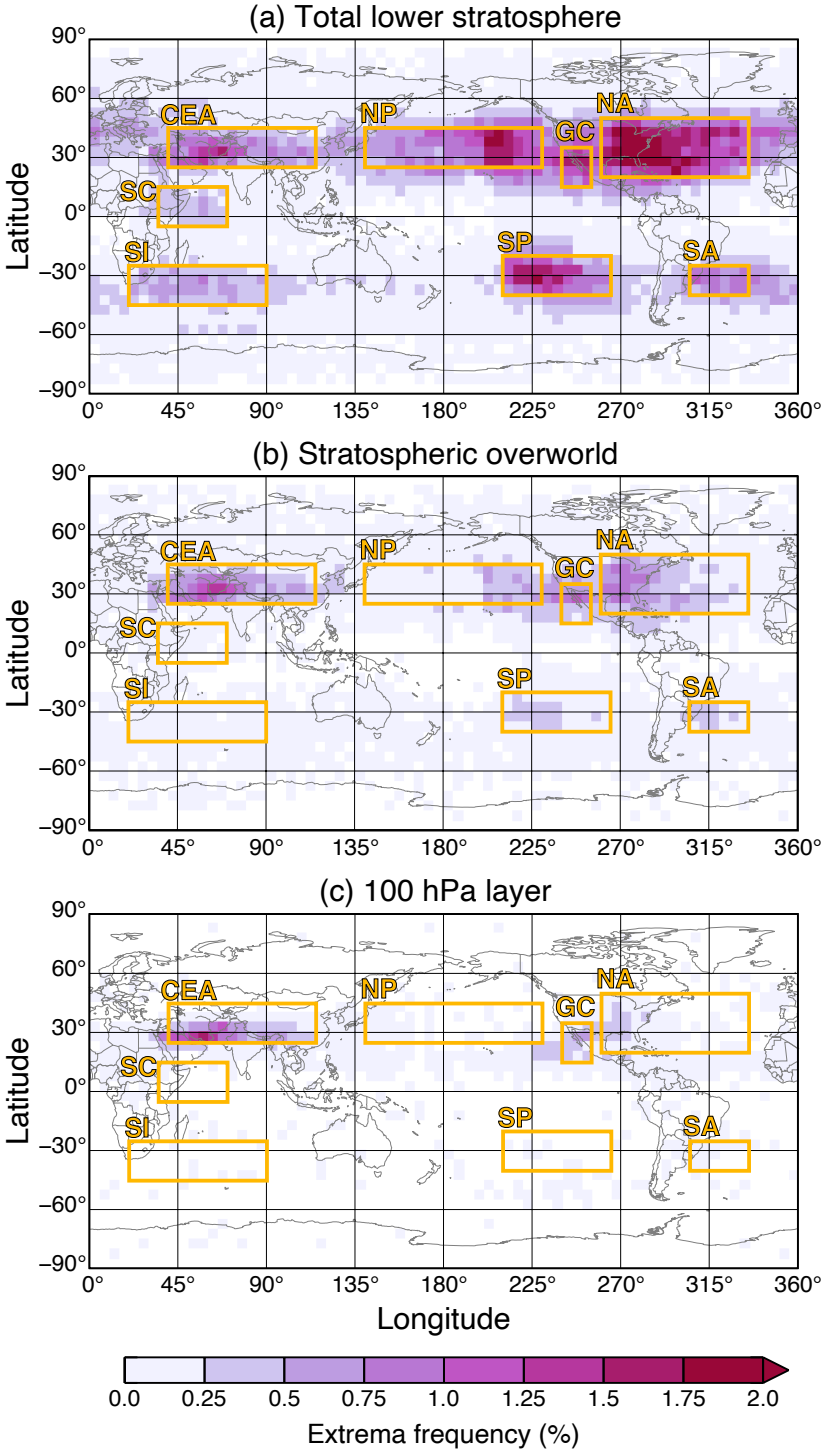

Figure 2.1: Binned frequency of H_2O extrema ($\geq$ 8 ppmv) as observed by MLS for (a) layers classified as stratospheric, (b) overworld layers only, and (c) the 100 hPa layer only. Eight local maxima are classified into regions (gold) for further analysis.

2.3.1 Extrema Frequency

The frequency of H_2O extrema in the total LS (overworld + LMS) and the overworld only is shown in Fig. 2.1a and b. Over most of the world, H_2O concentrations exceeding 8 ppmv in the stratospheric overworld occur less than 0.25% of the time. There are six notable geographic features where the frequency of extrema is maximized which are highlighted and subjectively classified into regions here: Central and Eastern Asia (CEA), the North Pacific (NP), the South Pacific (SP), the Gulf of California (GC), North America and the North Atlantic (NA), and finally South America and the South Atlantic (SA). The maximum frequency of overworld H_2O extrema in each of these regions varies from ∼0.25–1.25%. The CEA feature is the most pronounced in its spatial extent and magnitude, followed closely by the NA feature.

When this analysis is extended to include the LMS, the magnitude and spatial extent of nearly every feature increase, although the strength of the frequency change is variable across the domain (Fig. 2.1a). The NA, GC, NP, and SP maxima experience the greatest increases in frequency magnitude, exceeding 2% in some locations which is more than double that of their overworld counterparts. The SA feature displays a modest increase in frequency, with a maximum frequency of 1.25%. Notably, the magnitude of extrema in the CEA region is minimally impacted by the inclusion of the LMS, which results in the central Asia maximum being one of the least pronounced features in the total LS, despite being the dominant region in the overworld only analysis. This result is consistent with previous work showing that tropopause heights are anomalously high in the region and season of the Asian Monsoon Anticyclone, leading to a shallow — or non-existent— LMS in this region (Munchak and Pan 2014). There are also two additional maxima that become apparent with the inclusion of the LMS: along and just east of the Somalian Coast (SC), and over the Southern Indian Ocean (SI). These features were not detectable in the overworld only analysis where,

like in much of the rest of the world, the occurrence of H_2O extrema did not exceed a frequency of 0.25%. However, these maxima become comparable to the CEA feature in the total LS analysis, with extrema frequencies reaching up to ∼1%. In addition to changes in the magnitude of H_2O extrema frequencies in the total LS analysis for most features, the spatial extent of most features increases as well. Specifically, the features tend to be elongated zonally from their position in the overworld. This can most clearly be seen in the NA and SA features extending eastward over the Atlantic, and the NP feature extending westward to far eastern Asia. This pattern of local extrema hot spots followed by downstream plumes of decreasing frequency is reasonable given typical mixing timescales (5–7 days; Homeyer et al. 2011) and average LS zonal flow. Put simply, a large initial H_2O enhancement can be detectable for days as it is transported downstream before being fully mixed into the background stratosphere. Finally, it is important to note that all regions were subjectively chosen based on the locations of maxima in the total lower stratosphere analysis.

The prominent features over North America (both the NA and the GC regions), Asia (the CEA region), and South America (the SA region) have been seen in previous studies of MLS H_2O extrema at the 100 and 82.5 hPa levels, and they have been linked to convective sources associated with the monsoon anticyclone circulations on these continents (e.g., Werner et al. 2020; Schwartz et al. 2013). In contrast, the maxima over the Pacific (the NP and SP regions) and over the Indian Ocean (the SC and SI regions) have never been identified. This, combined with no major local convective features identified in previous analyses (e.g., Liu et al. 2020), may lead to some concerns that this result could be a nonphysical artifact of or error in the analysis. For this reason, this analysis is also applied to the 100 hPa layer only to allow for a comparison to previous work (Fig. 2.1c). These results are nearly identical to those

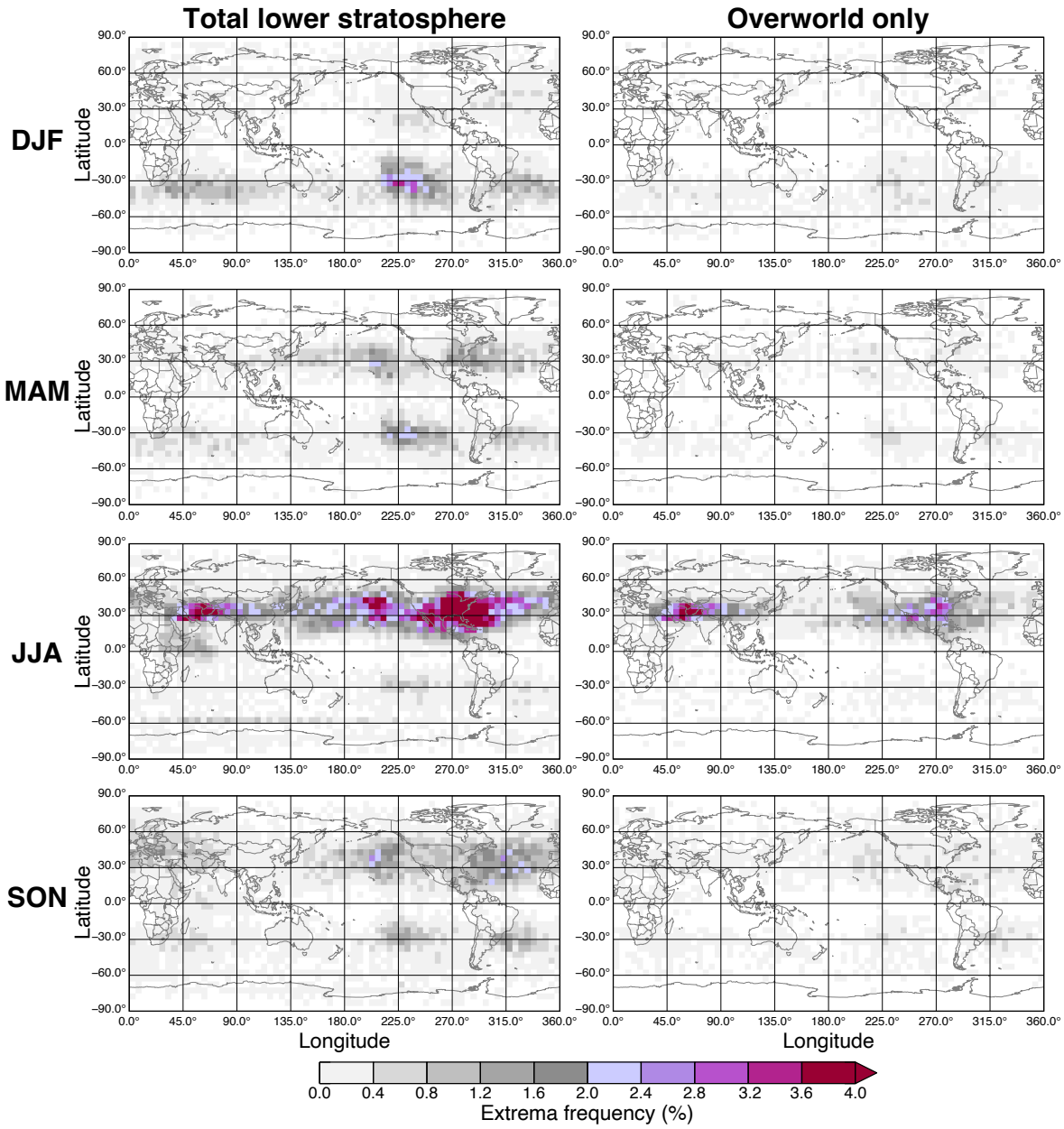

Figure 2.2: Binned frequencies of MLS H_2O extrema ($\geq$ 8 ppmv) separated seasonally into December, January, and February (DJF; top row), March, April, and May (MAM; second row), June, July, and August (JJA; third row), and September, October, and November (SON; bottom row) for (left) lower stratospheric layers and (right) stratospheric overworld layers only.

shown in Werner et al. (2020) and Schwartz et al. (2013), with minor differences likely accounted for by the length of the MLS record used, bin sizes, and previous choices to exclude certain anomalous events that were not made here. Most importantly, the NP, SP, SC, and SI are not found in the 100 hPa only analysis. The similarity of the analysis presented here to the results in Schwartz et al. (2013) and Werner et al. (2020) provides confidence that the previously unseen features are not due to analysis error, but rather due to the inclusion of additional MLS layers that can be classified as stratospheric. However, the presence of the LMS in the deep tropics where the SC region is located is — by definition — non-existent, which leads to a question of how the total LS analysis indicates a local maximum over this region when it is not present in the stratospheric overworld. This is investigated further in the transport analysis below.

A seasonal breakdown of the H_2O extrema patterns is shown in Fig. 2.2. In the Northern Hemisphere, JJA dominates the annual cycle in both the total LS and the overworld. In the NA and NP regions, the frequency of H_2O extrema in JJA far surpasses that of any other season, with more than 4% of total LS observations exceeding 8 ppmv. The westward extent of NP maxima seen in Fig. 2.1 is even more evident when restricted to JJA only. MAM and SON have modest contributions to Northern Hemisphere extrema and are most substantial over the NP and NA regions, while DJF (boreal winter) frequencies are $< 0.4\%$ across nearly the whole of the Northern Hemisphere. The significance of the Asian Monsoon Anticylone is made apparent in the total LS seasonal analysis where the CEA maximum is pronounced in JJA, while other features — such as NA maxima — are present in all seasons except for DJF. In the stratospheric overworld, however, locations over CEA and the NA regions exceed an extrema frequency of 0.8% in JJA only.

In the Southern Hemisphere, DJF (austral summer) has the most prominent contribution to both LS and overworld extrema, though the overall annual cycle is far less clear than that of the Northern Hemisphere. The SP region is the dominant feature of the DJF analysis, with frequencies exceeding 2–3% throughout the region. The SI and SA maxima are also noticeable in the DJF total LS analysis, though their frequencies remain below 1.6%. Similarly to their contributions in the Northern Hemisphere, MAM and SON feature modest frequencies of H_2O concentrations exceeding 8 ppmv in the Southern Hemisphere, with the maximum over South America being the only notable feature in addition to that over the Pacific. Finally, Southern Hemisphere extrema in JJA (austral winter) are exceedingly rare.

2.3.2 Transport Characteristics

To provide context for the extrema observations described above, the recent transport behavior of all LS H_2O extrema located in the eight regions identified in Fig. 2.1 are investigated via an isentropic backward-trajectory analysis for the season in which the feature is most pronounced. This analysis serves as a complement to the extrema climatology presented above and allows us to investigate potential sources of extreme LS H_2O. I show here and discuss in detail the statistical transport for a well-known H_2O frequency maximum (the CEA region), and two unexpected maxima (the NP and SC regions). The transport analyses for the remaining regions are located in Sect. 2.3.3.

The statistical transport behavior of H_2O extrema located in the CEA region during JJA is shown in Fig. 2.3. Throughout the 10 day history, the vast majority of trajectory particles remain over Asia indicating that the extrema air was confined within the summertime Asian Monsoon anticyclone throughout its recent history. As expected,

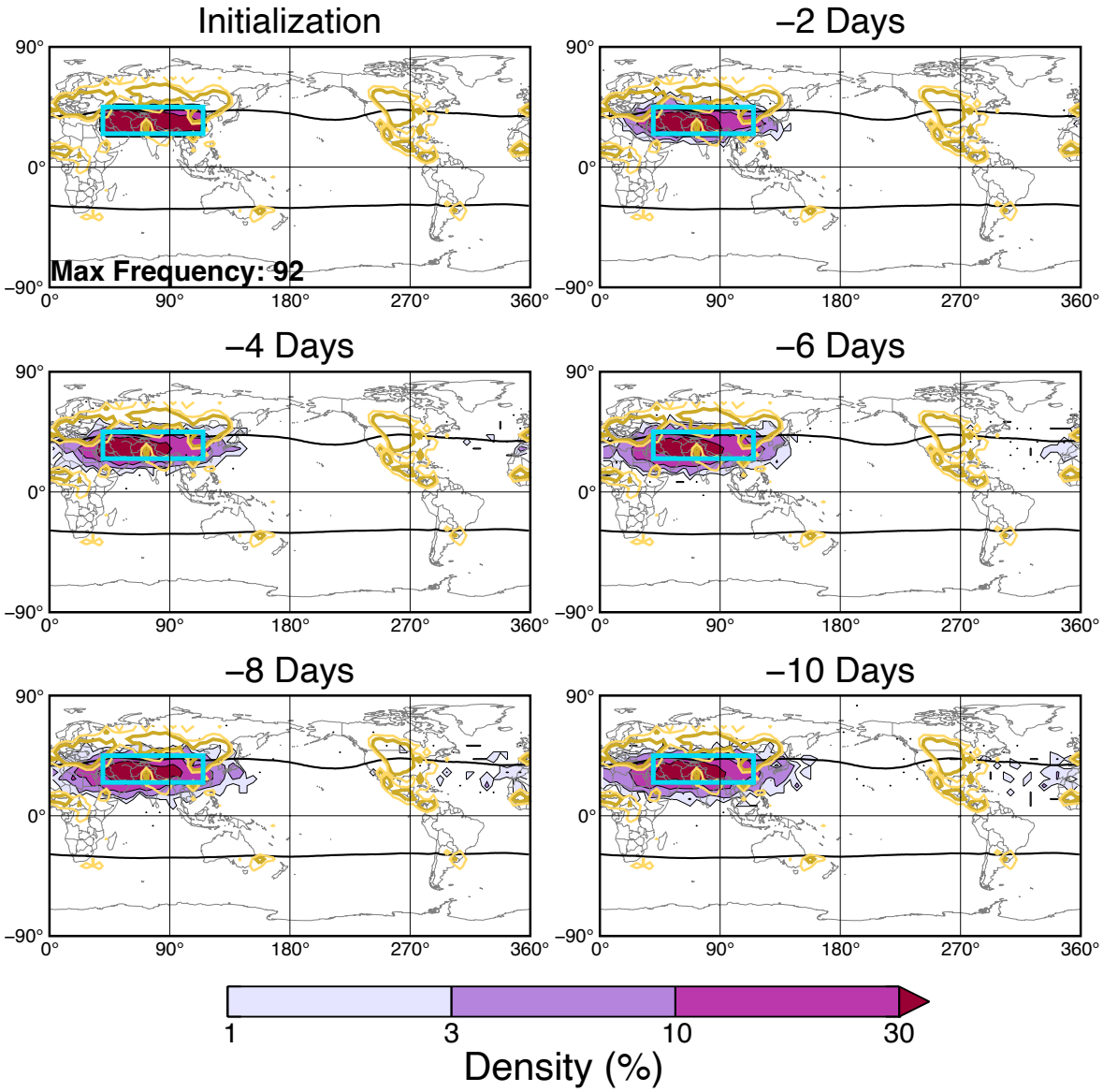

Figure 2.3: Isentropic backwards trajectory analysis for H_2O extrema in the CEA region (blue box) in JJA. The normalized density of trajectories at initialization and at 2, 4, 6, 8, and 10 days prior is shown by the color-fill, with the maximum density value given in the initialization panel. The seasonal frequency of tropopause-overshooting convection as detected by GPM is given by the golden contours at intervals of $5 * 10^{-5}$ overshoots per observation (lighter gold) and $10 * 10^{-5}$ overshoots per observation (darker gold). The seasonal average tropopause break (i.e. the location of the sharp discontinuity between tropical and extratropical tropopause heights) for each hemisphere is indicated by the solid black line.

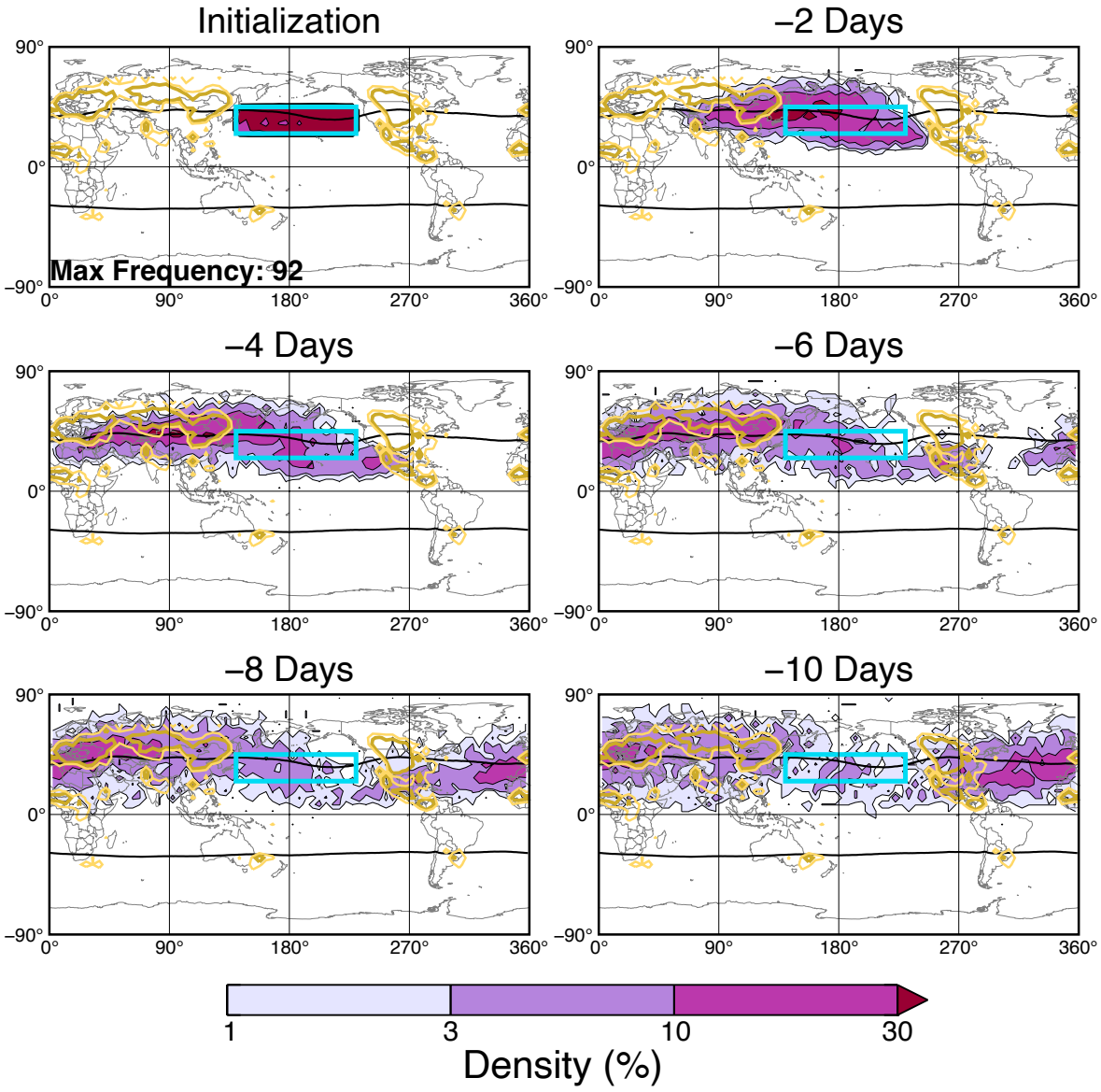

Figure 2.4: As in Fig. 2.3, but for the NP region in JJA.

and consistent with previous studies (e.g., Bergman et al. 2013; Khaykin et al. 2022), this demonstrates that the frequent high LS H_2O concentrations over this region are related to a combination of monsoon dynamics and convection. It is important to note, however, specific convective moistening of the particles along the trajectory path may have occurred before or at any time during the preceding 10 day period, as convective transport is not captured by these large-scale isentropic trajectories. For the NP maxima, transport is largely zonal along the subtropical jet axis (Fig. 2.4). At 4 days prior to the extrema observation, the highest-density area of trajectory particles is located over active overshooting convection areas across Asia, Siberia, and southern Russia as observed by GPM, suggesting that convective moistening is a likely contributor to these extrema. A smaller, but still substantial, portion of trajectories can be traced back eastward to Central American convection 4 to 6 days prior. As demonstrated in Figs. 2.1 and 2.2, the frequency of H_2O extrema in the eastern half of the defined NP region is approximately double that of the western half. This transport analysis suggests that Central American convection related to the North American Monsoon Anticylone is at least partly responsible for the high frequency of extrema over the eastern North Pacific, which is consistent with recent work (Clapp et al. 2021). Another potential source for high LS H_2O concentrations over the NP worth investigating would be poleward Rossby wave breaking transport of tropical/subtropical upper troposphere air. The North Pacific is a location of frequent Rossby wave breaking (Homeyer and Bowman 2013), and poleward wave breaking has the potential to transport relatively moist, tropical upper tropospheric air into the lowermost stratosphere and contribute to this maximum (Langille et al. 2020). However, the lack of substantial meridional transport from the tropics (i.e., equatorward of the average tropopause break latitude) related to the observed extrema, outside of the aforementioned path from Central America,

suggests that this method of stratospheric hydration may be limited when it comes to H_2O concentrations exceeding 8 ppmv.

Finally, the transport history of the SC local maximum is shown in Fig. 2.5. As mentioned above, the existence of relatively high frequencies of H_2O extrema in the SC region in the total LS analysis, but not the overworld only analysis, is theoretically impossible, as the LMS does not exist in the deep tropics. The transport behavior indicates that this air largely originated from southeast Asia as recently as two days prior, and was located within the monsoon circulation for the preceding 10 days. The path of these trajectories largely resembles equatorward wave breaking of midlatitude LMS air along the eastern portion of the monsoon anticyclone shown in previous studies (e.g., Konopka et al. 2010). The transport of this air into the deep tropics would retain some characteristics of its source region for up to 1 week, namely higher PV and potential temperature, which is likely what allows for this air to meet the threshold requirements set here and be identified as LMS though it is encompassed by tropical upper troposphere air. Additionally, LRT altitudes in this region are frequently identified as lower than in other regions located along the same latitude band (not shown), again suggesting a modification confined to this region due to monsoon dynamics.

To provide additional insight into the potential sources of LS H_2O extrema, the cross-tropopause transport nature of the isentropic trajectories is analyzed to assess the likelihood of large-scale moistening (rather than delivery by tropopause-overshooting convection). As a proxy for large-scale isentropic TST, the percentage of trajectories that spent at least 72 of the 120 hours prior to extrema observation within the troposphere in each season is shown in Fig. 2.6. The seasonal variation in large-scale TST at any given location appears minimal. However, it is important to note that for each season, data are only shown for bins with at least 20 initialized trajectories,

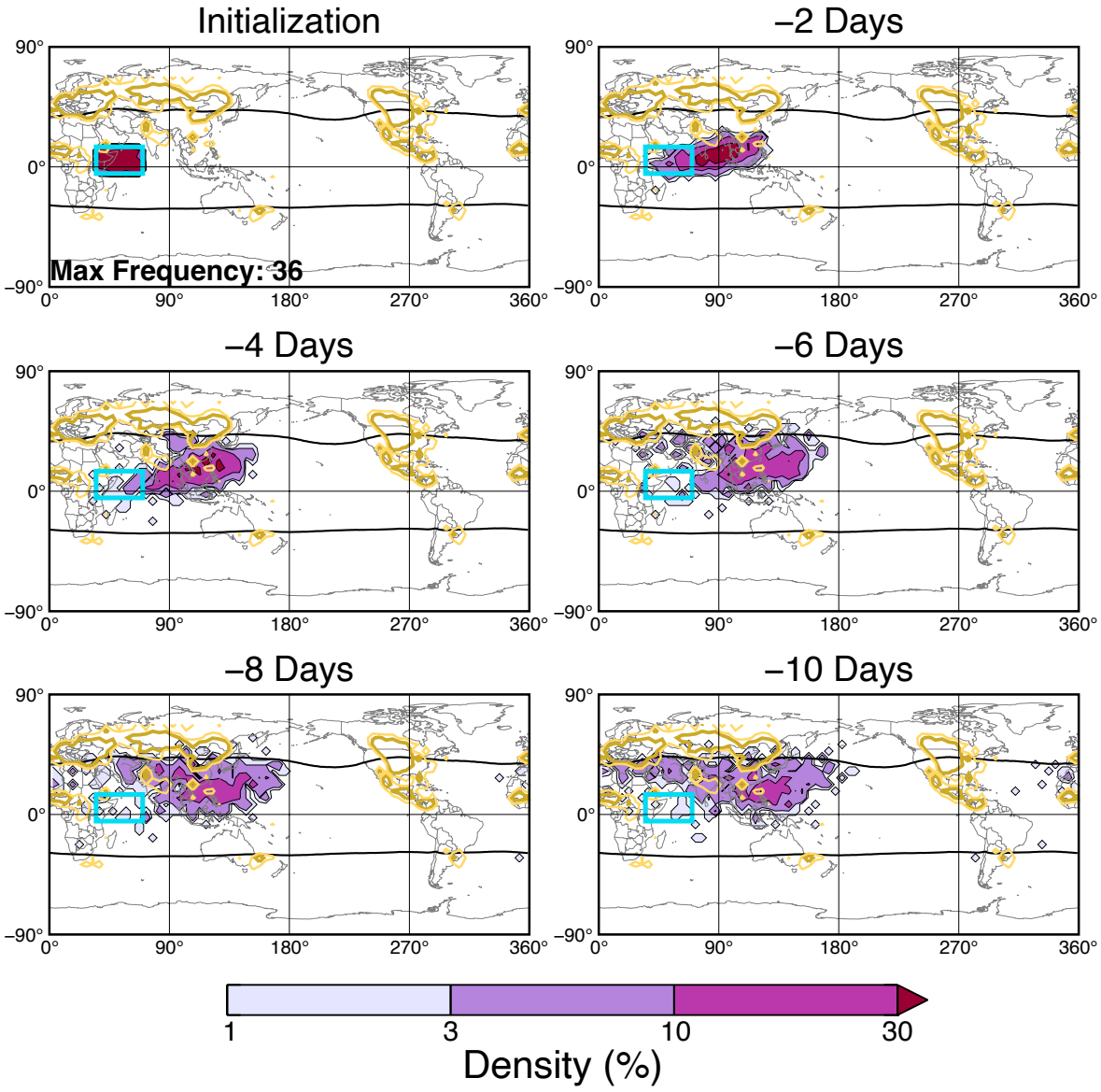

Figure 2.5: As in Fig. 2.3, but for the SC region in JJA.

which could obscure seasonal variation from this analysis. In general, locations over the South Pacific, southern Indian Ocean, the Somalian coast, and the Asian Monsoon region more frequently ($\geq$60%) indicate recent large scale TST, while the northern Pacific and North America have much lower large-scale transport percentages (<40%).

The higher frequency of large-scale TST over the Asian monsoon region (>80% in some places) is consistent with recent studies that have shown the importance of monsoon dynamics in stratospheric moistening over Asia, where monsoon convection often moistens the upper troposphere but additional monsoon-driven isentropic cross-tropopause transport is required to extend these impacts to the stratosphere (e.g., Randel et al. 2010; Pan et al. 2016; Honomichl and Pan 2020; Pan et al. 2022). Alternatively, the lower percentages common throughout the rest of the Northern Hemisphere subtropics and extratropics suggest that direct convective moistening via overshooting is the primary driver of these extreme concentrations. In some locations, like over North America extending eastward into the North Atlantic, this adds to the body of work which has shown that convection over North America is particularly capable of moistening the lowermost stratosphere (e.g., Randel et al. 2012; Tinney and Homeyer 2021).

On the other hand, the low frequencies of large-scale TST for the summertime band of extrema from 180–225°E longitude over the northern Pacific are somewhat surprising given that this is a location of frequent Rossby wave breaking in boreal summer (Homeyer and Bowman 2013). However, this is in line with the analysis shown in Fig. 2.4 which has a lack of meridional transport from the tropics outside of a pathway of summertime transport from Central American convection, which suggests poleward Rossby wave breaking is not a substantial contributor for LS H_2O concentrations greater than

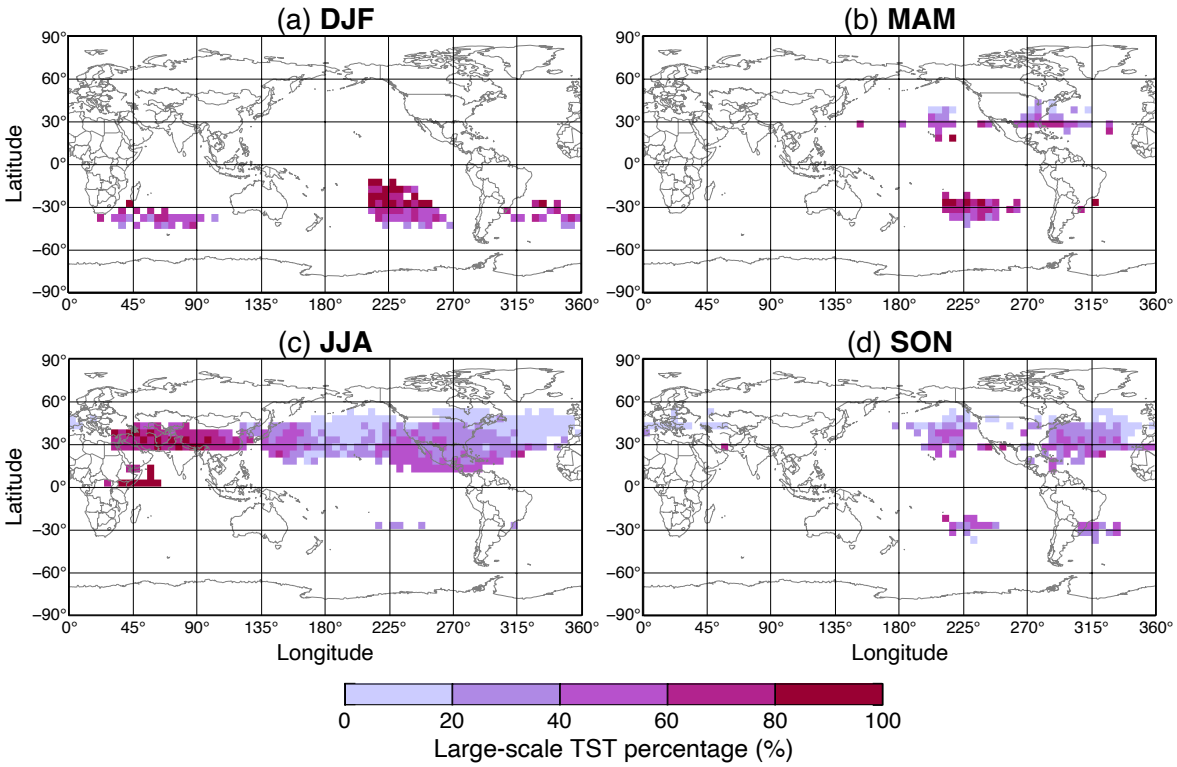

Figure 2.6: The binned percentage of H_2O extrema trajectories classified as large-scale TST at their initialized location for (a) DJF, (b) MAM, (c) JJA, and (d) SON. To restrict the analysis to bins with sufficient sampling of extrema, percentages are only shown for bins with ≥ 20 observations for the corresponding season.

8 ppmv. The significance of the contribution of Rossby wave breaking events to stratospheric H_2O concentrations has been debated in previous work (e.g., Ploeger et al. 2013). The analysis above suggests that while horizontal transport events between the tropical upper troposphere and extratropical LS via Rossby wave breaking may be common in this location, the air involved in associated TST is not moist enough to substantially contribute to the populations of H_2O extrema analyzed here.

2.3.3 Transport in Additional Regions

The statistical backward-trajectory transport analysis described and shown for the CEA, NP, and SC regions in the previous subsection is presented and briefly discussed here for the remaining regions. Figures 2.7–2.9 show back-trajectory density maps for H_2O extrema in the NA, SA, and GC regions. These regions are all characterized by rapid transport of extrema observations to active overshooting convection regions upstream and spatially adjacent to the extrema locations, implying that MLS is capturing H_2O enhancements from convection at times shortly after the storms. For the NA region, overshooting over the US Great Plains, Gulf of Mexico, and — at longer transport times — the Mediterranean, are likely contributors (with significance in that order). For the SA region, overshooting in Argentina is most likely responsible. For the GC region, overshooting over the Sierra Madre Occidental in Mexico and the Gulf of Mexico are likely contributors. In contrast with these apparently dominant local convective sources, transport pathways of H_2O extrema in the SP region (Fig. 2.10) are not linked to a clear overshooting source region but are densely sourced from the equatorward side of the mean tropopause break location. This behavior suggests that many of the H_2O extrema in that region are facilitated in part by large-scale TST. It is noted, however, that SP extrema transport bypasses the South Pacific Convergence Zone (SPCZ), which is one of the more globally active convective regions in DJF (when

SP extrema are most common; Vincent 1994, and references therein). Thus, it is possible that H_2O extrema in this region are the result of large-scale transport of UT air hydrated by convection over the SPCZ to the LS over the east Pacific. Finally, transport histories for H_2O extrema within the SI region (Fig. 2.11) indicate rapid linkages to two upstream overshooting convection sources along the mean tropopause break location (i.e., the subtropical jet) within 2–4 days: southern Africa and Argentina.

2.3.4 Annual Cycles in Monsoon-Related Regions

Monsoon dynamics and circulations have a unique and substantial impact on LS H_2O extrema. The seasonal nature of monsoon circulations motivates additional analysis of the annual cycle of LS H_2O extrema in monsoon-related regions, with a goal of providing further insight into the relationship between monsoon circulations and LS H_2O extrema. In particular, analysis is focused on the Asian Monsoon Anticyclone (AMA; 20°N – 40°N, 30°E – 130°E), the North American Monsoon Anticyclone (NAMA; 20°N – 45°N, 230°E – 290°E), and the South American Monsoon Anticyclone (SAMA; 20°S – 40°S, 260°E – 320°E). Note that these region boundaries are different from those defined and discussed previously, as those were subjectively chosen based on local maxima of LS H_2O extrema frequency and do not necessarily align with the tropopause-level monsoon circulations. These monsoon regions, shown in Fig. 2.12d, were specifically chosen to encapsulate their associated tropopause-level anticyclonic circulations as indicated by the climatological mean of hemispheric summer 100 hPa winds in reanalysis (not shown).

While the frequency of H_2O extrema peaks in summer and decreases in winter for each monsoon anticyclone, the characteristics of each cycle vary substantially. Both

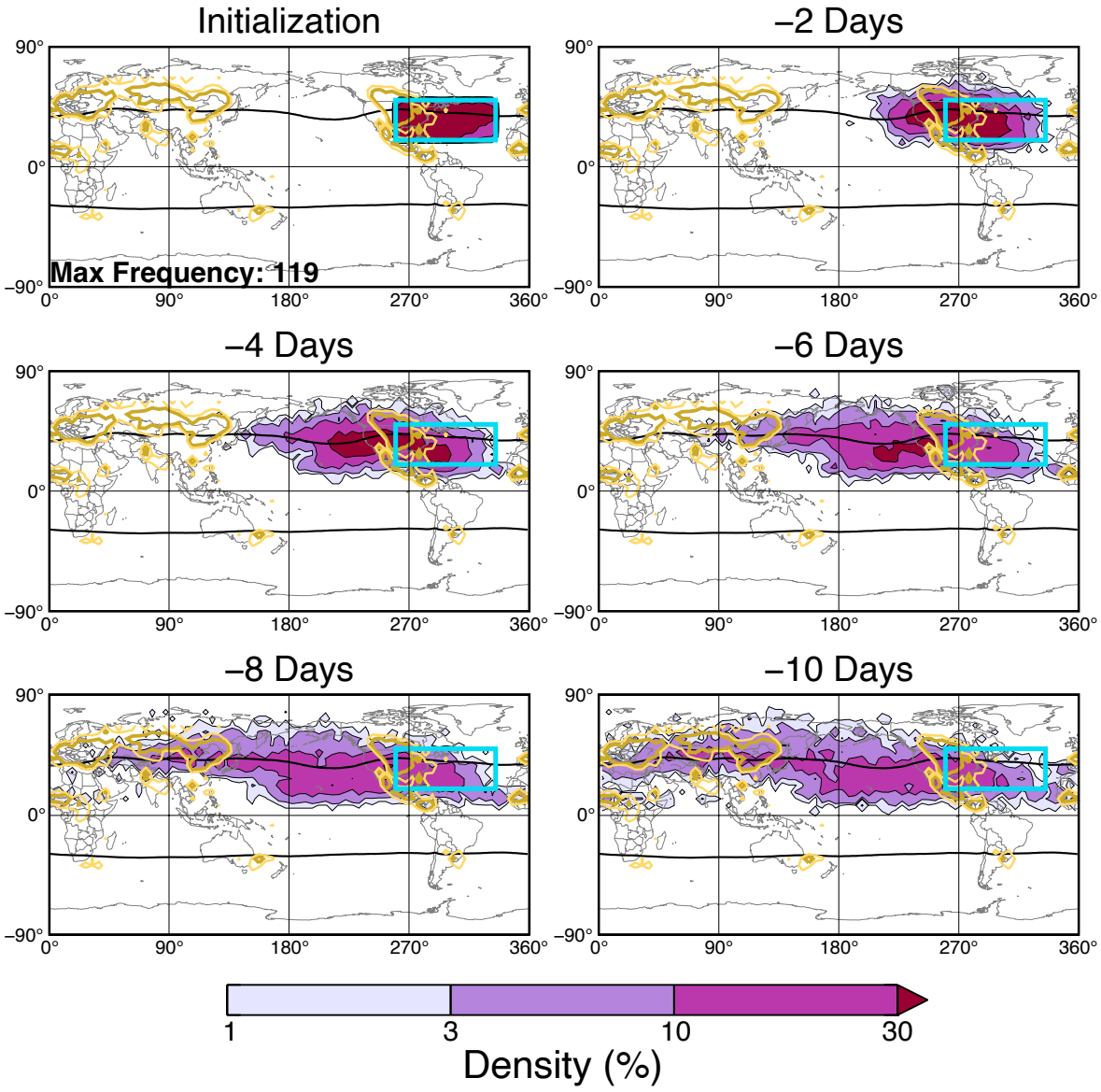

Figure 2.7: As in Fig. 2.3, but for the NA region in JJA.

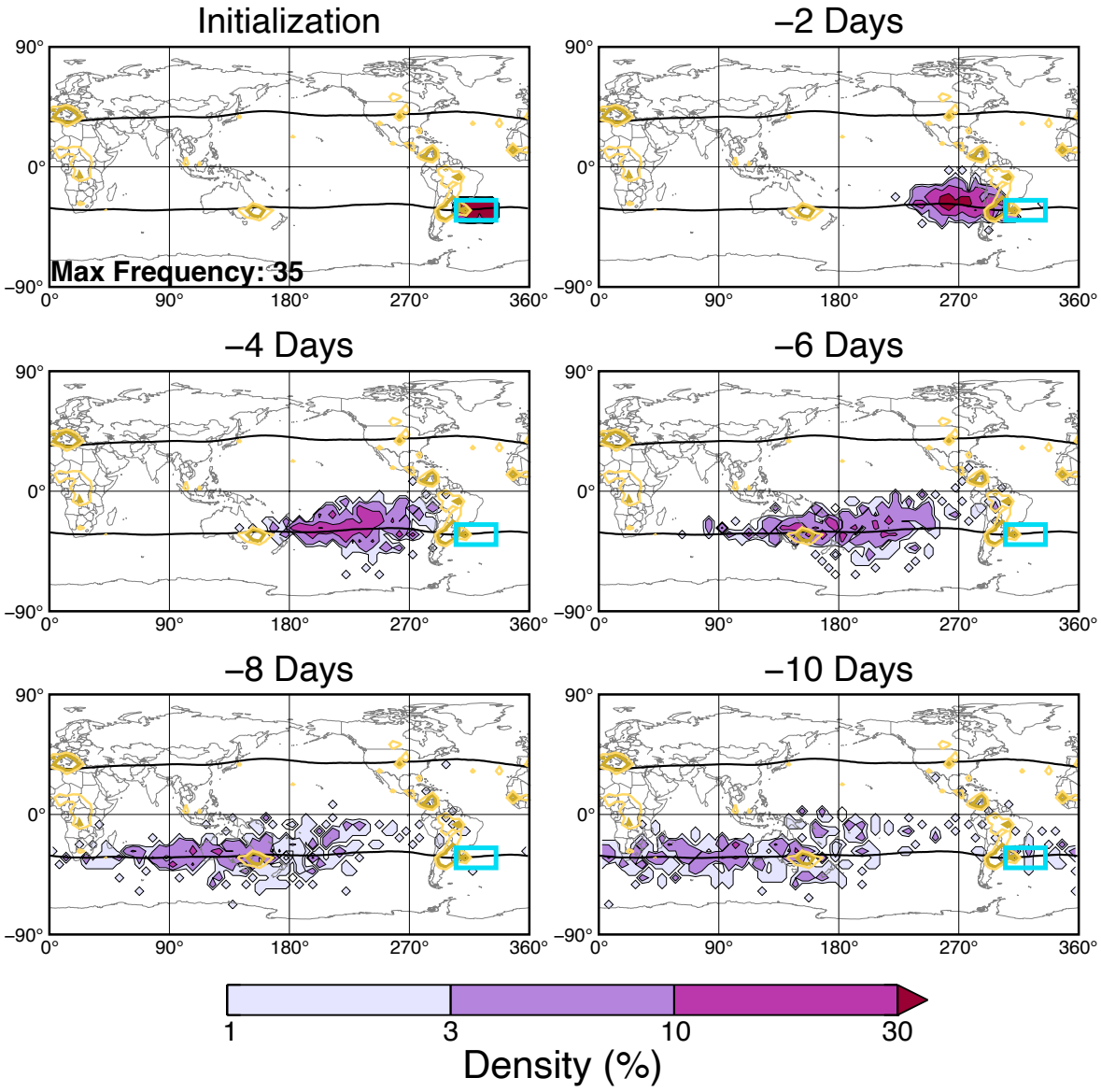

Figure 2.8: As in Fig. 2.3, but for the SA region in SON.

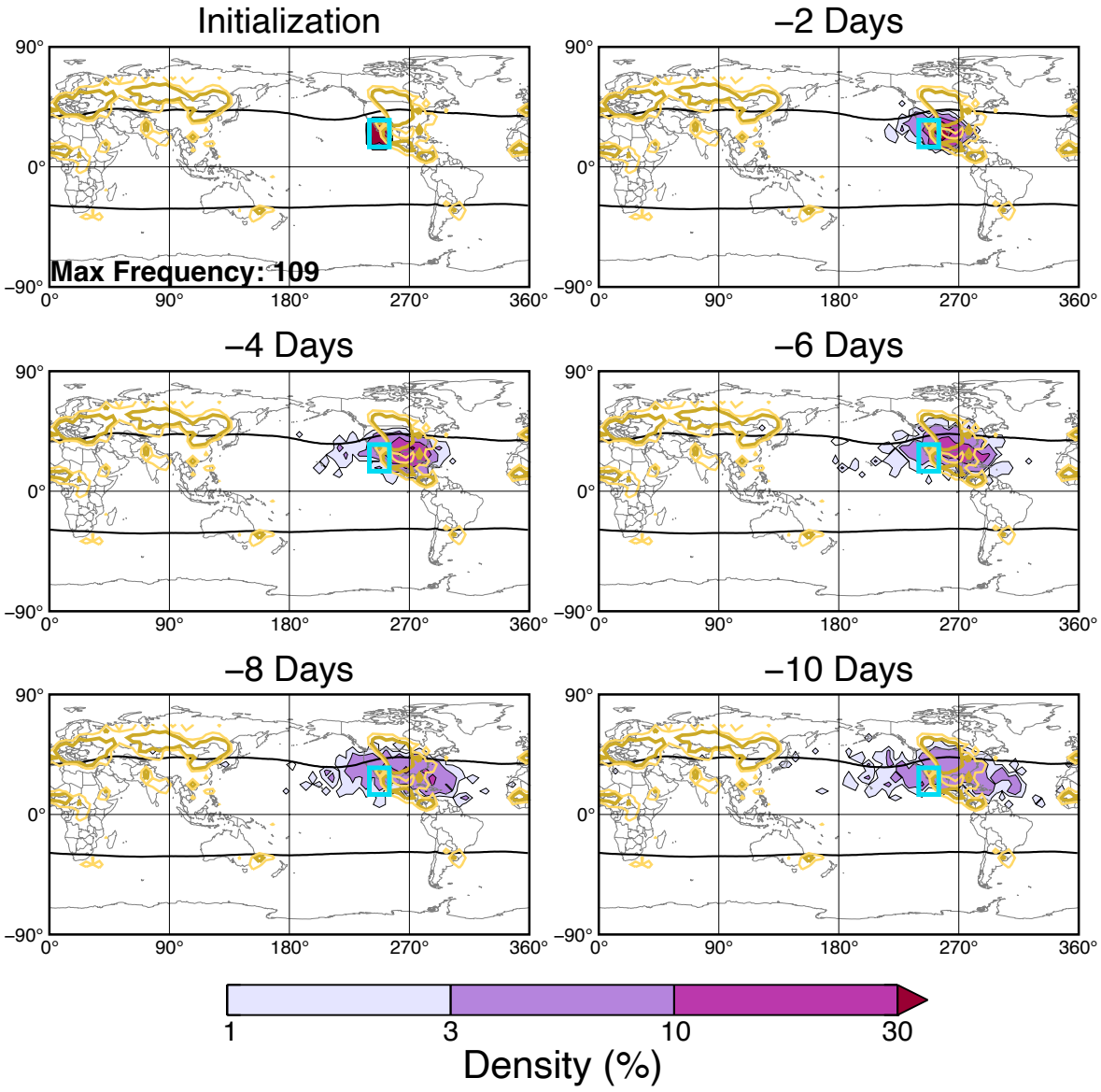

Figure 2.9: As in Fig. 2.3, but for the GC region in JJA.

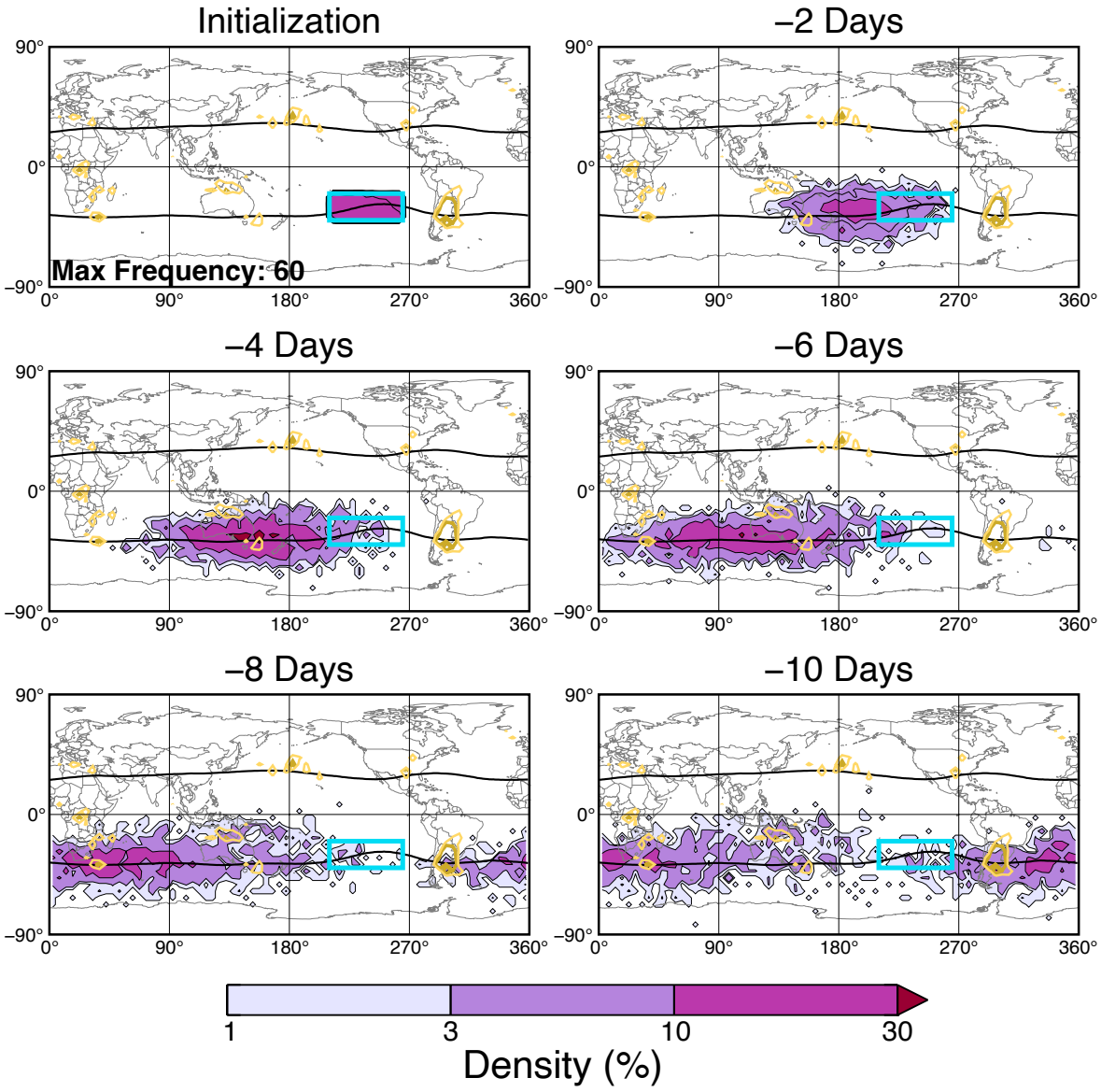

Figure 2.10: As in Fig. 2.3, but for the SP region in DJF.

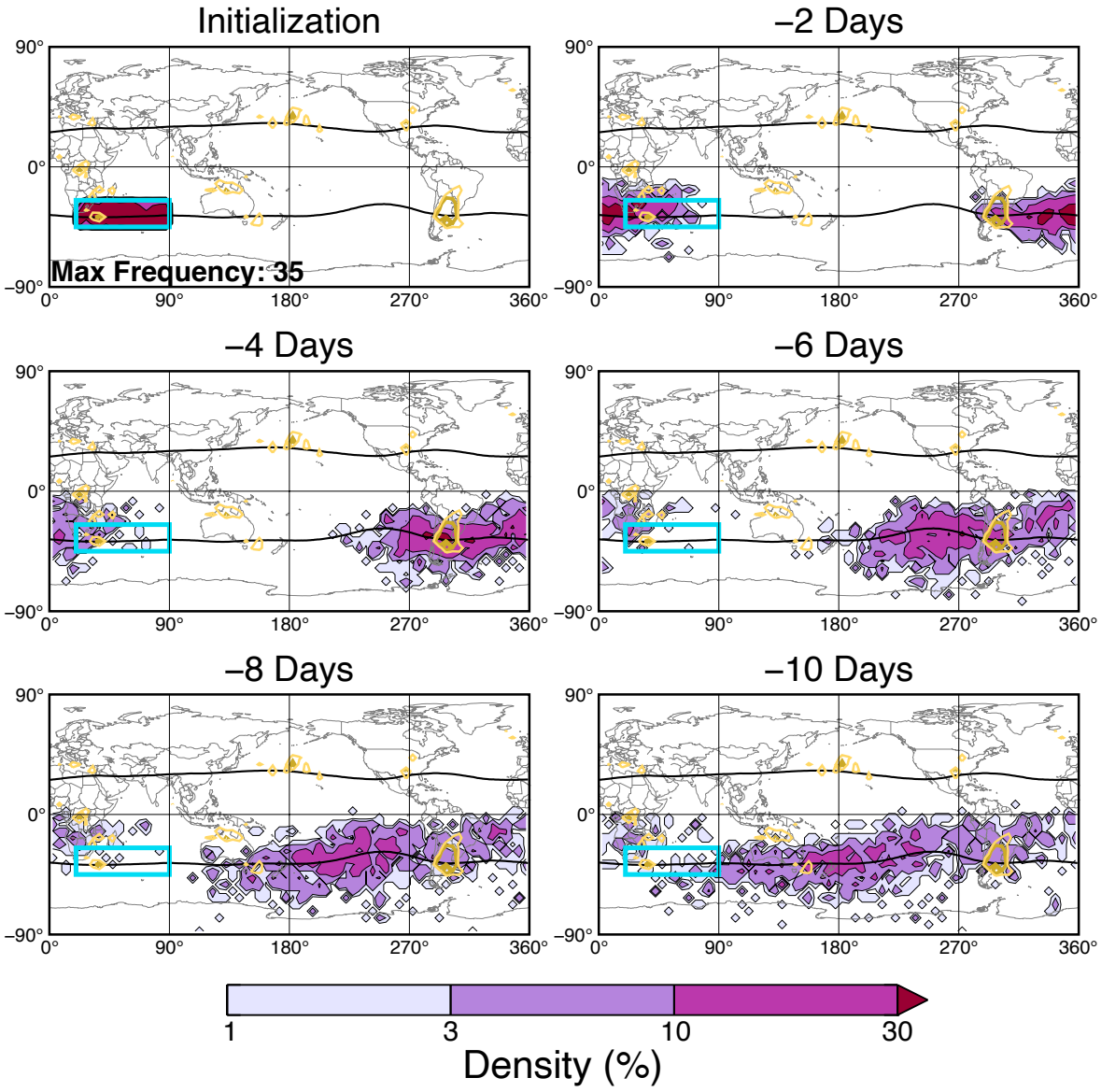

Figure 2.11: As in Fig. 2.3, but for the SI region in DJF.

when normalizing for region size (Fig. 2.12a) and when not (Fig. 2.12b), the frequency of LS H_2O extrema in AMA and NAMA is an order of magnitude larger than in SAMA at their respective peaks. The SAMA annual cycle is characterized by a broad, shallow peak from October to January (hemispheric spring and summer) with a maximum average of ∼0.2 observations per grid point. For NAMA the occurrence of LS H_2O extrema largely exists between April and October (hemispheric late spring to early fall), peaking in August at a maximum average of ∼1.7 observations per grid point. Alternatively, AMA extrema primarily exist within boreal summer (JJA) and peak in July at ∼1.0 observations per gridpoint. From a per grid point standpoint, the NAMA region clearly dominates contributions to LS H_2O extrema in both magnitude of the frequency and the longevity compared to AMA and SAMA, likely as a result of combined contributions from monsoon-driven deep convection near the Sierra Madre Occidental in northwest Mexico and additional frequent convection in the central and eastern United States during spring, summer, and fall. When comparing the monsoons as a whole and allowing for their size to modulate their contributions, the NAMA region still exhibits the greatest H_2O extrema frequency, though AMA is more comparable in its total number of extrema observations (Fig. 2.12b). Perhaps even more notable is the disparity between the proportion of total LS versus overworld only extrema in each region. For NAMA and SAMA, the overall overworld contributions to the total LS extrema frequency is less than 50%, while more than 90% of AMA LS H_2O extrema are from the stratospheric overworld, which reflects the anomalously high tropopause heights in this region (Munchak and Pan 2014). This result especially highlights the importance of considering the LMS when assessing the contributions of each monsoon to extreme H_2O concentrations.

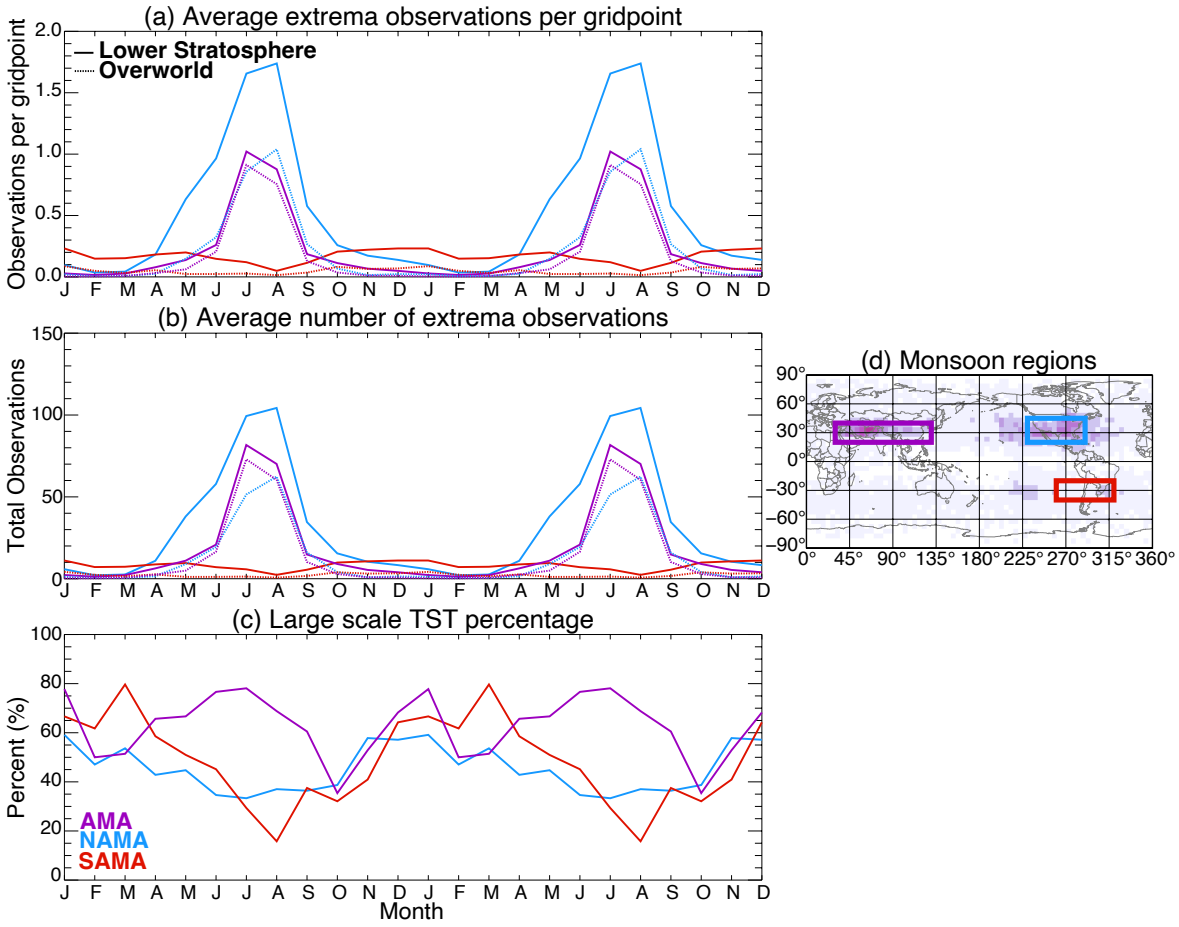

Figure 2.12: Two average annual cycles of (a) the number of H_2O extrema per grid point, (b) the average regional number H_2O extrema, and (c) the percentage of extrema with a large-scale transport history are given for the Asian Monsoon Anticyclone (AMA; 20°N – 40°N, 30°E – 130°E; purple), the North American Monsoon Anticyclone (NAMA; 20°N – 45°N, 230°E – 290°E; blue) and the South American Monsoon Anticyclone (SAMA; 20°S – 40°S, 260°E – 320°E; red). For (a) and (b), the number of observations for the total lower stratosphere is given by the solid line and the number of observations in the stratospheric overworld only is given by the dotted line. The region boundaries for each monsoon described above are given in (d).

Figure 2.12 also shows the percentage of extrema in each monsoon region whose back-trajectory analysis indicates a recent tropospheric origin (as described above). Again, there are substantial differences between the three monsoons. For AMA and SAMA, the large-scale TST percentage peaks during the monsoon season when the frequency of extrema peaks. Alternatively, the NAMA region experiences a minimum in large-scale TST percentage in August when the H_2O extrema frequency peaks, providing more evidence that convection in the NAMA region is uniquely capable of transporting H_2O to the LS without necessitating some additional, larger-scale transport, as has been demonstrated in previous studies (e.g., Randel et al. 2012; Tinney and Homeyer 2021). Both the AMA and the NAMA regions also experience relative maxima in the frequency of large-scale TST in December/January, which is likely a result of the substantial decrease in tropopause-overshooting convection in the winter months.

2.4 Discussion

Throughout this study, several choices and assumptions were necessary for conducting the analysis. For example, using the tropopause-relative location of trajectories as a proxy for large-scale TST can be sensitive to the requirements for the percentage of time spent in the troposphere. In addition to the requirement used here (60% of the preceding 5 days spent in the troposphere), the analysis was performed requiring that trajectories must be located in the troposphere for only 40% of the preceding 5 days. This changed the number of trajectories but did not impact the resulting large scale pathways (not shown). Additionally, while the analysis was conducted for MLS extrema thresholds of 8, 10, and 12 ppmv, only the 8 ppmv results were presented here. In general, the 8 ppmv threshold increased the number of extrema in all regions and all

seasons compared to the more restrictive thresholds. For example, 8 ppmv extrema are typically ∼1–2 times more frequent than 10 ppmv extrema globally. However, the 8 ppmv threshold does disproportionately increase the number of extrema in the CEA–AMA region, where 8 ppmv extrema are ∼3–4 times more frequent than 10 ppmv extrema (not shown). Another sensitivity to the choice of threshold is found when examining the annual cycle of extrema in the NH, where 10 and 12 ppmv extrema frequency peaks in July while 8 ppmv extrema frequency peaks in August (not shown). This slight seasonal shift is likely related to the increase in background stratospheric water vapor concentrations in the summer months (e.g., Tinney and Homeyer 2021). Though these sensitivities are notable, they do not impact the conclusions drawn from the analysis.

Lastly, the biggest challenge for this work arose from the major goal of this study — to expand on previous work through the inclusion of the LMS in analysis of LS composition. Restricting the analysis to stratospheric MLS layers only proved to be a difficult task due to the relatively coarse vertical resolutions of MLS and MERRA-2. For this study, the selected criteria were as lenient as possible while still accounting for the uncertainties within the data. Specifically, to limit contamination from MLS layers whose depth may extend across the tropopause, a series of stringent criteria were put in place and only MLS layers at pressures of 147 hPa were included in this analysis. Despite these efforts, it is possible that upper-tropospheric H_2O could influence parts of the analysis and partially inflate LS extrema frequencies. Alternatively, the stringent criteria may also obscure and prevent truly lower stratospheric layers from being included within this analysis — therefore potentially undercounting extrema. I emphasize here that the inclusion of the LMS in analyses like that presented here is challenging — but worthwhile — and is important to do in future work that aims to increase understanding of the concentrations and sources of H_2O and other trace gases

in the LS, especially given the implications for understanding the role of tropopause-overshooting convection in the STE budget.

Chapter 3

A Modern Approach to Stability-Based Definition of the Tropopause

This chapter is based on and reproduced from the following published peer-reviewed journal article:

> Tinney, E. N., C. R. Homeyer, L. Elizalde, D. F. Hurst, A. M. Thompson, R. M. Stauffer, H. Vömel, and H. B. Selkirk, 2022: A modern approach to a stability-based definition of the tropopause. *Monthly Weather Review*, **150 (12)**, 3151 – 3174, https://doi.org/https://doi.org/10.1175/MWR-D-22-0174.1.

Some sections of Chapter 1 are based upon this article as well.

3.1 Background and Motivation

The assessment of many UTLS-relevant processes, such as the work presented in Chapter 2 and in research focusing on STE, are heavily reliant upon accurately defining the stratosphere. Therefore, definition of the tropopause continues to be an important and challenging task. For example, a tropopause that is identified too high can result in the false assessment of stratospheric air in the troposphere, and vice versa. Ultimately, it is the diverse dynamic, chemical, and radiative coupling between troposphere and stratosphere in the UTLS and the two-way exchange of air via stratosphere–troposphere exchange, which significantly impact Earth's radiation budget and climate, that motivate continued refinement in our approach to tropopause definition (Holton et al. 1995;

Stohl et al. 2003; Gettelman et al. 2011; Banerjee et al. 2019). A variety of unique tropopause definitions have been proposed over the years, each of which can fall within one of three main categories: stability-based definitions, dynamics-based definitions, and composition-based definitions.

Stability-based definitions of the tropopause use profiles of temperature to determine the vertical stratification of the atmosphere. The original and most-used stability-based definition is that created by the World Meteorological Organization (WMO) in 1957. The temperature lapse-rate definition of the tropopause (LRT) is defined as "*the lowest level at which the lapse rate decreases to 2°C km^{-1} or less, provided also the average lapse rate between this level and all higher levels within 2 km does not exceed 2°C km^{-1}*" (World Meteorological Organization 1957). This method is one of few globally and universally-applicable definitions (i.e., it can be applied reliably to both balloon observations and model output), although its accuracy can vary seasonally, latitudinally, and under previously-outlined complex synoptic patterns such as tropopause folds and Rossby wave breaking events (Zängl and Hoinka 2001; Homeyer et al. 2010). The most significant and routine errors in tropopause identification using the LRT definition occur in polar regions during hemispheric winter and spring where a stable, near-isothermal middle troposphere and UTLS can prevent the LRT criteria from being met at a level below the lower-to-middle stratosphere, resulting in an erroneously high tropopause altitude (Zängl and Hoinka 2001). Near the subtropical jets and more spatially confined, lamination of tropical tropospheric air and extratropical stratospheric air can result in complex stability profiles that make tropopause definition using any criteria difficult, for which errors in LRT altitude are almost always realized as a high bias and are also unfortunately common (Homeyer et al. 2010). In the tropics, the cold point tropopause (i.e., the UTLS temperature minimum) is a commonly-used definition, but is susceptible to bias from temperature fluctuations driven by wave activity (Kim and

Alexander 2015). Additionally, the cold point tropopause cannot be used poleward of the subtropical jets due to decoupling between the temperature minimum in a profile and the dominant troposphere-stratosphere composition change (e.g., Highwood and Hoskins 1998). In evaluation of modeled convective mass transport, tropopause identification by a potential temperature gradient threshold performed similarly to the LRT, though its potential further use has not been fully explored (Maddox and Mullendore 2018). Other variations of stability-based definitions have also been created in recent years, often leveraging the Brunt–Väisälä frequency N in their identification (Homeyer et al. 2010; Gettelman and Wang 2015; Duran and Molinari 2019). Note that any stability-based definition applied to radiosonde observations can be sensitive to noise and measurement-related artifacts, such as solar heating of the sensor or adsorption of hydrometeors onto the sensor, but these are typically negligible for tropopause altitude definition.

Dynamic definitions of the tropopause are the most popular alternative to thermal (i.e. stability) definitions in the subtropics and extratropics. Potential vorticity (PV) is commonly used as the basis of a dynamic tropopause definition (Reed 1955; Holton et al. 1995; Kunz et al. 2011). PV is the product of static stability and absolute vorticity and is conserved in frictionless, adiabatic flows. While some studies use the gradient of PV along isentropes to identify the dynamic tropopause, it is most often prescribed as a surface of constant PV expressed as a potential vorticity unit, or PVU, where 1 PVU $= 10^{-6}$ K m^2 kg^{-1} s^{-1}. The PV threshold selected often ranges from $\pm$1–4 PVU, with $\pm$2 PVU being most common, but the ideal threshold has been found to vary seasonally and by altitude from model analyses (Hoerling et al. 1991; Wernli and Bourqui 2002; Sprenger et al. 2003; Kunz et al. 2011; Škerlak et al. 2014). The PV-based dynamic tropopause cannot be applied in the tropics where the absolute vorticity approaches zero and PV surfaces become nearly vertical. However, the arguably greatest limitation

of a PV-based dynamic definition of the tropopause is that it is largely gridded-data-based and therefore cannot be applied in many traditional observational studies without additional support of a gridded dataset. Alternative dynamic definitions exist based on trajectory calculations, called a "Lagrangian tropopause" (e.g., Berthet et al. 2007), but these are more computationally expensive and entirely model-based.

Lastly, composition-based definitions of the tropopause use the often dramatic composition change between troposphere and stratosphere to identify a chemical tropopause. Previous observational and modeling studies have leveraged the concentrations of various trace gases, such as–but not limited to–ozone (O_3), water vapor (H_2O), and carbon monoxide (CO), due to their sharp gradients across the tropopause transition layer. These sharp gradients allow the compounds to be considered tracers of stratospheric (O_3) and tropospheric (H_2O, CO) air. Past studies have either used profiles of one of these trace gases—predominantly O_3—or two trace gases to identify the characteristic composition change in the tropopause transition layer. For example, Bethan et al. (1996) used balloon observations of O_3 at select sites around the world to produce an 'ozone tropopause' definition. For two trace gases, plots of coincident tropospheric and stratospheric tracers demonstrating tracer–tracer relationships have become a common technique for a chemical tropopause transition layer definition, with O_3–CO and O_3–H_2O relationships being most common (Fischer et al. 2000; Hoor et al. 2002; Zahn and Brenninkmeijer 2003; Pan et al. 2004). However, such chemical tropopause definitions can be sensitive to transient processes including stratosphere–troposphere exchange, are not able to be applied to common observations such as radiosondes and models without chemistry, and can require adjustment when applied to locations at a wide range of latitudes. Unique approaches to chemical tropopause definition have been explored using models, such as passive tracer concentrations with a tropospheric source

(e.g., Prather et al. 2011), but are ultimately less common and also not applicable to observations.

Despite the wide range of approaches used to identify the tropopause in prior work, the LRT is often characterized as the most reliable definition due to both its universal applicability and superior ability to identify the approximate location of the layer of greatest composition change in the UTLS, both in tropical, high-tropopause regions and extratropical, low-tropopause regions (Gettelman et al. 2011; Pan et al. 2018). The common coincidence of the LRT with the layer of greatest composition change is remarkable, because the LRT definition was developed at a time where coincident profile observations of atmospheric temperature and composition were extremely rare. Recent work has demonstrated that other stability metrics may perform similarly to the LRT, but their potential use and applicability to a wide variety of environments and dynamic scenarios must be further investigated (Maddox and Mullendore 2018). Recognition of this fact and motivated by both the increasing availability of long-term, globally distributed profiles of observed atmospheric temperature and composition, especially O_3 and H_2O, and the known common failure modes of the LRT definition, this study seeks to evaluate the relationship between UTLS composition change and common metrics of atmospheric stability. In doing so, the following questions are addressed: 1) Does the temperature lapse rate best correspond to composition change in the UTLS? 2) Is it possible to improve upon the known limitations of the LRT definition by designing an alternative, universally applicable stability-based tropopause definition? My focus in addressing these questions is on the conventional exercise of identifying a single tropopause level rather than the composition transition layer depth.

To examine relationships between UTLS composition change and stability, 12-40+ years of balloon-based profile observations from six locations ranging in latitude from

the high Arctic to the South Pole are used in this study. These observations include coincident measurements of temperature, O_3, and (in some cases) H_2O. The observations are first used to statistically examine the relationship between UTLS composition (O_3 only) and three commonly-used metrics of atmospheric stability: the temperature lapse rate, vertical gradient of potential temperature, and N. Following this analysis, a new stability-based tropopause definition is proposed, applied to profile observations and reanalysis output in comparison to the LRT, and evaluated through tropopause-relative analysis of O_3 and O_3–H_2O tracer-tracer diagrams.

3.2 Data and Methods

3.2.1 Balloon Observations

High-resolution balloon observations of temperature, O_3, and H_2O used in this study were obtained from NOAA's Earth System Research Laboratories (ESRL) Global Monitoring Laboratory (GML) online archive (NOAA 2021, 5 out of 6 sites) and from NASA's Southern Hemisphere ADditional OZonesondes (SHADOZ) and Network for the Detection of Atmospheric Composition Change (NDACC) archives (NASA 2022a,b, for the Costa Rica site only). These data include traditional radiosonde observations of air temperature, pressure, and humidity in all cases and one or both of the following instruments, depending on the flight: an electrochemical concentration cell (ECC) ozonesonde for measuring O_3 with an accuracy of ±5% and a precision of ±3–4% (Witte et al. 2017; Thompson et al. 2017; Witte et al. 2018; Sterling et al. 2018) and/or a NOAA frost point hygrometer (FPH; Hurst et al. 2011) or cryogenic frost point hygrometer (CFH; Vömel et al. 2007) for measuring tropospheric and stratospheric H_2O with total uncertainties of ±10% and ±6%, respectively (Hall et al. 2016; Vömel et al.

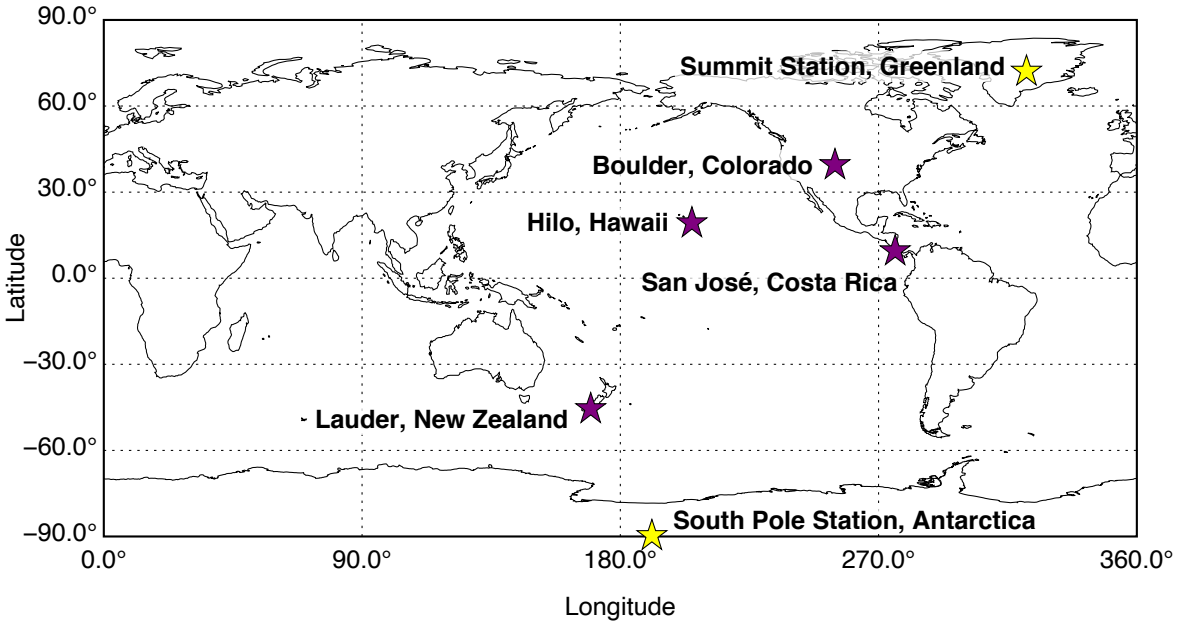

Figure 3.1: Sites of the balloon observations used in this study. Yellow stars indicate sites with ozonesonde-only observations and purple stars indicate sites that also have water vapor data.

2016). Note that while the radiosonde data include humidity measurements for all profiles, these data are not suitable for detailed analysis of H_2O composition in the UTLS given the well-established need for corrections of measurement biases and slow sensor response times (e.g., Miloshevich et al. 2004). Regardless of the composition instrumentation used, every balloon carried a radiosonde and most reached altitudes >30 km, providing measurements of meteorology and composition throughout the troposphere and lower stratosphere. For ECC and radiosonde flights, O_3 and temperature measurements reported at a vertical data spacing of 5–10 m were averaged in 100-m vertical layers, while for flights that also included a FPH/CFH, the 5–10 m-spaced measurements of H_2O, O_3 and temperature were averaged in 250-m vertical layers. Many of the flights that include both FPH/CFH and ECC instruments are also available in the ECC-only datasets. In such cases, only the multi-instrument 250-m layer data is retained for analysis to prevent double counting. For consistency, all 250-m

layer data are linearly interpolated to 100-m vertical grid spacing prior to analysis. For either dataset, only the ascent (i.e., generally higher quality) observations are used for analysis.

To explore relationships between stability and composition across a wide range of latitudes, five NOAA ESRL GML balloon sounding sites and one NASA site were selected for analysis in this study, which are: Summit Station, Greenland (72.58°N); Boulder, Colorado (39.95°N); Hilo, Hawaii (19.72°N); Lauder, New Zealand (45.04°S); South Pole Station, Antarctica (90.00°S); and San José, Costa Rica (∼10°N), respectively. Latitude was used as the basis for balloon sounding site selection because it is the leading factor of global variability in tropopause altitude and UTLS composition (e.g., Gettelman et al. 2011). The Boulder, Hilo, San José and Lauder balloon sounding sites include measurements with both ECC and FPH/CFH instruments, while the Summit and South Pole sites are ECC(O_3)-only. Figure 3.1 shows a map of these balloon sounding sites and Table 3.1 summarizes the number of flights from each site at least 18 km in depth from the surface that are used for analysis in this study.

Table 3.1: The total number of balloon observations at least 18 km in depth by type (ECC or O_3-only, FPH/CFH or H_2O-only, and both) and location.

Observation Site	**O_3-only**	**H_2O-only**	**O_3 & H_2O**
Boulder, Colorado	1678	284	241
Hilo, Hawaii	1612	5	126
Lauder, New Zealand	0	5	181
Summit Station, Greenland	527	0	0
San José, Costa Rica	402	1	221
South Pole Station, Antarctica	2134	0	0

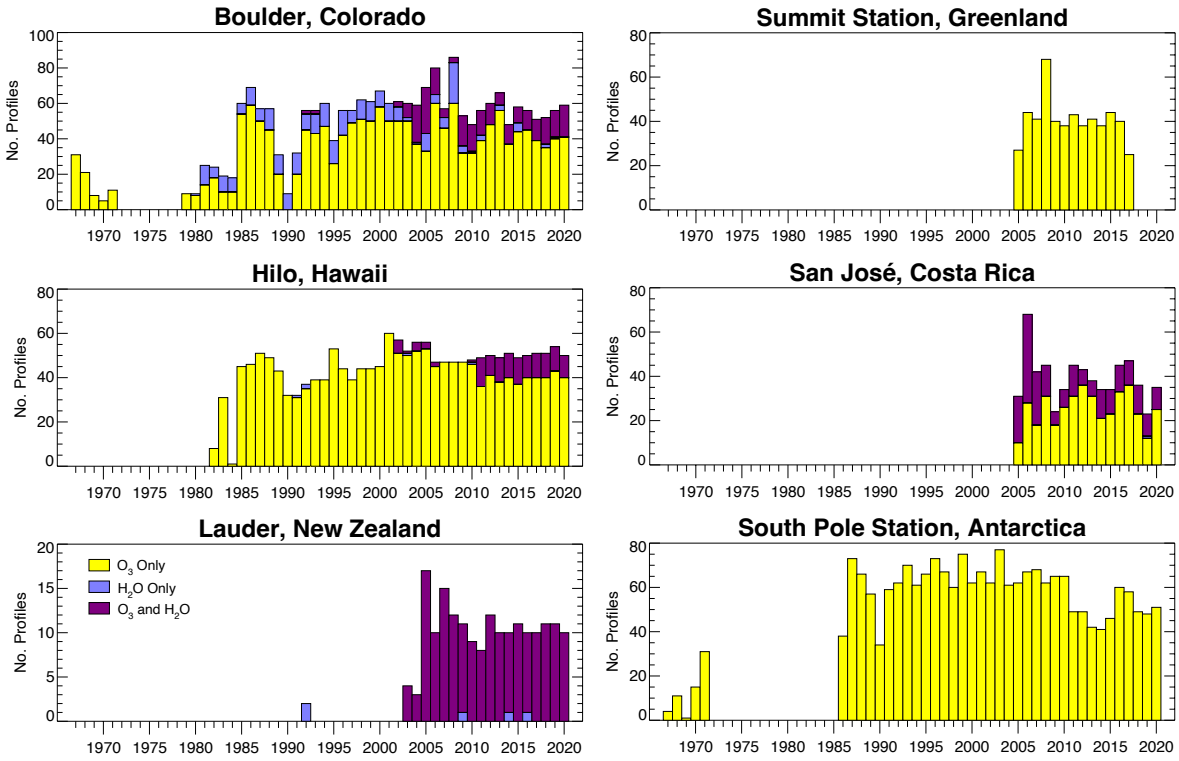

Figure 3.2: Stacked bar charts indicating the number of balloon profiles reaching at least 18 km above the surface, as a function of year for the 6 balloon sounding sites used. Yellow bars indicate the total number of ozonesonde-only observations, blue the total number of FPH/CFH-only observations, and purple the total number of balloon observations with both instruments. Note that the ordinate varies by observation site.

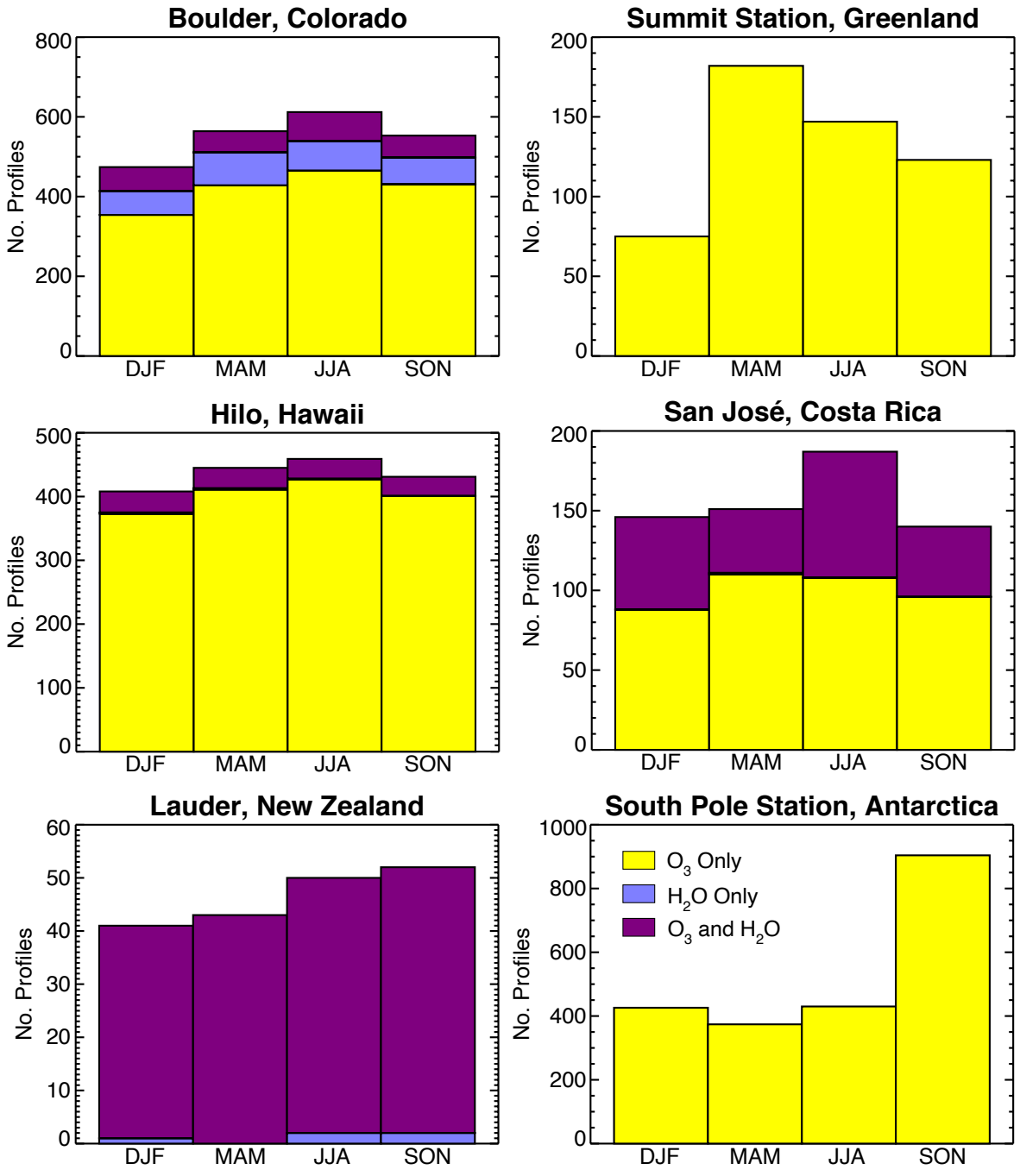

Figure 3.3: As in Fig. 3.2, but by season. Note that the disproportionate number of ECC soundings at South Pole Station during SON is due to an increased frequency of soundings each year during the formation and evolution of the polar ozone holes.

Figures 3.2 and 3.3 summarize data availability for all balloon sounding sites in detail as a function of year and season, respectively. The ozonesonde record is the most extensive of the balloon flights, extending back to the late 1960s for the Boulder and South Pole sites. The Boulder, Hilo, and South Pole stations have the longest data records, with sustained observations from the late-1970s or mid-1980s to the Present. Flights from Boulder (2003–Present), Hilo (2005–Present), San José (2005–Present), and Lauder (2011–Present) that include all three instruments (radiosonde, ECC, and FPH/CFH) amount to ∼10 seasonally-distributed flights per year for each site. The Boulder FPH record began in 1980, making it the world's longest record of UTLS H_2O measurements. There are varying degrees of seasonality in the availability of ozonesonde data for the balloon sounding sites, with the greatest seasonality at the South Pole and Summit Stations, where there are maxima in the number of observations during the seasons when substantial stratospheric O_3 depletion occurs (in September–November and March–May, respectively).

3.2.2 Reanalysis Output

To demonstrate global application of tropopause definitions in this study, output from the Modern-Era Retrospective analysis for Research and Applications, Version 2 (MERRA-2) is used. MERRA-2 is available every 3 hours from 1979 to the present at a horizontal grid spacing of $0.625° \times 0.5°$ longitude-latitude and 72 vertical levels, with a vertical grid spacing of ∼1100 m in the UTLS (Gelaro et al. 2017). Four individual 0000 UTC analysis times during the midpoint of each season of a single year are used here, to demonstrate the seasonality and variability of global tropopause definition and compare performance of the new stability-based tropopause definition introduced here to the lapse-rate and dynamic (i.e. PV-based) tropopauses. Tropopause altitudes are

calculated for each reanalysis profile after first interpolating temperature to a regular 100-m vertical grid using cubic splines.

3.3 Results

3.3.1 Composition-Stability Relationships

As outlined in Sect. 3.1, a unique opportunity afforded by modern balloon observations that include measurements of atmospheric composition is that the relationship between composition change in the tropopause transition layer and stability can be extensively evaluated. Here, I explore this using the entire record of balloon observations introduced in Sect. 3.2.1 and multiple metrics of static stability. In particular, analysis is focused on three easily computed conventional metrics that can be obtained from any balloon radiosonde profile or model output. Namely, I investigate vertical gradients of temperature ($\partial T/\partial z$), potential temperature θ ($\partial\theta/\partial z$), and the Brunt-Väisälä frequency N, given as:

$$N = \sqrt{\frac{g}{\theta}\frac{\partial\theta}{\partial z}} = \sqrt{\frac{g}{T}\left(\frac{\partial T}{\partial z} + \Gamma_d\right)} \tag{3.1}$$

where g is the gravitational constant (9.8 m s^{-2}) and Γ_d is the dry adiabatic lapse rate (9.8 K km^{-1}). Note that $\partial T/\partial z$ is simply the opposite sign of the environmental temperature lapse rate Γ, which the LRT definition is based upon. These three stability metrics have been widely used to both quantitatively and qualitatively depict stability change associated with the tropopause transition layer, but only $\partial T/\partial z$ (or Γ) has been routinely used for tropopause definition in the past.

Three example profiles of T, θ, O_3, and the stability metrics are given in Figure 3.4. The three profiles shown encompass variability in time of year, tropopause altitude,

and location, with a high-latitude example from the South Pole Station during austral spring with substantial stratospheric O_3 depletion, a midlatitude example from Boulder, Colorado, and a low-latitude example from San José, Costa Rica. Characteristic profiles of T and θ from each location indicate the variability in UTLS structure that make reliable, globally-applicable identification of the tropopause difficult. Namely, abrupt changes in T and θ and concomitant step-like changes in the stability metrics are found in the Boulder and San José examples, near altitudes of 14 km and 17 km, respectively. Sharp changes in O_3 composition clearly accompany the stability changes in those cases, which is common in environments with such strong stability-based tropopause definition. However, in the South Pole Station example, the tropopause transition in stability is more gradual, despite a pronounced O_3 composition change indicating a tropopause transition layer near 9 km altitude. The three stability metrics show a weak transition that is far less pronounced than in the other example profiles, but there is no pronounced minimum in the temperature profile near the tropopause.

Two main characteristics of stability profiles that aid in establishing a clear relationship between a stability metric and UTLS O_3 composition change are considered: i) increased troposphere-stratosphere contrast of the stability metric (i.e., the relative difference between common low-stability tropospheric and high-stability stratospheric values) co-located with the strong vertical gradient in O_3 and ii) decreased fluctuations of the stability metric that are generally unrelated with the tropopause transition layer. For the example profiles in Figure 3.4, $\partial\theta/\partial z$ appears to provide the greatest contrast of the stability metrics, but all metrics are characterized by large variability (especially at higher altitudes - i.e., throughout the stratosphere). This large variability stems from a range of thermodynamic and dynamic processes such as vertically propagating

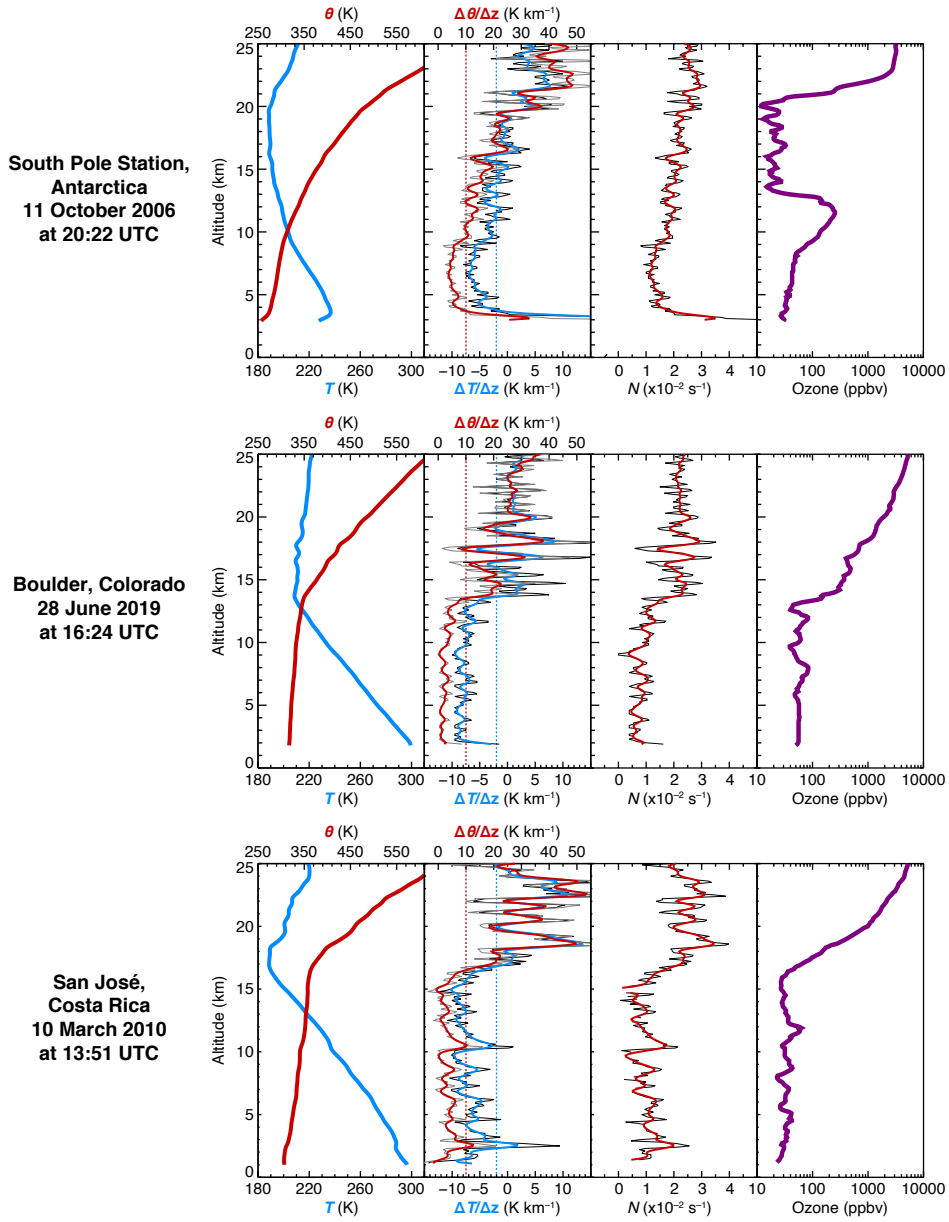

Figure 3.4: Example ozonesonde profiles of (from left to right) temperature (T; blue) and potential temperature (θ; red), vertical gradients of T ($\Delta T/\Delta z$) and θ ($\Delta\theta/\Delta z$), the Brunt-Väisälä frequency N, and ozone volume mixing ratio (purple). For the T, θ, and stability profiles, the raw data are shown by the black and gray profiles in the background, while colored lines show 2-σ Gaussian smoothing of the raw T and θ data. In the second panel, vertical blue and red dashed lines are given at constant values of $\Delta T/\Delta z = -2$ K km^{-1} and $\Delta\theta/\Delta z = 10$ K km^{-1}, respectively. The profiles are sourced from (top) South Pole Station, Antarctica on 11 October 2006 at 20:22 UTC, (middle) Boulder, Colorado on 28 June 2019 at 16:24 UTC, and (bottom) San José, Costa Rica on 10 March 2010 at 13:51 UTC.

high-frequency (e.g., gravity) waves and complex large-scale lamination of stable layers in latitude from Rossby wave breaking and tropopause folding (e.g., Holton et al. 1995; Stohl et al. 2003; Gettelman et al. 2011). To leverage stability transitions for tropopause definition, measuring changes over substantial depths or smoothing of the underlying T and θ data is sensible. Figure 3.4 shows the resulting reduction in variability of the stability metrics after application of 2-σ Gaussian smoothing to the 100-m T and θ profiles, which spans a layer $\sim$1 km deep in total and has a full width at half maximum of $\sim$500 m for the Gaussian weights. Nevertheless, some broad differences among the three stability metrics can be inferred from comparison in these three example profiles: i) $\partial\theta/\partial z$ provides the greatest troposphere-stratosphere contrast of the three metrics, and ii) of the smoothed metrics, N provides the least variance in magnitude with changing altitude unrelated with the transition layer. These differences and their relationship to troposphere-stratosphere O_3 composition change are robustly examined in the statistical analysis that follows.

Figure 3.5 shows two-dimensional frequency distributions of joint O_3 and stability observations for all balloon observations from each site. This analysis is limited to altitudes between 5 and 20 km (5 and 25 km for San José) to focus on observations from the UTLS and prevent contamination from stable planetary boundary layer inversions. Most joint frequency distributions reveal a bimodal pattern, with frequent observations of low O_3 ($\lessapprox$100 ppbv) at low stability and frequent observations of high O_3 ($\gtrapprox$100 ppbv) at high stability. The degree of bimodality and 2-D separation of the low and high modes varies by location and stability metric. For low latitude, high tropopause altitude stations (Hilo and San José), there is weaker bimodality and an overall frequency bias toward the low mode due to more of the analyzed layer being in the troposphere. The bimodality increases with latitude for the remaining stations,

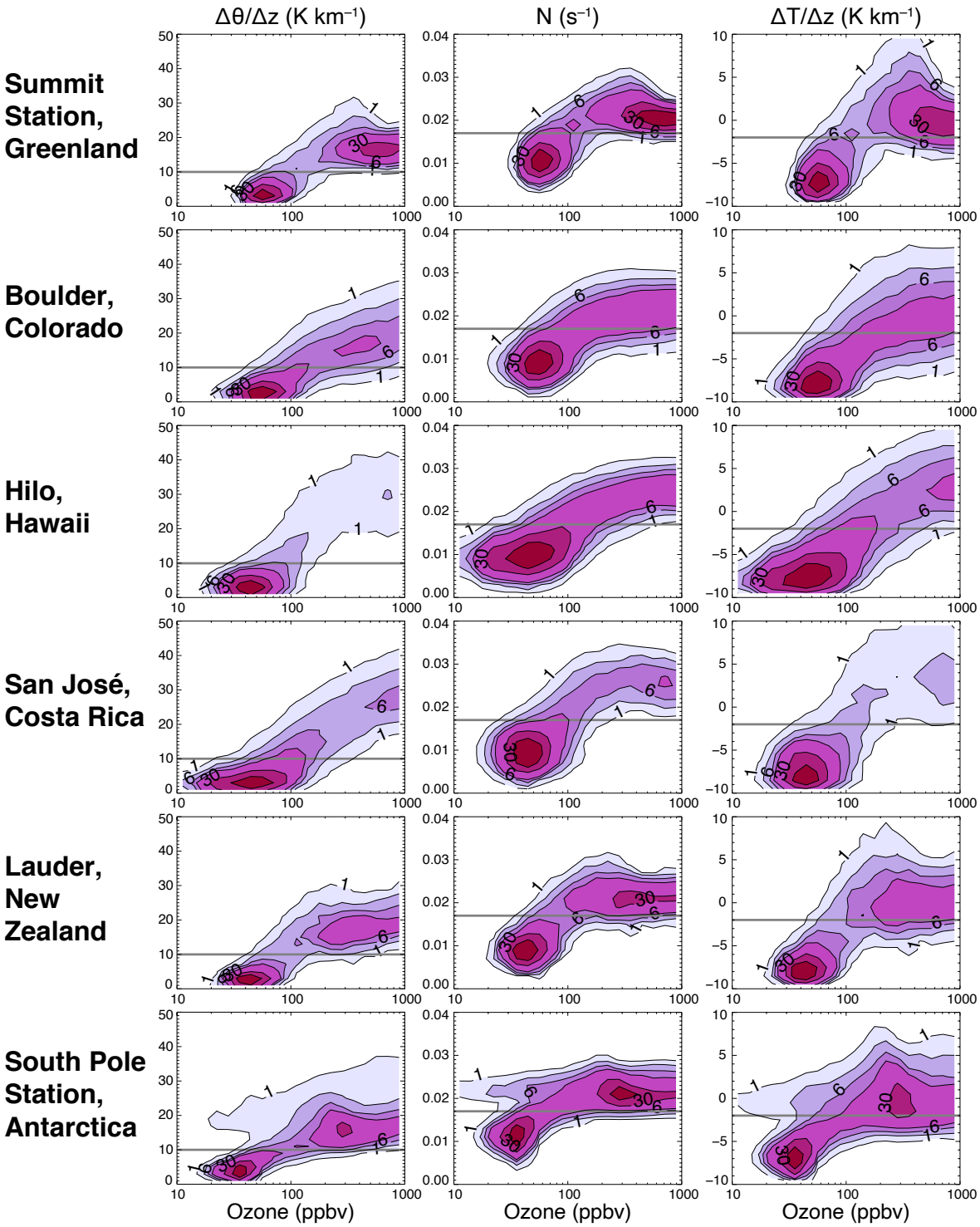
Δθ/Δz (K km⁻¹)
N (s⁻¹)
ΔT/Δz (K km⁻¹)
Summit Station, Greenland
Boulder, Colorado
Hilo, Hawaii
San José, Costa Rica
Lauder, New Zealand
South Pole Station, Antarctica
Ozone (ppbv)
Ozone (ppbv)
Ozone (ppbv)

Figure 3.5: Two-dimensional frequency distributions of ozone vs. (left) potential temperature gradient $\Delta\theta/\Delta z$, (middle) Brunt-Väisälä frequency N, and (right) temperature gradient $\Delta T/\Delta z$ for all measurements from each observation site. Ozone is placed into logarithmic bins of size 0.1, while $\Delta\theta/\Delta z$, $\Delta T/\Delta z$, and N are placed into bins of size 2 K km^{-1}, 1 K km^{-1}, and 0.002 s^{-1}, respectively. Contours represent the frequency of observations relative to the maximum value within any 2-D bin in each panel, with shading at 1, 3, 6, 10, 30, and 60%. Gray horizontal lines are given in each panel at constant values of $\Delta\theta/\Delta z = 10$ K km^{-1}, $N = 0.017$ s^{-1}, and $\Delta T/\Delta z = -2$ K km^{-1}, for reference.

reflecting a more equal population of tropospheric and stratospheric air in the contributing observations as a result of the transition to both lower tropopause altitude, and downward transport of high-O_3 air in the midlatitude lower stratosphere, which enhances the near-tropopause gradient in composition and thereby increases O_3 separation of the modes.

Each of the stability parameters offer strong separation in stability magnitudes for the two high-frequency modes, which is indicated by lesser overlap of high- and low-O_3 modes in stability space (Fig. 3.5), though identification of a tropopause transition layer via stability is challenging for any metric since composition and stability are not always positively related (e.g., at some point there is no relation for air confined to the troposphere or stratosphere and away from the tropopause). However, the stability parameters differ in the consistency of the value at which this separation occurs in different environments. In Figure 3.5, somewhat arbitrary gray horizontal lines are drawn for each stability metric at a constant value across all stations: -2 K km^{-1} for $\Delta T/\Delta z$ (i.e., the value consistent with the LRT), 10 K km^{-1} for $\Delta\theta/\Delta z$, and 0.017 s^{-1} for N. The -2 K km^{-1} $\Delta T/\Delta z$ threshold corresponds relatively well with the location of high-frequency mode separation for Summit Station, Hilo, San José, and Lauder, but overlaps with air with stratospheric O_3 characteristics for Boulder and South Pole Station. Alternatively, both the $\Delta\theta/\Delta z$ and N thresholds perform relatively well at

all locations. A constant $\Delta\theta/\Delta z$ threshold, specifically, seems the most appropriate metric for identification of the transition at all stations due to minimized overlap of the high-frequency modes. The consistency of a single $\Delta\theta/\Delta z$ value (10 K km^{-1} in this case) co-located with the UTLS composition transition in a variety of tropopause environments indicates that this metric provides the most promising opportunity for discriminating between troposphere and stratosphere layers on a global scale. The analysis in Figure 3.4 is consistent with this conclusion, where a 10 K km^{-1} $\partial\theta/\partial z$ threshold is reached at the location of the strong O_3 gradient at each station.

Why is it that the three stability metrics vary in the consistency of their relationship to composition change across a variety of environments? To investigate this, relationships between $\partial\theta/\partial z$ and the remaining stability metrics as a function of altitude are shown in Figure 3.6. The relationship between $\partial\theta/\partial z$ and $\partial T/\partial z$ is modified by pressure: a -2 K km^{-1} $\partial T/\partial z$ threshold corresponds with smaller $\partial\theta/\partial z$ values at higher pressures (lower altitudes; e.g., $\sim$10 K km^{-1} at 300 hPa) and larger values at lower pressures (higher altitudes; e.g., $\sim$14 K km^{-1} at 100 hPa). Similarly, the relationship between $\partial\theta/\partial z$ and N is modified by θ, where lower θ corresponds to lower altitudes and vice versa. This vertical variation of the relationship between stability metrics demonstrates why tropopause identification based on them can differ. Ultimately, the composition-stability analysis shown in Figure 3.5 indicates that $\partial\theta/\partial z$ is the most consistent at demarcating the UTLS composition change using a single threshold value. Motivated by the above results, I introduce a new $\partial\theta/\partial z$-based tropopause definition in the following subsection.

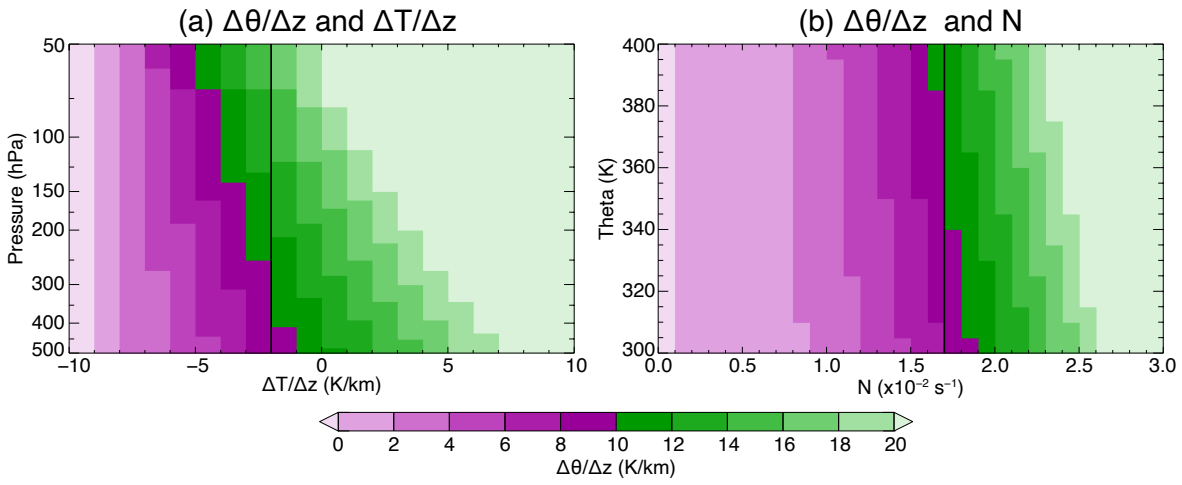

Figure 3.6: Values of $\Delta\theta/\Delta z$ as a function of (a) $\Delta T/\Delta z$ and pressure, and (b) N and θ. Black vertical lines are given at constant values of (a) $\Delta T/\Delta z = -2$ K and (b) $N = 0.017$ s^{-1}.

3.3.2 The Potential Temperature Gradient Tropopause Algorithm

Based on the finding from statistical analysis of balloon observations that the vertical gradient of potential temperature ($\partial\theta/\partial z$) provides the greatest discrimination between air masses with tropospheric or stratospheric characteristics, an algorithm to identify a potential temperature gradient tropopause (hereafter PTGT) was sought. The goals of this new algorithm were to: 1) provide a reliable technique for tropopause altitude identification that captured the typical step-wise change in the magnitude of $\partial\theta/\partial z$ (and more generally, static stability) from troposphere to stratosphere, 2) to improve stability-based identification of the tropopause in instances where the conventional LRT definition fails, and 3) to better coincide with the sharp composition change commonly observed in the tropopause transition layer. After rigorous tests and evaluation of mathematical approaches to this problem, the most reliable and simplest approach developed is modeled after the LRT definition.

The PTGT definition is as follows: i) the first tropopause is defined as the lowest level at which the potential temperature gradient increases to 10 K km^{-1}, provided also that the potential temperature gradient between this level and all higher levels within 2 km does not fall below 10 K km^{-1}, and ii) if above the first tropopause, the potential temperature gradient between any level and all higher levels within 1 km falls below 10 K km^{-1}, then a second tropopause may be defined as done for the first tropopause, but using a potential temperature gradient threshold of 15 K km^{-1}. The 10 and 15 K km^{-1} thresholds were selected based on sensitivity tests, with the ultimate goal being consistent performance at all latitudes. These $\partial\theta/\partial z$ thresholds also commonly coincide with composition change observed near the tropopause and in complex transport events such as Rossby wave breaking (e.g., Pan et al. 2009).

Applying this definition reliably and as intended by the authors requires that data are on a regular altitude grid and that forward (i.e., upward) finite differencing is used for computing the potential temperature gradient, as implied by the language in the definition (again, consistent with the LRT). While most tropopause definitions do not outline the utility and/or necessity of requiring all profile data to conform to a uniform vertical grid, doing so is advantageous to reliable and consistent application of any tropopause definition since nearly all algorithms attempt to identify robust changes in some variable —typically temperature— over a finite depth. To formalize this, I emphasize here that a necessary step to successful implementation of any tropopause algorithm be interpolation of profile data to a uniform grid (100-m data spacing is recommended for most datasets). Note that for temperature, interpolation via cubic splines is often preferred to minimize error in tropopause identification (e.g., Hoffmann and Spang 2022).

3.3.3 Evaluation of the Tropopause Algorithm

3.3.3.1 Application to Observations

Figure 3.7 shows the results of applying LRT and PTGT tropopause definitions to the example profiles previously shown in Figure 3.4. These examples demonstrate near perfect agreement of the two tropopause definitions in the Boulder and San José profiles where the stability transition is sharp and large disagreement in the South Pole Station example where the transition is weaker. Namely, in the South Pole Station profile, the PTGT definition identifies the subtle, lower altitude transition in stability that lies in close proximity to the pronounced O_3 increase near 9 km, indicative of the transition from troposphere to stratosphere air. Alternatively, the LRT definition is biased nearly 5 km high, identifying an arbitrary level that satisfies the lapse-rate criteria and falls within the broad layer of stratospheric O_3 depletion found ∼12–22 km in this example. As outlined in Sect. 3.1, such high bias in LRT altitude in the polar regions was one motivating factor for revisiting stability-based tropopause definition in this study due to its unfortunately common occurrence during winter and early spring, which will ultimately introduce significant error to any analysis that relies on accurate identification of the tropopause (e.g., stratosphere–troposphere exchange). As will be shown further below, the improvement in tropopause identification given by the new PTGT definition is not unique to this example.

Figure 3.8 shows scatterplots comparing PTGT and LRT altitudes for all of the balloon observations. The scatterplots are densely grouped along a 1-to-1 line at all locations, indicating frequent agreement between the two definitions. When the PTGT and LRT disagree, the PTGT is almost always identified at a lower altitude. Lauder and Summit Station show the best agreement among the six stations, with only 4.8% and 1.7% of profiles containing differences larger than 1 km, respectively. For the

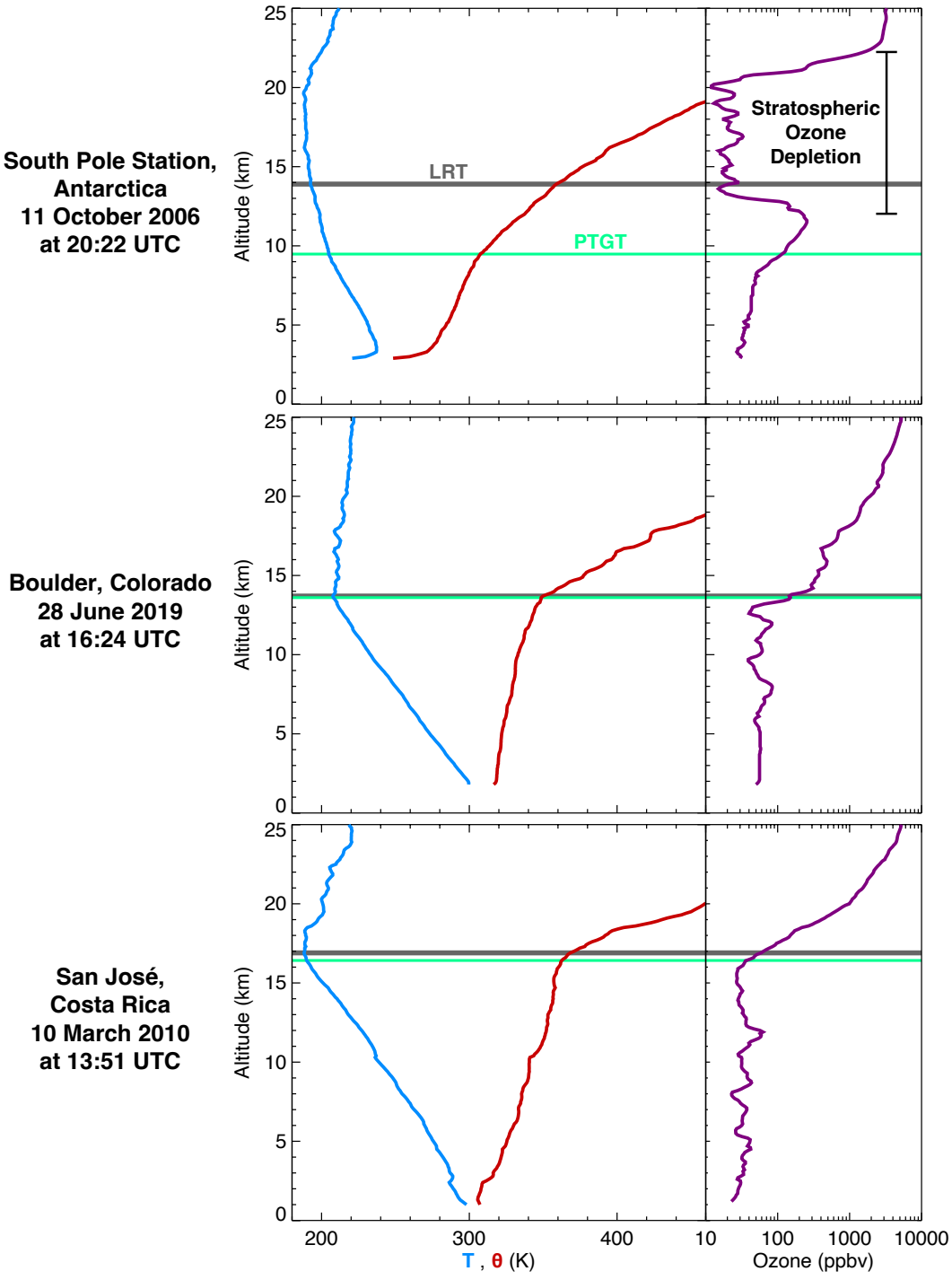

Figure 3.7: For the same profiles in Fig. 3.4: (left) profiles of temperature (T; blue) and potential temperature (θ; red) and (right) profiles of ozone volume mixing ratio. Altitudes of objectively diagnosed lapse-rate tropopauses (LRT; gray) and potential temperature gradient tropopauses (PTGT; green) are superimposed.

remaining balloon sounding sites (Boulder, Hilo, San José, and South Pole Station), there are substantial occurrences of PTGT < LRT. In total, differences between PTGT and LRT larger than 1 km are found for 21.8% of the soundings at Boulder, 38.6% of the soundings at Hilo, 29.0% at San José, and 26.5% at South Pole Station. The frequency of large differences at South Pole Station is likely biased high since 40% of the observations are made in SON when the LRT is frequently biased high (Fig. 3.3). To evaluate the consequences of this difference in tropopause definition, attention is focused on the observed composition change relative to the diagnosed LRT and PTGT heights in the analysis that follows.

From a composition perspective, O_3 concentrations relative to an appropriately identified tropopause will be uniformly low in the troposphere in most cases, with a sharp increase in O_3 within the tropopause transition layer and increasingly high values with increasing altitude in the lower stratosphere. Such analysis is featured in Figure 3.9, which shows tropopause-relative profiles of O_3, θ, and temperature for each station. The vertical structure and median O_3, θ, and temperature change across the LRT and PTGT are nearly indistinguishable for Lauder and Summit Station. The low spread between 10^{th} and 90^{th} percentile values also suggests consistent tropopause identifications for both definitions relative to O_3 concentrations at these locations, although this is also likely a reflection of their limited sampling (Figs. 3.3 and 3.8). Alternatively, tropopause-relative O_3 concentrations for Boulder, Hilo, San José, and South Pole Station exhibit notable differences for the PTGT and LRT definitions.

For Boulder, while PTGT-relative concentrations of O_3 remain low ($\leq$ 90 ppbv) throughout the troposphere (i.e., below-tropopause altitudes), O_3 concentrations begin to increase $\sim$ 2 km below the LRT. This leads to a slightly weaker O_3 gradient across the tropopause, and higher LRT-relative concentrations throughout the stratosphere

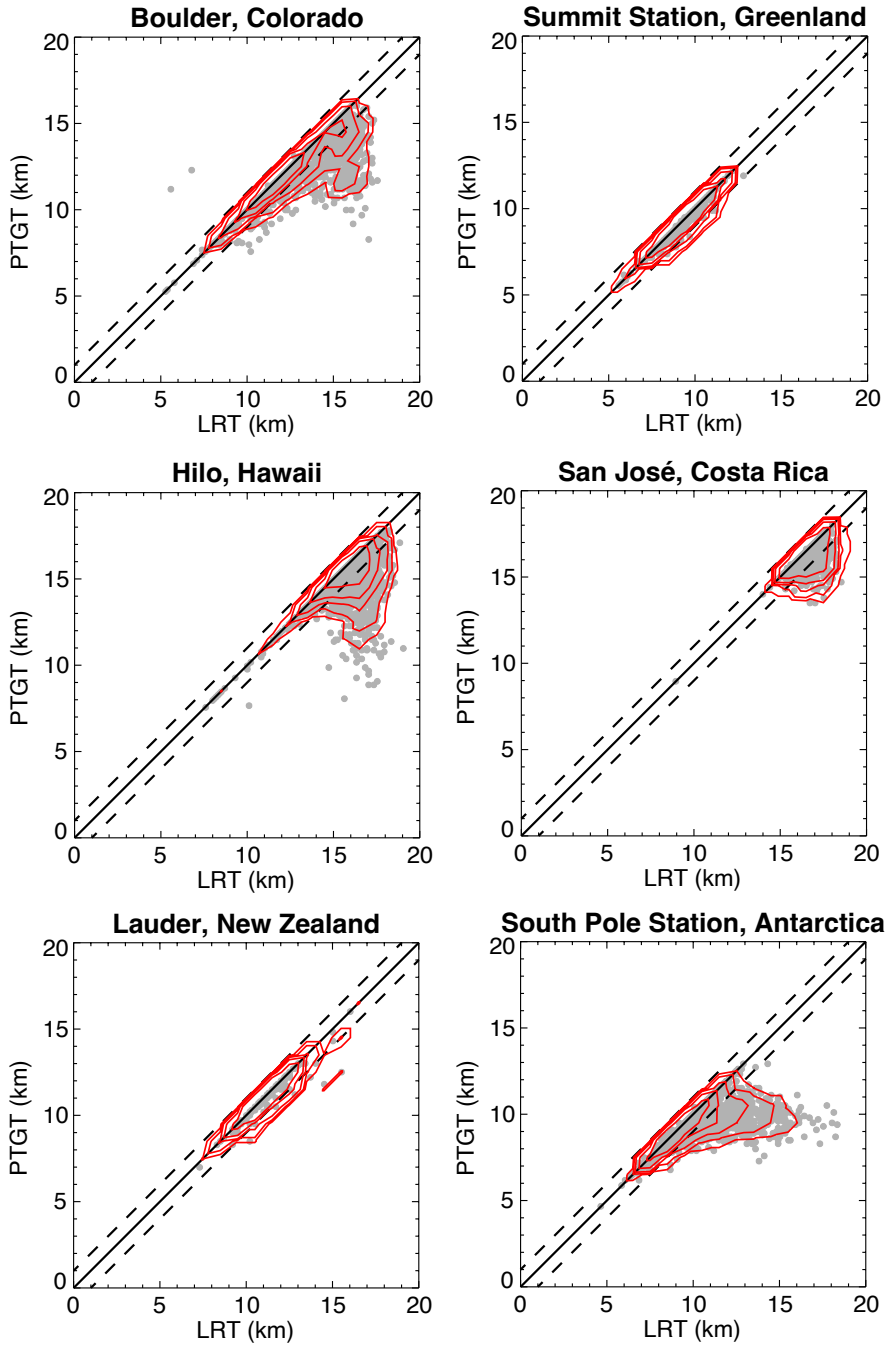

Figure 3.8: Scatterplots comparing PTGT and LRT altitudes for all balloon observations used in this study, separated by observation site. The solid black lines are 1-to-1 lines and the dashed black lines show the boundaries of ± 1 km altitude differences. Red contours indicate the density of observations in 1-km × 1-km bins as the fraction of the total number of profiles, doubling in magnitude from 0.5 to 8 % (i.e., 0.5, 1, 2, 4, and 8 %).

relative to PTGT-relative concentrations. These differences reveal that the LRT definition is more frequently identifying the tropopause near the top of the transition layer, while the PTGT is identifying the tropopause near the base of the transition layer. A similar pattern is seen in the Hilo and San José tropopause-relative profiles, where LRT-relative O_3 concentrations begin to exceed those based on the PTGT 3–4 km below the tropopause. The Hilo profiles also stand out due to the wider 10^{th} to 90^{th} percentile spread of PTGT-relative O_3, θ, and temperature, likely reflecting increased complexity of UTLS layers common to the subtropics. For the Hilo and San José profiles, the low PTGT-relative 10^{th} percentile stratospheric O_3 concentrations and θ, combined with the high 90^{th} percentile PTGT-relative temperatures, are indicative of profiles where the PTGT is identified well below the LRT (as indicated in Fig. 3.8). Lastly, the South Pole Station exhibits the largest differences between PTGT- and LRT-relative observations of any of the balloon sounding sites. The median concentrations for all profiles (Fig. 3.9) differ slightly, but the 90^{th} percentile below-tropopause concentrations of LRT-relative O_3 are an order of magnitude larger than the respective PTGT-relative observations. This is the result of a number of profiles where the lapse-rate criteria are not satisfied near the strong tropopause-level O_3 gradient, resulting in an LRT altitude that is biased several kilometers high (as in the South Pole Station example in Fig. 3.7).

Figure 3.10 displays tropopause-relative observations for only those profiles where the PTGT is identified more than 1 km below the LRT for the 4 balloon sounding sites where there is adequate sampling of such environments. For Hilo and Boulder, 38.6% and 21.8% of profiles contain a PTGT altitude more than 1 km below the LRT and substantial differences between all three PTGT- and LRT- relative parameters are

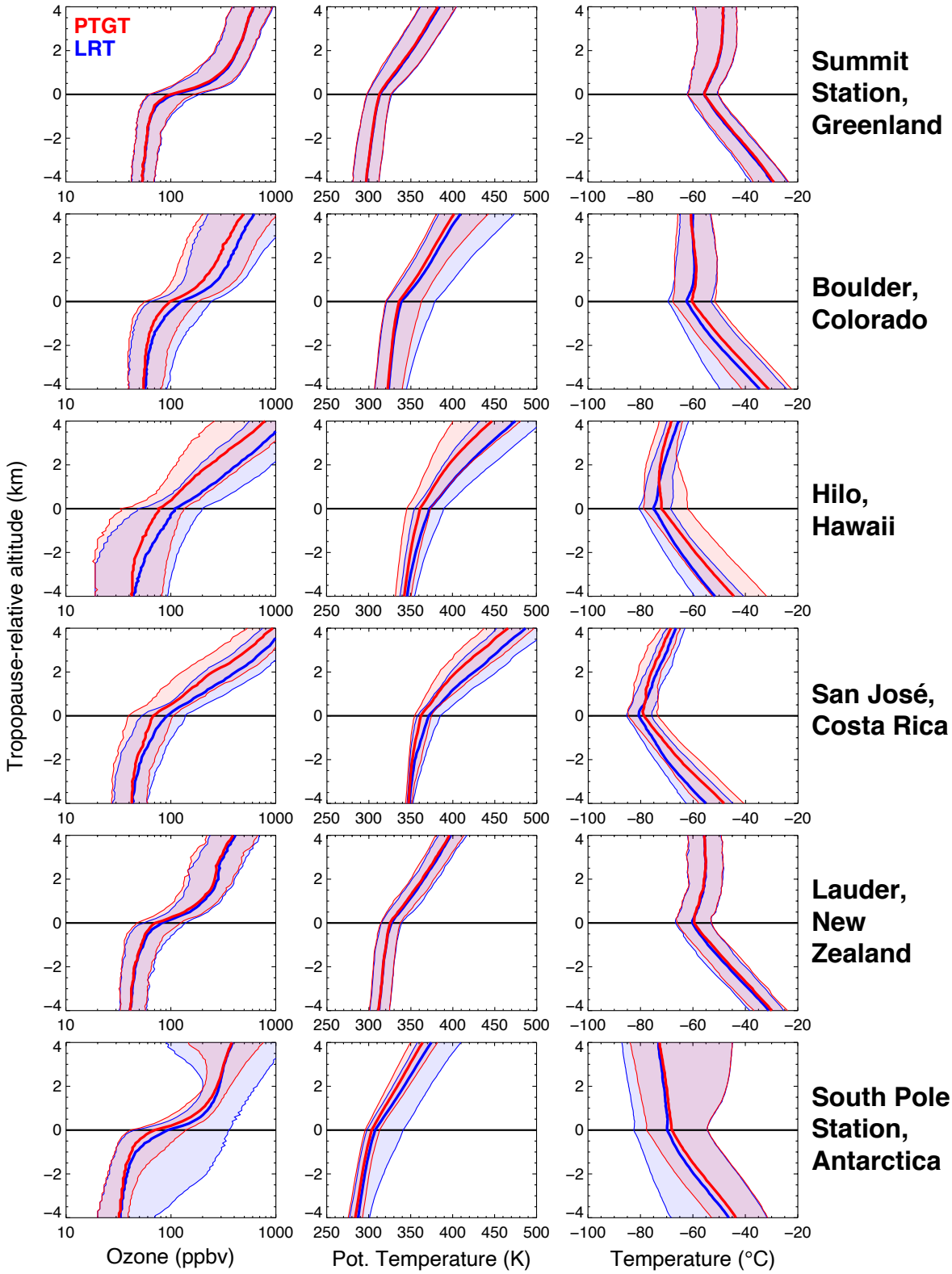
PTGT
LRT
Summit Station, Greenland
Boulder, Colorado
Hilo, Hawaii
San José, Costa Rica
Lauder, New Zealand
South Pole Station, Antarctica
Tropopause-relative altitude (km)
Ozone (ppbv)
Pot. Temperature (K)
Temperature (°C)

Figure 3.9: For all profiles with ozone from each observation site: tropopause-relative profiles of (left) ozone, (middle) potential temperature, and (right) temperature. Thin lines bounding the color-fill in each panel span the 10th- to 90th-percentile observations for each variable, while thick lines superimposed on the color-fill represent the median value. Blue profiles are relative to the LRT, while red profiles are relative to the PTGT.

revealed in Figure 3.10. As in the results for all profiles in Figure 3.9, O_3 concentrations remain low throughout the PTGT-relative troposphere, with a modest gradient occurring across the tropopause. Alternatively, the LRT-relative O_3 profiles for Hilo and Boulder feature increases throughout the upper troposphere and a stronger gradient across the tropopause than that for PTGT concentrations. The accompanying temperature and potential temperature profiles provide insight into why these differences may be occurring. Specifically, the LRT-relative temperatures exhibit a strong, cold-point minimum at the level of the diagnosed tropopause that is characteristic of tropical environments, while the PTGT-relative temperatures are similar in structure to a double tropopause environment, where a weak transition in stability accompanies the primary tropopause and the colder, higher tropical tropopause remains as the secondary tropopause (and often temperature minimum of the profile). This suggests that Hilo and Boulder profiles where the LRT is located well above the PTGT occur due to the PTGT identifying a lower, weaker stability transition that does not satisfy the criteria of the LRT definition but from a composition perspective (O_3) is consistent with horizontal layering of tropical troposphere and extratropical stratosphere that is a robust outcome from the formation of a large-scale double tropopause (e.g., Pan et al. 2009).

The results for profiles with PTGT altitude more than 1 km below the LRT at San José are similar to those at Hilo and Boulder. While this outcome is somewhat surprising as transport of extratropical lower stratosphere air does not often extend

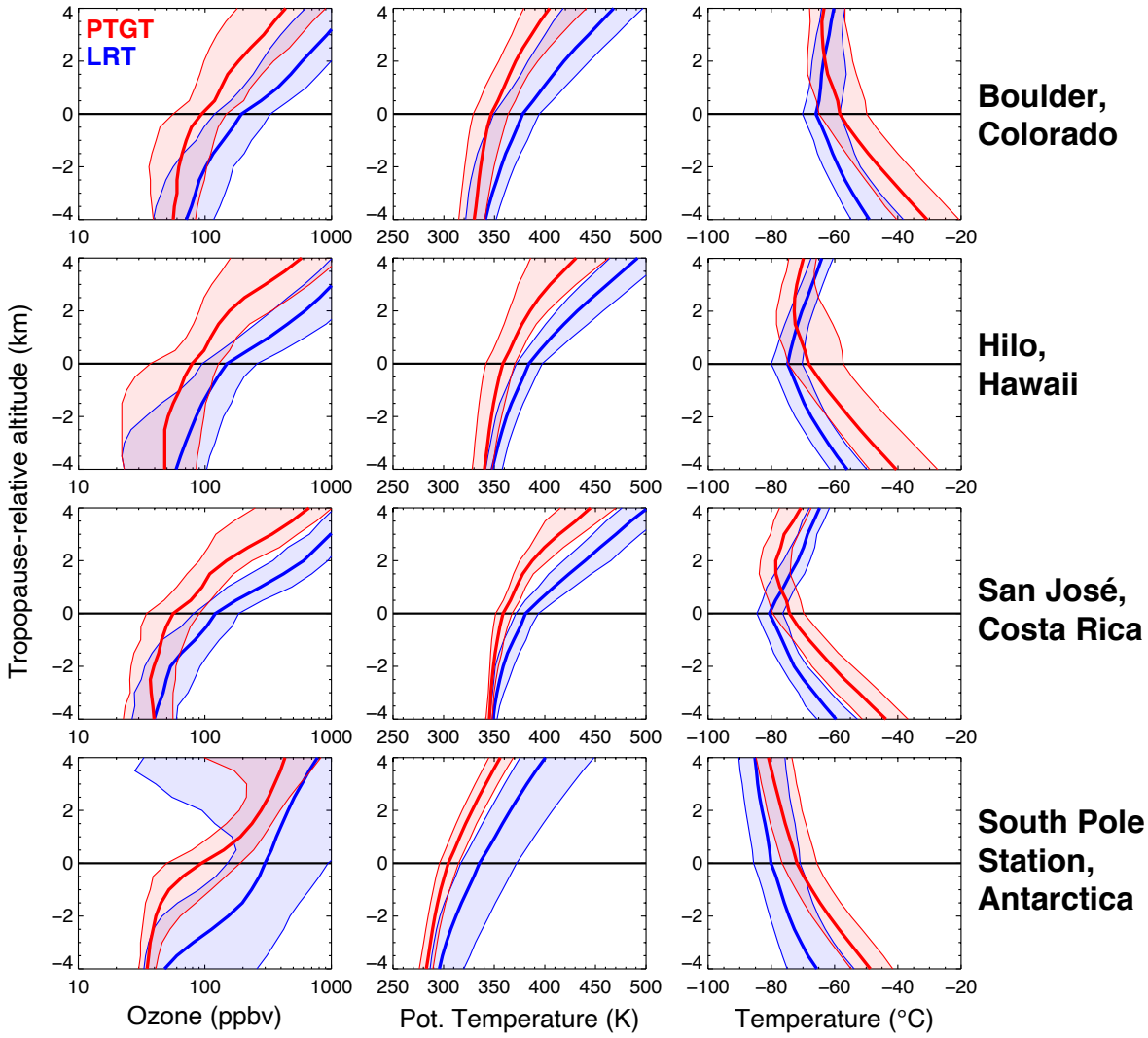

Figure 3.10: As in Fig. 3.9, but only for instances where the PTGT is located more than 1 km below the LRT.

deeply into the tropics, the tropopause-relative O_3 indicates that the PTGT location better captures the tropopause-level composition change at this station. Finally, for the 26.5% of South Pole Station profiles where the PTGT is located more than 1 km below the LRT, the differences in O_3 concentrations are remarkable. As discussed previously, the LRT often fails to capture the weak stability transition that occurs at the poles and is biased several kilometers high. The analysis shown in Figure 3.10 demonstrates that the PTGT excels at identifying the tropopause transition in these cases, as demonstrated by its approximate co-location with the sharp O_3 increase at the tropopause.

The appropriateness of each tropopause definition from a composition perspective is further examined by analyzing their locations in O_3–H_2O tracer–tracer space. This is accomplished using profiles from the four balloon sounding sites where coincident O_3 and H_2O observations are available: Boulder, Hilo, San José, and Lauder. Figure 3.11 shows joint frequency distributions of O_3 and H_2O observations with the frequency of PTGT and LRT definitions in O_3–H_2O space superimposed, where observations from all four sites are combined and separated into high tropopause environments (where both PTGT and LRT exceed 14 km), low tropopause environments (where both PTGT and LRT are below 14 km), and environments where the LRT is identified above 14 km while the PTGT is identified below 14 km (i.e., where they differ substantially).

The O_3–H_2O joint frequency distributions in Figure 3.11 reveal features commonly identified in prior work (Pan et al. 2004; Hegglin et al. 2009; Tilmes et al. 2010). Namely, tropical, high-tropopause altitude environments are characterized by two distinct stratospheric and tropospheric branches in tracer–tracer space, which meet near the tropopause at low concentrations of both trace gases and form an "L"-shaped relationship (as found in Fig. 3.11a). Here, the stratospheric branch has uniformly low

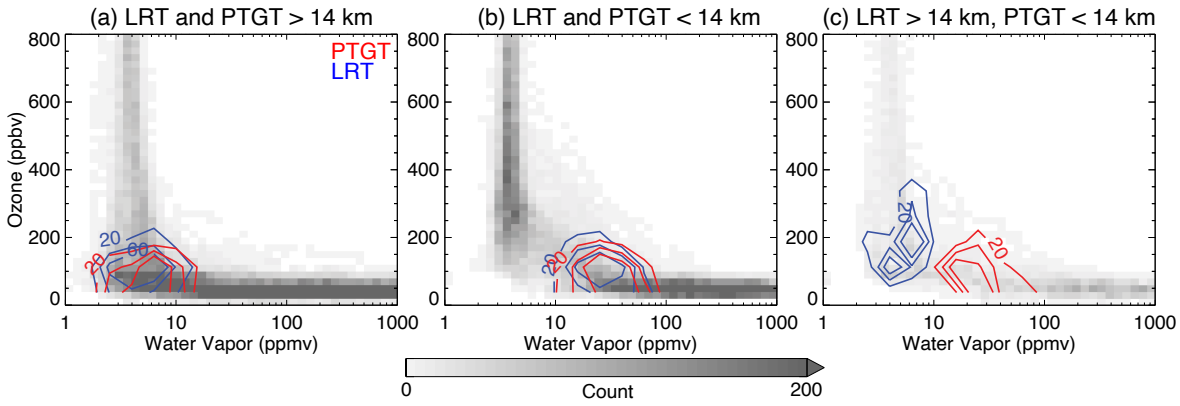

Figure 3.11: Locations of identified PTGTs and LRTs in tracer–tracer space for co-located observations of ozone and water vapor from the Boulder, Hilo, San José, and Lauder stations for (a) high-tropopause (tropical) environments, (b) low-tropopause (extratropical) environments, and (c) environments where a tropical and extratropical tropopause are identified by the LRT and PTGT definitions, respectively. Gray shading indicates the number of 250-m layer observations placed into each water vapor-ozone (0.1 log(ppmv) x 75 ppbv sized) bin, and red and blue contours represent the frequency of PTGT and LRT definitions in tracer–tracer space (in %), respectively. The number of profiles contributing to each panel are: (a) 358, (b) 332, and (c) 59.

H_2O (<10 ppmv) and a wide range of O_3 concentrations, and the tropospheric branch has uniformly low O_3 (<150 ppbv) and a wide range of H_2O concentrations. In the subtropics and extratropics, a three-branch structure emerges, with the third branch characterized by a negative slope that broadens the corner of the "L" shape and intersects the tropospheric and stratospheric branches (commonly referred to as the extratropical transition layer or ExTL, or more generally as the "mixing" branch). The degree of mixing between stratospheric and/or tropospheric air in the UTLS helps to control the extent to which this branch extends toward higher concentrations of the stratospheric and tropospheric tracers (e.g., Pan et al. 2004; Konopka and Pan 2012). For the tropical, high-tropopause environment profiles and extratropical, low-tropopause profiles analyzed here (Figs. 3.11a and 3.11b), there is clear agreement between the LRT and PTGT definitions in tracer–tracer space, with the PTGT favoring slightly lower O_3.

For high-tropopause environments, the tropopause altitudes are consistently identified at the corner of the "L" shape. For low-tropopause environments, the tropopause altitudes from both definitions are consistently identified at the tropospheric end of the ExTL. For the profiles where the PTGT and LRT definitions substantially differ (Fig. 3.11c), the tracer–tracer distributions appear to be more subtropical in nature with a shallower mixing branch and the PTGT altitudes favor the tropospheric end of the mixing branch (as in low-tropopause, extratropical environments) while the LRT altitudes favor the stratospheric end of the mixing branch. This result demonstrates that the PTGT definition results in more consistent stability-based identification of UTLS composition change than the LRT definition.

3.3.3.2 Observations of Multiple Tropopauses

Environments with multiple stable layers in the UTLS, and therefore multiple tropopauses, are not uncommon and have been observed since early radiosondes (e.g., Kochanski 1955). Such environments are of particular interest due to their connection with both large and smaller (i.e. convective) scale stratosphere–troposphere exchange (e.g., Schwartz et al. 2015; Pan et al. 2009; Homeyer et al. 2011, 2014; Solomon et al. 2016; Tinney and Homeyer 2021). Accordingly, double tropopause (DT) environments have been investigated in both observations and model output in recent decades. They occur in both hemispheres and most frequently occur in the midlatitudes during the cool season, often near the subtropical jet (e.g., Randel et al. 2007a; Añel et al. 2008; Schwartz et al. 2015; Manney et al. 2017; Xian and Homeyer 2019). Most frequently, a DT is formed by differential advection of less stable, tropical upper tropospheric and more stable, extratropical lower stratospheric air, often associated with a Rossby wave breaking event (e.g., Randel et al. 2007a; Pan et al. 2009; Castanheira and Gimeno 2011; Peevey et al. 2012; Schwartz et al. 2015; Liu and Barnes 2018). DTs can also

form through modification of thermodynamic properties from dynamic stretching or shrinking of layers in the UTLS (e.g., Randel et al. 2007a; Wang and Polvani 2011; Peevey et al. 2014). Additionally, Castanheira et al. (2009) and Xian and Homeyer (2019) have shown an increase in the frequency of DT events since the mid-to-late 20$^{\text{th}}$ century, for which the processes responsible are not well understood.

Table 3.2: The frequency of double tropopause identifications in the observed profiles. For each site, the double tropopause frequency based on the LRT definition, PTGT definition, and both definitions is given.

Observation Site	**LRT (%)**	**PTGT (%)**	**Both (%)**
Summit Station, Greenland	23.7	2.8	2.5
Boulder, Colorado	61.5	39.9	34.1
Hilo, Hawaii	22.2	20.1	8.1
San José, Costa Rica	12.4	11.9	3.9
Lauder, New Zealand	41.1	15.1	13.5
South Pole Station, Antarctica	22.0	6.4	2.7

With the exception of the proposed PTGT definition, the LRT is the only tropopause definition that provides additional language for DT identification: "*If above the first tropopause the average lapse rate between any level and all higher levels within 1 km exceeds 3° C km^{-1}, then a second tropopause is defined by the same criterion as [the primary definition]. This tropopause may be either within or above the 1 km layer*" (World Meteorological Organization 1957). As described in the algorithm description in Sect. 3.3.2, the PTGT provides a similar definition based on $\partial\theta/\partial z$ thresholds. A comparison of LRT- and PTGT-defined DTs is therefore desired, which is included here. The frequency of DT identifications at each station based on the LRT and PTGT definitions are summarized in Table 3.2. At all stations, the PTGT identifies fewer DTs than the

LRT, though the magnitude of this difference varies by station. This is likely the result of the variation in the $\partial\theta/\partial z$– $\partial T/\partial z$ relationship with altitude: the LRT and PTGT thresholds are well aligned at lower latitudes where DTs occur at lower pressures, while at higher latitudes it is more difficult for the PTGT DT requirement of 15 K km^{-1} to be met at higher pressures (Fig. 3.6). The latitudinal variation in DT identifications is similar between the two definitions, with both identifying DTs most frequently at midlatitude stations (Boulder and Lauder). However, the LRT identifies far more DTs in the polar stations (Summit and South Pole) where the PTGT identifies relatively few. To further explore these differences, example profiles are shown in Figure 3.12 and frequency distributions of tropopause altitude differences are shown in Figure 3.13.

In cases where both definitions identify a DT (Figs. 3.12e,f and right column of Fig. 3.13), the identifications of both the primary and secondary tropopause levels are within 500 m of each other more than 60% of the time at all stations except for the South Pole. Additionally, they are consistent more than 80% of the time at Boulder, the station where such profiles are most common. When a DT is identified by the LRT definition only (Figs. 3.12a,b and left column of Fig. 3.13), the PTGT and LRT primary tropopause are often found within 500 m of each other, while the LRT identifies a secondary boundary anywhere from ∼3–7 km above, depending on the station. As mentioned above, at least part of this population of DTs identified by the LRT only is likely a result of the vertical variation in the $\partial\theta/\partial z$– $\partial T/\partial z$ relationship making the PTGT DT requirement more difficult to attain, especially at higher latitudes. Alternatively, in cases where a DT is identified by the PTGT definition only, the PTGT secondary tropopause often aligns with the LRT primary tropopause (Figs. 3.12c,d and middle column of Fig. 3.13). However, the primary PTGT in such cases is most frequently found ∼2-4 km below the primary LRT, where it is identifying a

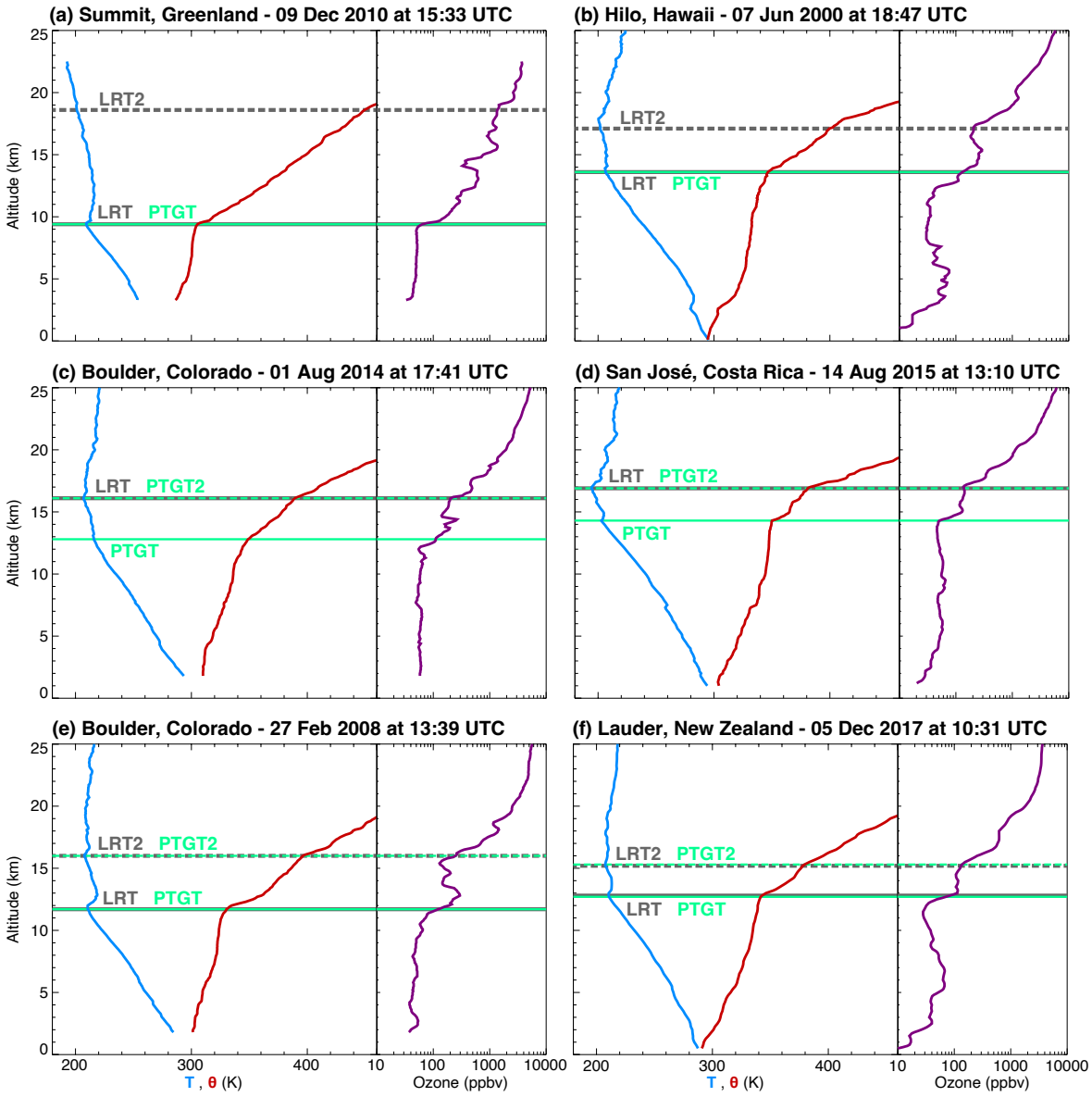

Figure 3.12: As in Fig. 3.7, but for select profiles with a double tropopause identification: (a,b) LRT-only, (c,d) PTGT-only, and (e,f) LRT and PTGT. Secondary tropopauses are given by the dashed horizontal lines.

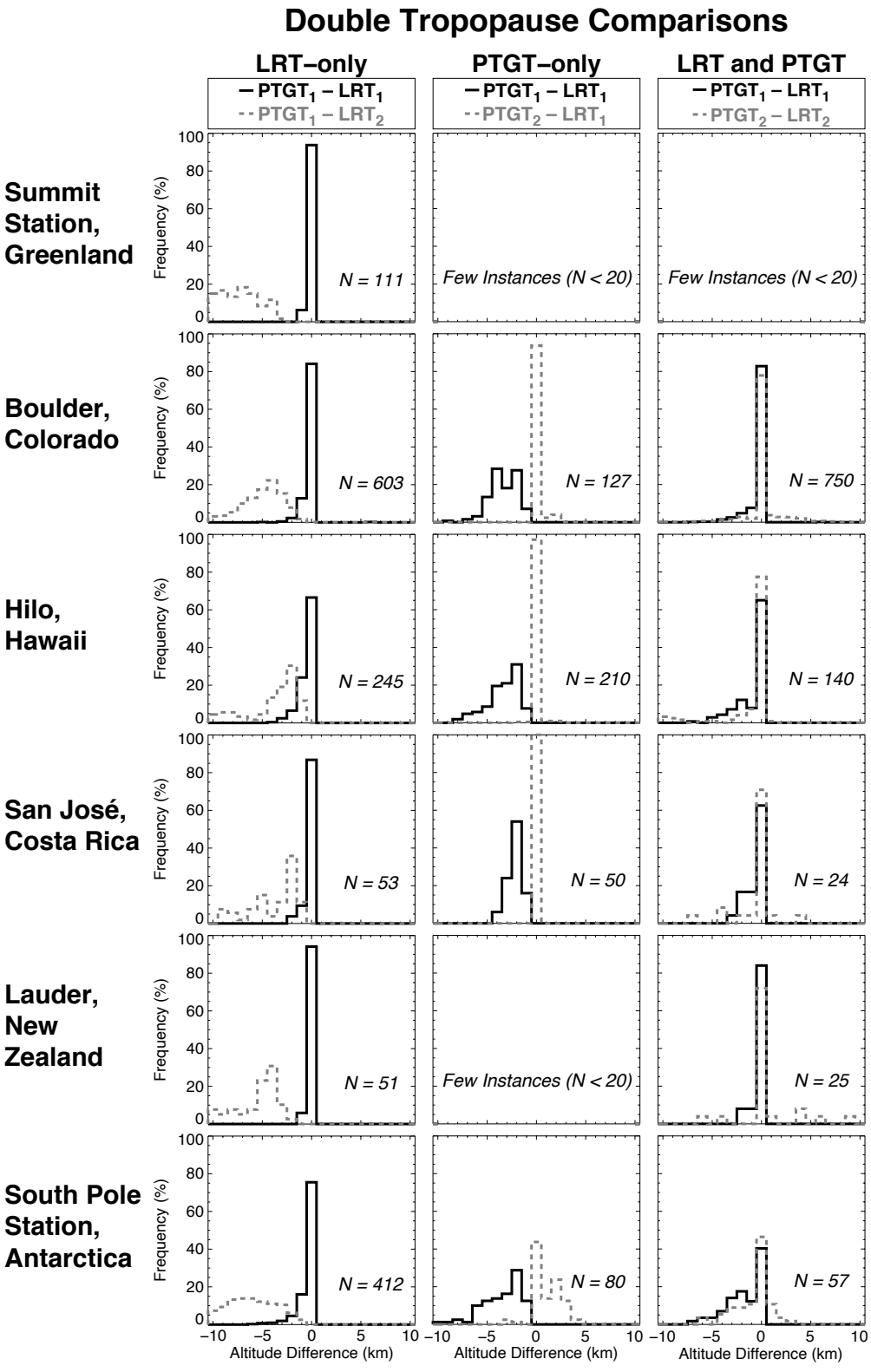
Double Tropopause Comparisons
LRT–only
PTGT–only
LRT and PTGT
PTGT1 – LRT1
PTGT1 – LRT2
PTGT2 – LRT1
PTGT2 – LRT2
Summit Station, Greenland
Boulder, Colorado
Hilo, Hawaii
San José, Costa Rica
Lauder, New Zealand
South Pole Station, Antarctica
Frequency (%)
Altitude Difference (km)
N = 111
Few Instances (N < 20)
Few Instances (N < 20)
N = 603
N = 127
N = 750
N = 245
N = 210
N = 140
N = 53
N = 50
N = 24
N = 51
Few Instances (N < 20)
N = 25
N = 412
N = 80
N = 57

Figure 3.13: Frequency distributions of tropopause altitude differences for profiles with a double tropopause (DT), using data from the six balloon sites. From left to right: profiles with a DT identified by only the LRT definition, only the PTGT definition, and both the LRT and PTGT definitions. For cases where only one tropopause definition identifies a DT, black solid lines indicate differences between the primary tropopause altitudes of the two definitions and dashed gray lines indicate differences between the secondary tropopause and the primary tropopause identified by the other definition. For cases where both the LRT and PTGT identify a DT, solid black lines indicate differences between primary tropopauses and dashed gray lines indicate differences between secondary tropopauses. The number of profiles used in each panel is noted.

stability change that does not satisfy the temperature threshold used in the LRT. This finding provides additional context to the analysis in Figure 3.10, where PTGT-relative temperature profiles exhibit characteristics of a DT environment.

3.3.3.3 Application to Reanalysis Output

Figures 3.14, 3.15 and 3.16 enable broader evaluation of the performance of the PTGT definition compared to the LRT. Both global maps (Fig. 3.14) and pole-to-pole cross sections at select longitudes (Fig. 3.16) demonstrate that, generally, there is broad consistency between the PTGT and LRT in each season. Namely, both definitions represent the tropopause break (indicated by the shift from dark purple to dark green in Fig. 3.14) similarly, as well as intricate dynamic features occurring in the midlatitudes. In Figure 3.15, DT features across the midlatitudes are also seen with broadly consistent identification between the definitions, though the DT areas identified by the LRT definition are slightly more expansive, which is consistent with the balloon observation DT frequency differences in Table 3.2.

There are a few additional key differences between reanalysis-derived PTGT and LRT altitudes worth noting. First, in high-tropopause environments, the PTGT tends to be lower than the LRT. Second, the high bias in LRT altitude in the polar regions is clearly resolved by the PTGT definition in these MERRA-2 examples, specifically

evidenced near the South Pole in July and October. Similarly, the LRT identifies a widespread (likely nonphysical) DT feature in the high Arctic during January (Fig. 3.15) that is not identified by the PTGT definition in this region. Lastly, in Figure 3.16, the consistency of each definition with the commonly-used dynamic tropopause is examined via several PV surfaces. In general, the PTGT primary tropopause more consistently aligns with the PV contours. This is especially apparent near the subtropical jets, where the PTGT primary tropopause follows the PV contours and identifies a secondary tropopause at higher altitudes where the LRT places the primary —and only— tropopause. Overall, the application of the PTGT algorithm to reanalysis is largely consistent with the observational analysis above for both primary and secondary tropopause identifications.

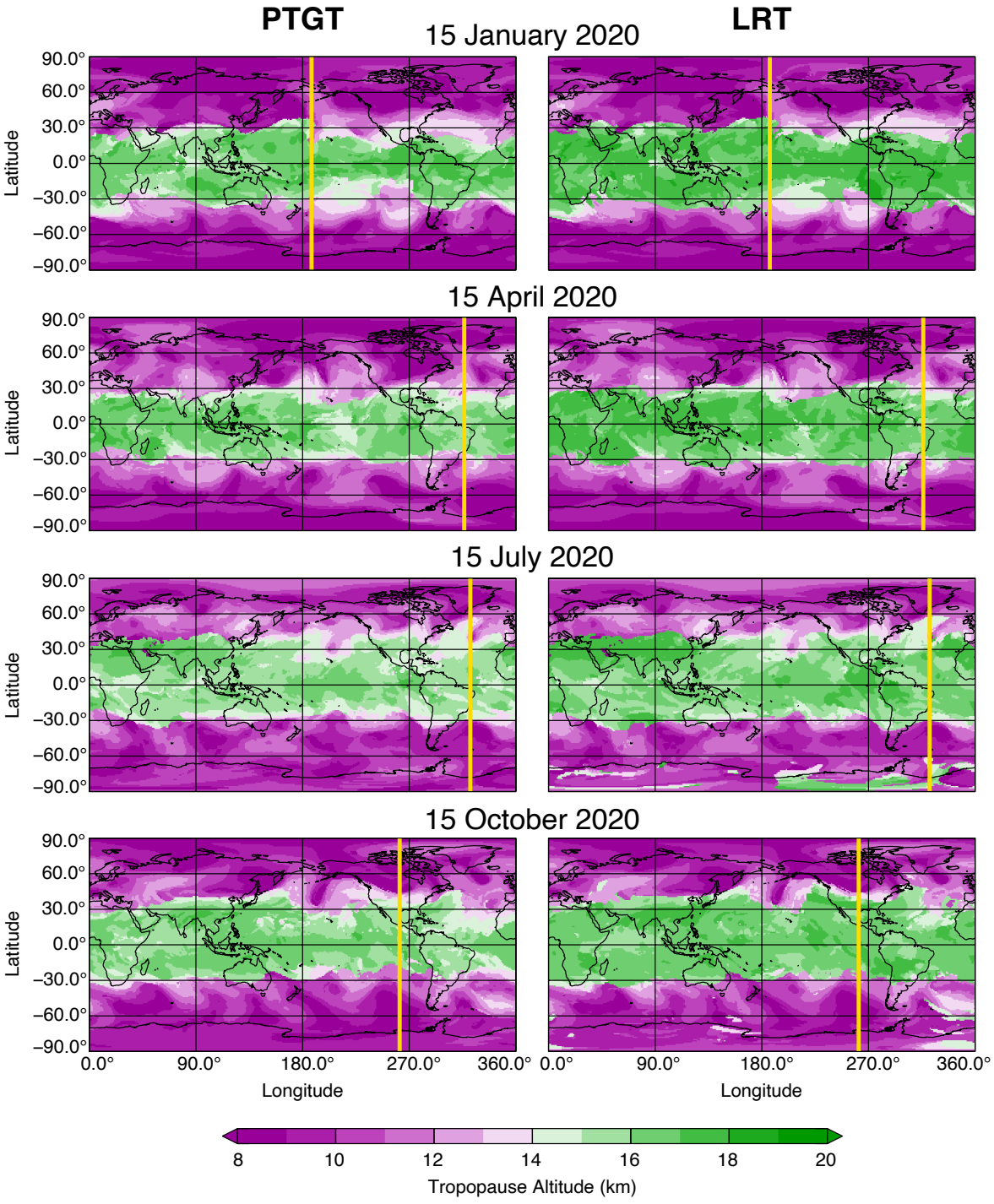

Figure 3.14: Maps of primary tropopause altitude diagnosed by the PTGT and LRT definitions for four select MERRA-2 reanalysis times: (top to bottom) 15 January 2020, 15 April 2020, 15 July 2020, and 15 October 2020. Thick yellow lines in each panel correspond to the locations of the vertical cross-sections in Fig. 3.16.

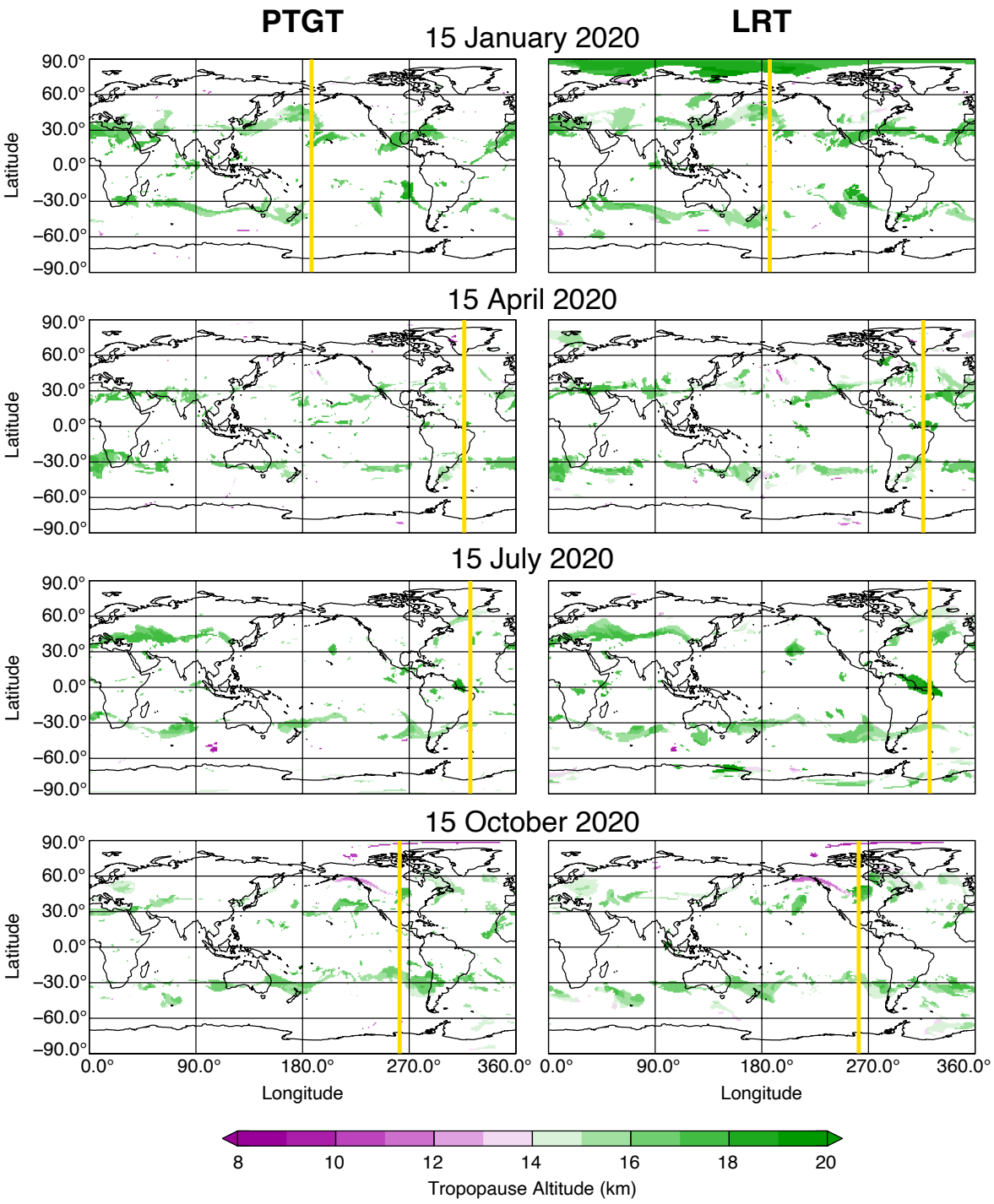

Figure 3.15: As in Fig. 3.14, but for secondary tropopause altitude when present.

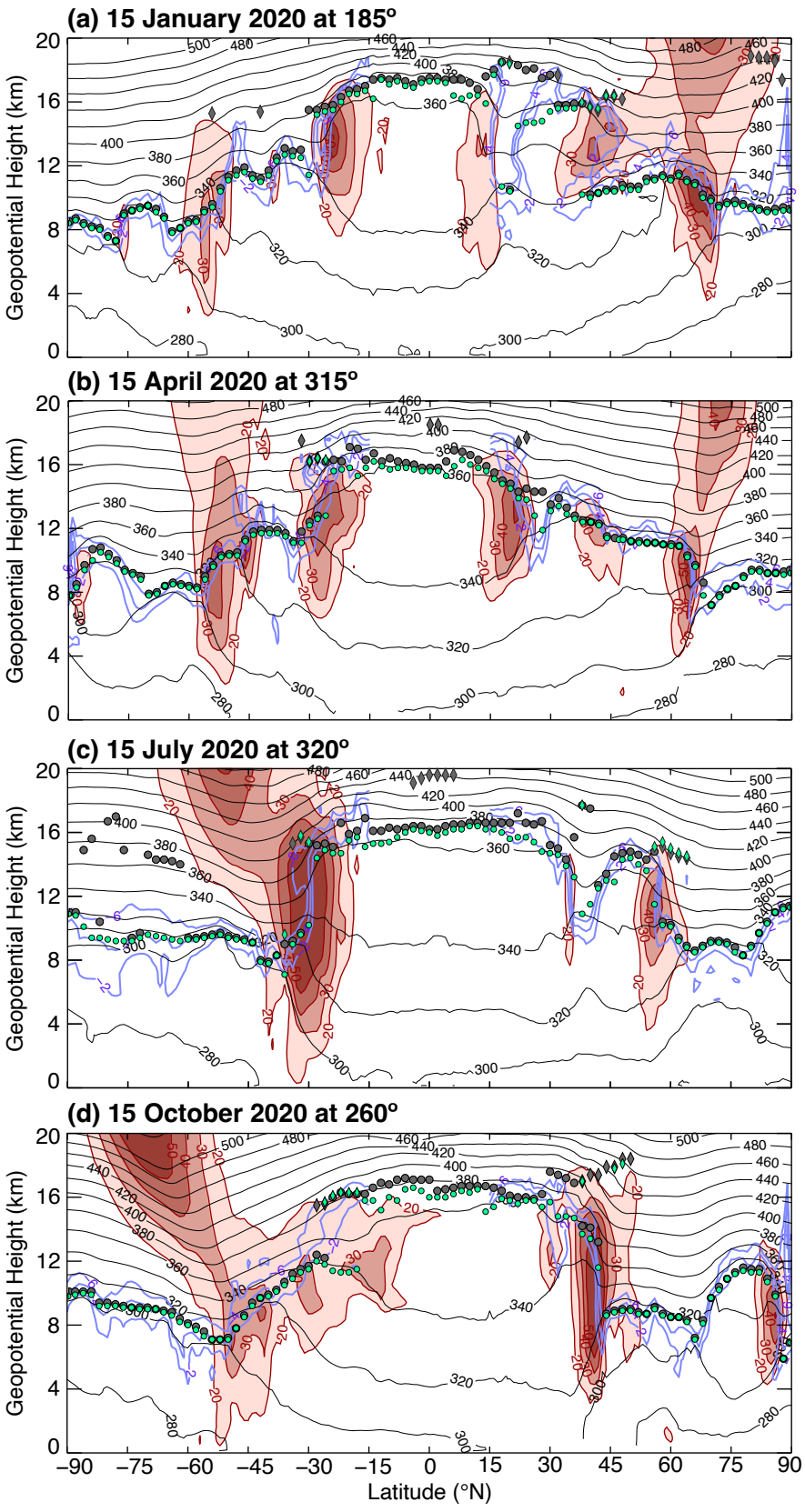
(a) 15 January 2020 at 185°
(b) 15 April 2020 at 315°
(c) 15 July 2020 at 320°
(d) 15 October 2020 at 260°
Geopotential Height (km)
Latitude (°N)

Figure 3.16: Pole-to-pole vertical cross-sections of MERRA-2 output for the four times in Fig. 3.14. Horizontal wind speeds are shown by the red color-filled contours (every 10 m s^{-1}, starting at 20 m s^{-1}), potential temperature (in K) by the black contours, potential vorticity above 4 km by the purple contours (every 2 PVU from ±2–6 PVU), PTGT altitudes by the green circles, PTGT secondary tropopause altitudes by the green diamonds, LRT altitudes by the gray circles, and LRT secondary tropopause altitudes by the gray diamonds.

Chapter 4

The Response of Tropopause-Overshooting Convection over North America to Climate Change

4.1 Background and Motivation

In recent years, there has been a growing body of evidence indicating that tropopause-overshooting convection has a larger impact on the composition of the upper troposphere and lower stratosphere (UTLS) than was previously thought, including the work presented in Chapter 2 (e.g., Chang et al. 2023; Homeyer et al. 2023; Tinney and Homeyer 2023; Clapp et al. 2021; Tinney and Homeyer 2021; Clapp et al. 2019; Herman et al. 2017; Smith et al. 2017; Randel et al. 2012; Hanisco et al. 2007; Dessler and Sherwood 2004). The alteration of concentrations of key greenhouse gases, like water vapor and ozone, are of particular interest due to the implications for the global radiation budget and associated climate change dynamics. Satellite-based studies, modeling studies, and *in situ* observations indicate that water vapor is particularly sensitive to convective influence, especially when a convective overshoot is accompanied by an above anvil cirrus plume (e.g., Homeyer et al. 2023; Gordon and Homeyer 2022; Homeyer et al. 2017). The recently completed Dynamics and Chemistry of the Summer Stratosphere (DCOTSS) field campaign dramatically increased the amount of *in situ* observations of convectively-enhanced water vapor (Homeyer et al. 2023) and will undoubtedly further our understanding of convective impacts on the UTLS

in the next few years. Both these recent and forthcoming advances motivate new exploration into tropopause-overshooting convection and its relationship to our climate system. Namely, how will tropopause-overshooting convection and its associated transport change in a warming climate?

The analysis tool that is used here to investigate the response of tropopause-overshooting convection to a warming climate is a convection-allowing model simulation that employs the pseudo-global warming (PGW) method, which has been used to examine climate change impacts to various convective-scale phenomena in recent years (e.g., Lasher-Trapp et al. 2023; Carroll-Smith et al. 2021; Trapp and Hoogewind 2016). The PGW method directly prescribes a climate change signal to a historical climate simulation by modifying its initial and boundary conditions. Notably, the synoptic forcing of the simulation is not altered from the historical state, allowing for a focused evaluation on the thermodynamic climate response in isolation from external dynamic — or baroclinic — changes (Brogli et al. 2023, and references therein). The PGW method has been successfully used to study potential climate impacts on derechoes, tropical cyclones, tornadoes, precipitation, and more (e.g., Lasher-Trapp et al. 2023; Carroll-Smith et al. 2021; Liu et al. 2017; Trapp and Hoogewind 2016; Rasmussen et al. 2011), and is used here to answer the following questions: (1) How does the frequency and distribution of tropopause-overshooting convection change in a warmed climate scenario? (2) How do tropopause characteristics and overshoot characteristics change in response to the prescribed warming signal?

4.2 Data and Methods

4.2.1 Model Output and Overshoot Identification

To employ the PGW approach for analyzing tropopause-overshooting convection in a warmed climate, this study makes use of three-hourly output from a pair of simulations from the Weather Research and Forecasting (WRF) model, Version 3.4.1. These simulations are comprised of a 13-year present-day control simulation (CTRL) and a future simulation (PGW) that encompasses all of CONUS and portions of Canada and Mexico (∼140–57°W longitude, ∼18–60°N latitude; Rasmussen and Liu 2017). The model has 51 vertical levels and a 4-km horizontal gridspacing, which is sufficient for resolving convection (Weisman et al. 1997). The model setup, experiments, improvements, and verification are described in detail in Liu et al. (2017) and are summarized in the following paragraph.

The CTRL simulation is forced by initial and boundary conditions from 6-hourly ERA-Interim reanalysis on a ∼0.75° longitude-latitude grid (Dee et al. 2011). In addition to initial and boundary conditions, spectral nudging is applied at scales >2000 km (i.e. synoptic scales) throughout the run while smaller scale processes are allowed to evolve freely. The same process is applied for the PGW simulation, with a modified input (WRF_{IN}) coming from the ERA-Interim analysis plus a climate perturbation, such that WRF_{IN} = ERA-Interim + $\Delta\mathrm{CMIP5}_{RCP8.5}$, where $\Delta\mathrm{CMIP5}_{RCP8.5}$ is the 95-year multi-model-ensemble-monthly-mean change signal using a worst case, RCP 8.5 emissions scenario in 19 CMIP5 models (see Table 1 in Liu et al. (2017)). The perturbed input fields include state variables such as geopotential, temperature, pressure, humidity, and horizontal winds, allowing the PGW approach to effectively capture the distinct physical response to climate warming in isolation from the dynamic response.

In this study, only a 10-year period (2003–2012 in CTRL, and the PGW equivalent) is used, which allows us to verify the model overshoots against recently improved radar and satellite datasets. However, note that February of 2005 is excluded from all analysis due to multiple missing times within the simulation in that month. In studying the UTLS, it is imperative that the vertical grid spacing is sufficient for representing tropopause-relative processes. The vertical grid spacing here is ∼500–600 m in the UTLS, which is appropriate for this study given the horizontal resolution of the model (Homeyer 2015).

In order to investigate the representation of tropopause-overshooting convection in both the CTRL and PGW simulations, two parameters — convective cloud top heights and tropopause heights — must be accurately determined. The assessment of convective cloud top heights involves identifying the altitude at which the frozen water mixing ratio (the combination of the three-dimensional model fields of snow, graupel, and ice mixing ratios) surpasses 0.1g/kg — a clear indicator of cloud presence. Additionally, the model cloud must be colocated with a model column-maximum reflectivity value of at least 50 dBZ to ensure there is a deep convective core simulated within the model. To determine tropopause heights, the model's three-dimensional temperature, pressure, and geopotential height fields are used to calculate the potential temperature gradient tropopause (PTGT; Tinney et al. 2022). A model grid point is then defined as overshooting when the cloud top height exceeds the PTGT altitude by a minimum of 0.75 km. The qualitative nature of the results are insensitive to this choice of threshold, which was ultimately chosen after comparison with observational data and to account for the vertical resolution of the model. For the 4-km latitude-longitude grid used here, an overshooting grid point is equivalent to 16 km^2 of overshooting area. For simplicity, I hereafter refer to individual overshooting grid boxes as "overshoots", though it is

emphasized here that in reality, neighboring overshooting grid points may comprise a single overshooting storm.

4.2.2 Observations and Overshoot Identifications

Radar data are sourced from the Next Generation Weather Radar (NEXRAD) network, which consists of more than 140 Weather Surveillance Radar-1988 Doppler (WSR-88D) systems over the contiguous United States (CONUS; Crum and Alberty 1993). Large-area mergers of data from individual radar sites, known as Gridded NEXRAD WSR-88D Radar (GridRad) data, allow for the analysis of radar data across the eastern two-thirds of the U.S (Homeyer and Bowman 2017). The GridRad algorithm is described in detail in Homeyer and Bowman (2017), but in summary, the algorithm is a four-dimensional time- and space-weighted binning procedure that merges single- and dual-polarization variables from individual radar sites into a large rectangular domain with a 0.2° longitude-latitude grid, vertical spacing of 1 km, and hourly temporal sampling. All quality-control methods recommended in Homeyer and Bowman (2017) are employed here, where low-confidence and infrequently-sampled echoes are removed to limit non-meteorological radar artifacts. For this study, three-hourly reflectivity fields coincident with the WRF model times are used. For this dataset, an overshooting grid point is identified where the 10 dBZ echotop height is at least 1 km above the tropopause, and the 20 dBZ echotop height is no more than 1 km below the tropopause, where the reference tropopause is the PTGT from the model CTRL experiment.

Three-hourly satellite imagery over North America is sourced from Geostationary Observing Earth Satellite (GOES) imagery, consisting of scans from GOES-8 (January 2003 – March 2003), GOES-12 (April 2003 – April 2010), and GOES-13 (April 2010 – December 2011). Note that GOES observations from 2012 are excluded here

due to a GOES-13 detection anomaly that resulted in unreliable overshoot identifications, specifically during October 2012. Outside of the anomaly, differences between the 9-year period used in this analysis and the full 10-year period are negligible. The overshoot identification methods used here are described in detail in Khlopenkov et al. (2021). Specifically, for an overshooting grid point to be identified, the infrared brightness temperature must be at a lower temperature than the PTGT height from the model CTRL experiment, which suggests that the satellite cloud tops are colder (and therefore higher) than the local tropopause. Additionally, the overshoot probability field is calculated as described in Khlopenkov et al. (2021) and is required to be 0.5 or greater for inclusion in the study, a threshold found to correspond to reliable overshoot detections (Cooney et al. 2021). Parallax adjustments to each GOES image are made prior to analysis based on a cloud top height estimate from IR temperature matching with a corresponding MERRA-2 temperature and altitude profile. Consistent with the model overshoot analysis described above, overshooting grid points in both the GridRad and GOES datasets are referred to as "overshoots", for simplicity.

4.3 Results

4.3.1 Model Validation

To evaluate the ability of the WRF model to represent the frequency and regional distribution of tropopause-overshooting convection in the historical simulation, the CTRL experiment is evaluated against the GridRad and GOES datasets described above. The average annual densities of tropopause-overshooting convection events for GridRad, GOES, the CTRL experiment are shown in Fig. 4.1a–c for evaluation of the model CTRL experiment. The overall spatial distribution is reasonably consistent between the observational data and the CTRL experiment, with a large frequency

maximum occurring over the U.S. Great Plains. Assessing spatial consistency outside of the CONUS is challenging due to the different limitations of each dataset's domain (outlined in Fig. 4.1). Nonetheless, smaller peaks, both in intensity and spatial coverage, are observed in both the CTRL experiment and at least one of the observational datasets. Specifically, the CTRL experiment and GOES both identify frequent overshoots over the Sierra Madre Occidental and the coastal northern Atlantic, and a small maximum is seen over Florida in both the model and GridRad. Unfortunately, the validity of the overshoots located over Cuba in the CTRL experiment can not be evaluated against either of the observational datasets. For the frequency of tropopause-overshooting convection, there are notable differences between each dataset. Namely, overshoots are most frequent in GridRad, followed by the model CTRL, and finally, by GOES. The horizontal spatial resolution of the GOES data is lower than that of GridRad and the model, which is likely at least partially responsible for fewer identifications in this dataset, as GOES is unlikely to be able to detect smaller overshoots that are detectable in GridRad and the model (Cooney et al. 2021). However, it should be noted that some of these differences may be attributed to the specific overshoot thresholds used in each dataset. It is also important to note that the GridRad domain shown in Fig. 4.1a does not account for the observational limitations of the data (i.e., that the radars are confined to CONUS) and therefore sufficient GridRad sampling is primarily confined to CONUS and just along/off the coasts (e.g. Cooney et al. 2018, 2021).

The dataset limitations increase the complexity of assessing the model performance in capturing the spatial distribution of tropopause-overshooting convection. For example, overshoots in the model are more prolific than in GOES over the Sierra Madre and along the southern Texas/Mexico border. However, given that GOES is consistently

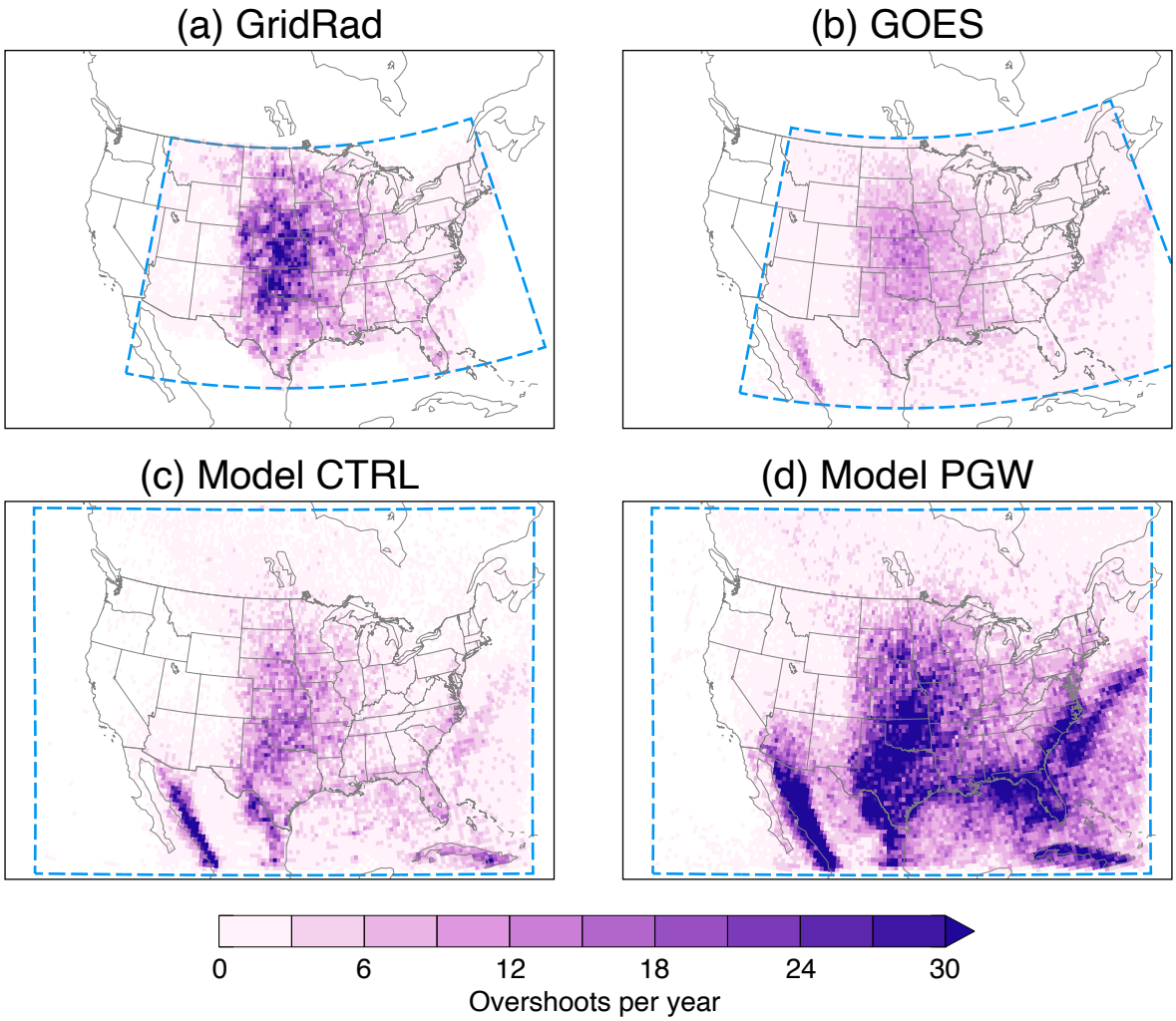

Figure 4.1: The average number of overshoots per year placed into 0.4° latitude-longitude bins for (a) GridRad, (b) GOES, (c) the WRF CTRL experiment, and (d) the WRF PGW experiment. The domain bounds of each individual dataset are indicated by the blue dashed lines.

observing lower numbers of overshoots than GridRad within CONUS, it is not unreasonable to extrapolate that the model CTRL frequencies are more reasonable than GOES over these regions. In other words, GOES may be under-sampling tropopause-overshooting convection in these regions rather than these events being over-simulated in the model. Additionally, temperature-based overshoot identifications such as GOES are susceptible to thermodynamic modifications of overshoot characteristics, such that the overshoot temperature may be influenced by the surrounding lower-stratospheric temperatures. This may be especially exacerbated in these high-tropopause environments where there is a strong tropopause inversion layer and therefore warmer stratospheric temperatures, which would result in less reliable temperature-based overshoot identifications.

In addition to spatial distributions, it is important to assess the model's ability to adequately reproduce the annual and diurnal cycles of overshoot occurrence. Figure 4.2 shows the average annual cycle of tropopause-overshooting convection in GridRad, GOES, and in the model CTRL experiment. The frequency variation between each dataset is well-demonstrated here, with all datasets showing a peak in overshoot occurrence in June but at varying counts of $\sim$7000, 6500, and 4200 overshoots per year for the model CTRL, GridRad, and GOES, respectively. To better assess the relative annual cycle of each dataset, Fig. 4.2 also shows the cycle normalized by magnitude. While the number of overshoots in each dataset peaks in June, the timing of each cycle varies. Specifically, the cycle in the model simulation trails that of GridRad and GOES, indicating the model may be underestimating overshoot occurrence in Boreal springtime, and overestimating it in late summer and fall. It is important to note, however, that the varying domains of each dataset are likely contributing to some of these differences, which is further investigated below. The diurnal cycles of each dataset are

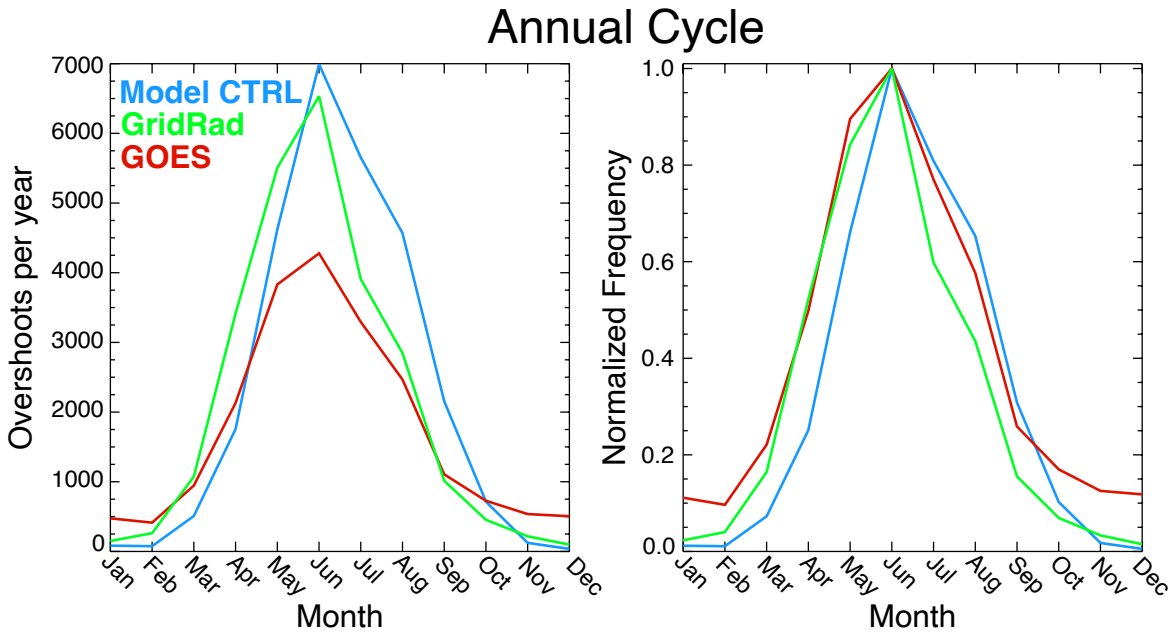

Figure 4.2: The average annual cycle of (blue) the CTRL experiment, (green) GridRad, and (red) GOES across their respective domains shown in Fig. 4.1 displayed as both the total counts of overshoots (left) and as normalized frequencies (right).

shown in Fig. 4.3, where the difference in the overall number of overshoots in each dataset is once again reflected. Note that each dataset was transformed into Local Solar Time (LST; i.e., relative to solar noon) and subsequently rebinned into the original three-hourly timesteps. The normalized diurnal cycle indicates broad consistency in the relative cycles of the model CTRL experiment and GridRad with strong peaks at 3 p.m. LST, while GOES trails and peaks at 6 p.m. LST. Additionally, the amplitudes of the normalized cycles differ, where GOES observed a higher relative percentage of overshoots overnight compared to GridRad and the model. The temporal lag in GOES may again be explained by differences in horizontal resolution, where overshoots are likely smaller (and therefore more likely to be missed by GOES) during their initial development. Additionally, storm tops may not be optically thick during their early development, which could also lead to lower detection rates (Cooney et al. 2021).

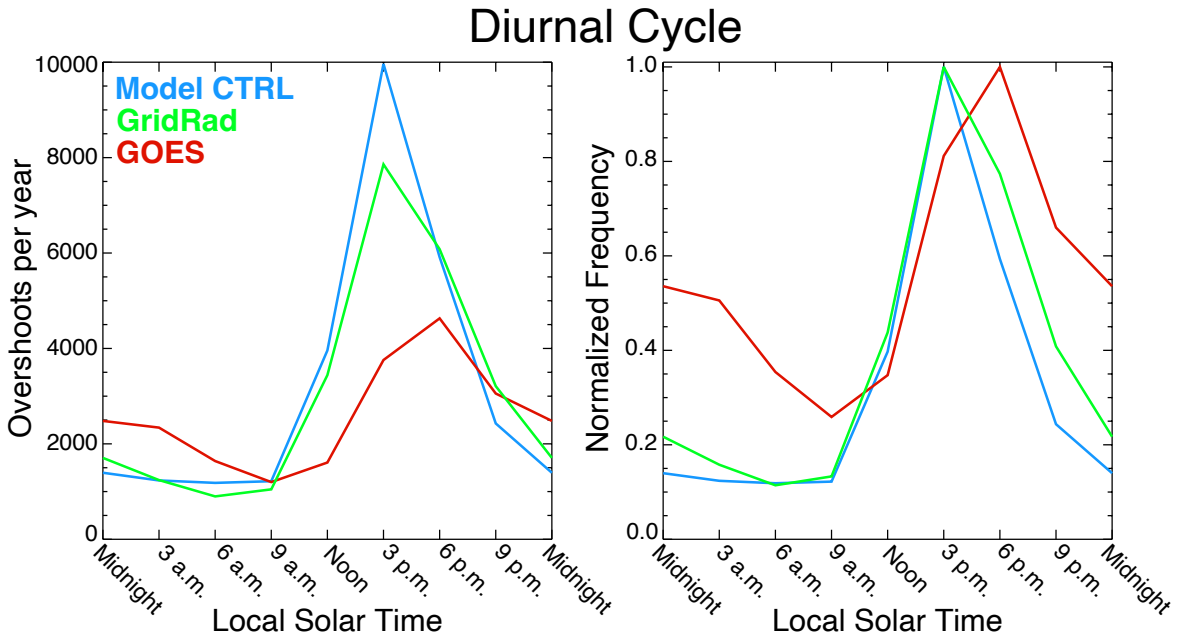

Figure 4.3: As in Fig. 4.2, but for the diurnal cycle.

The annual and diurnal cycles of convection are not constant across North America. Therefore, it is important to evaluate how the model is representing these cycles on a regional basis. To determine specific regions of interest, I examine the difference between the model CTRL and PGW simulations at subjectively-selected locations with prominent and statistically significant projected increases in overshoot occurrence (Fig. 4.4a). A CONUS domain that is well sampled by all datasets is also defined, which is designated here as the "common domain". The analysis is then performed on these six individual regions identified in Fig. 4.4: the common domain, the Sierra Madre, the Northern Plains, the Southern Plains, the Gulf Coast, and the East Coast.

Figure 4.5 shows the annual cycle of overshoots in GridRad, GOES, and the model CTRL experiment for each region. When the analysis is restricted to the common domain only (Fig. 4.5a), the model CTRL annual cycle is more closely aligned to observations than the results for the full domain analysis in Fig. 4.2. This is primarily

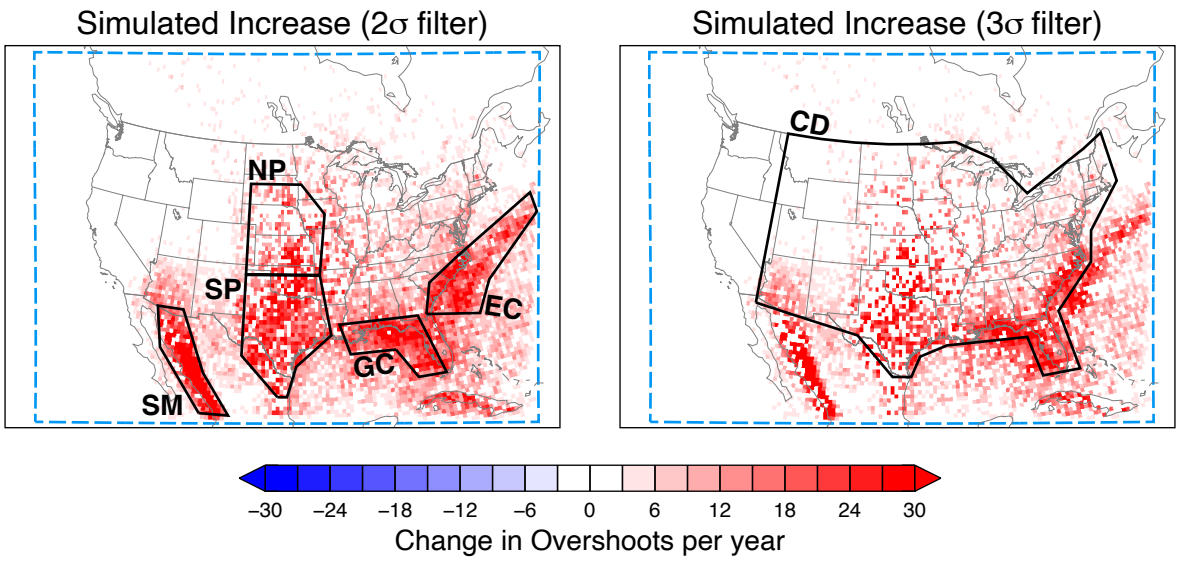

Figure 4.4: The change in the number of overshoots per year from the CTRL experiment to the PGW experiment in 0.4° latitude-longitude bins. Only bins in which the PGW experiment mean exceeds 2 standard deviations (left) and three standard deviations (right) of the CTRL experiment are shown. Regions of large increases are identified by the black polygons for further regional analysis: the Sierra Madre (SM), the Northern Plains (NP), the Southern Plains (SP), the Gulf Coast (GC), the East Coast (EC), and the domain that is common to and well sampled by all three datasets (Common Domain, CD). The model domain is indicated by the blue dashed lines.

due to the exclusion of regions with late-Summer peaks, such as the Sierra Madre and coastal regions, resulting in a closer match between the model's annual cycle and the observed data. Regarding the magnitude of the cycles, the model simulates overshoots at a frequency between that of GOES and GridRad in the common domain, the Northern Plains, and the Southern Plains. For the Sierra Madre, the Gulf Coast, and the East Coast, the model produces overshoots at a substantially higher rate than both GridRad and GOES, though it is important to note that these regions are either poorly sampled or not sampled at all by GridRad. Notable disparities between the annual cycle of the CTRL experiment and the observations are evident in the Gulf Coast and the East Coast in Fig. 4.5e,f, where the model depicts a strong late-summer peak that is absent in the observations. I emphasize again here that it is difficult

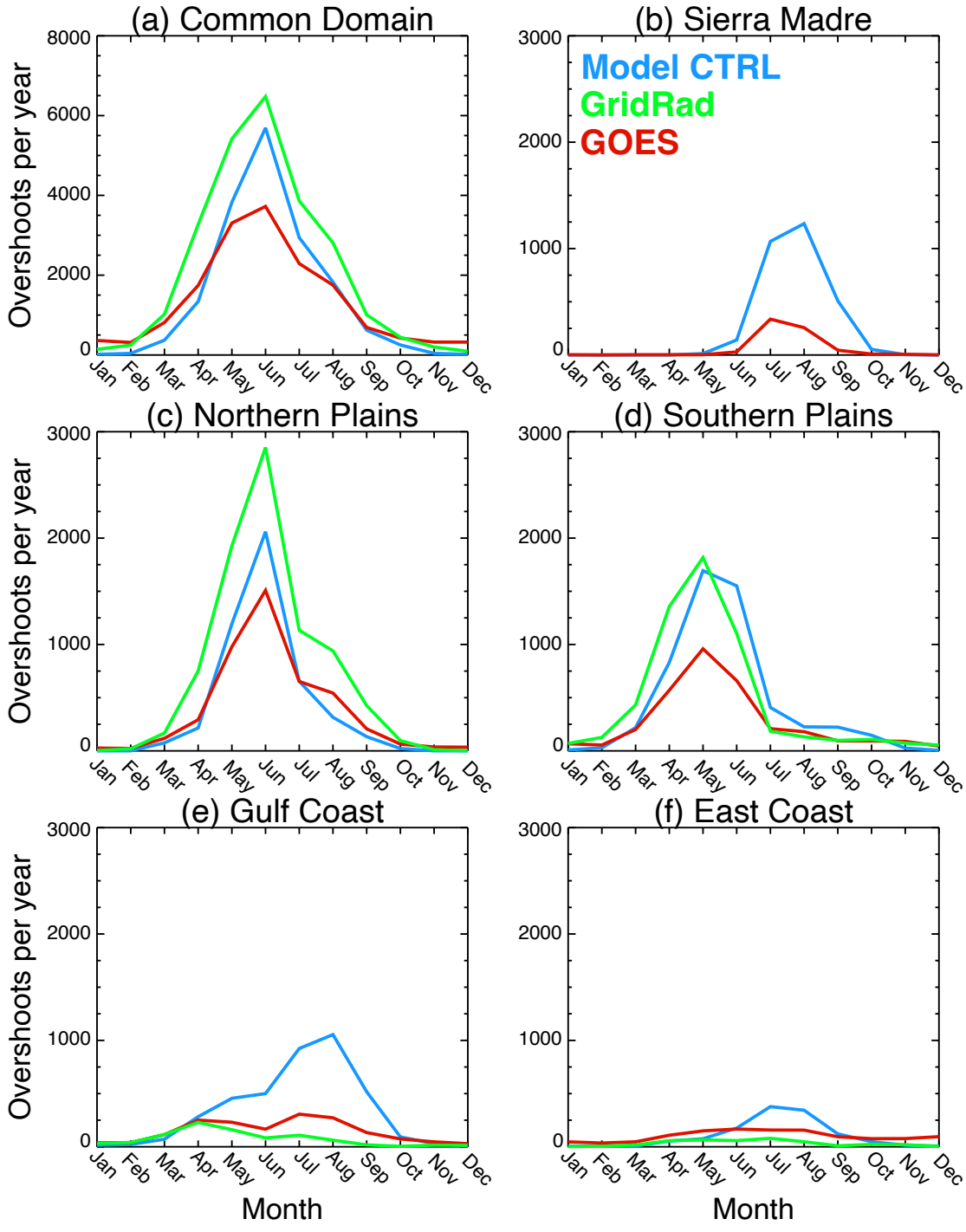

Figure 4.5: The average annual cycle of (blue) the CTRL experiment, (green) GridRad, and (red) GOES for the (a) Common Domain, (b) Sierra Madre, (c) Northern Plains, (d) Southern Plains, (e) Gulf Coast, and (f) East Coast regions as identified in Fig. 4.4.

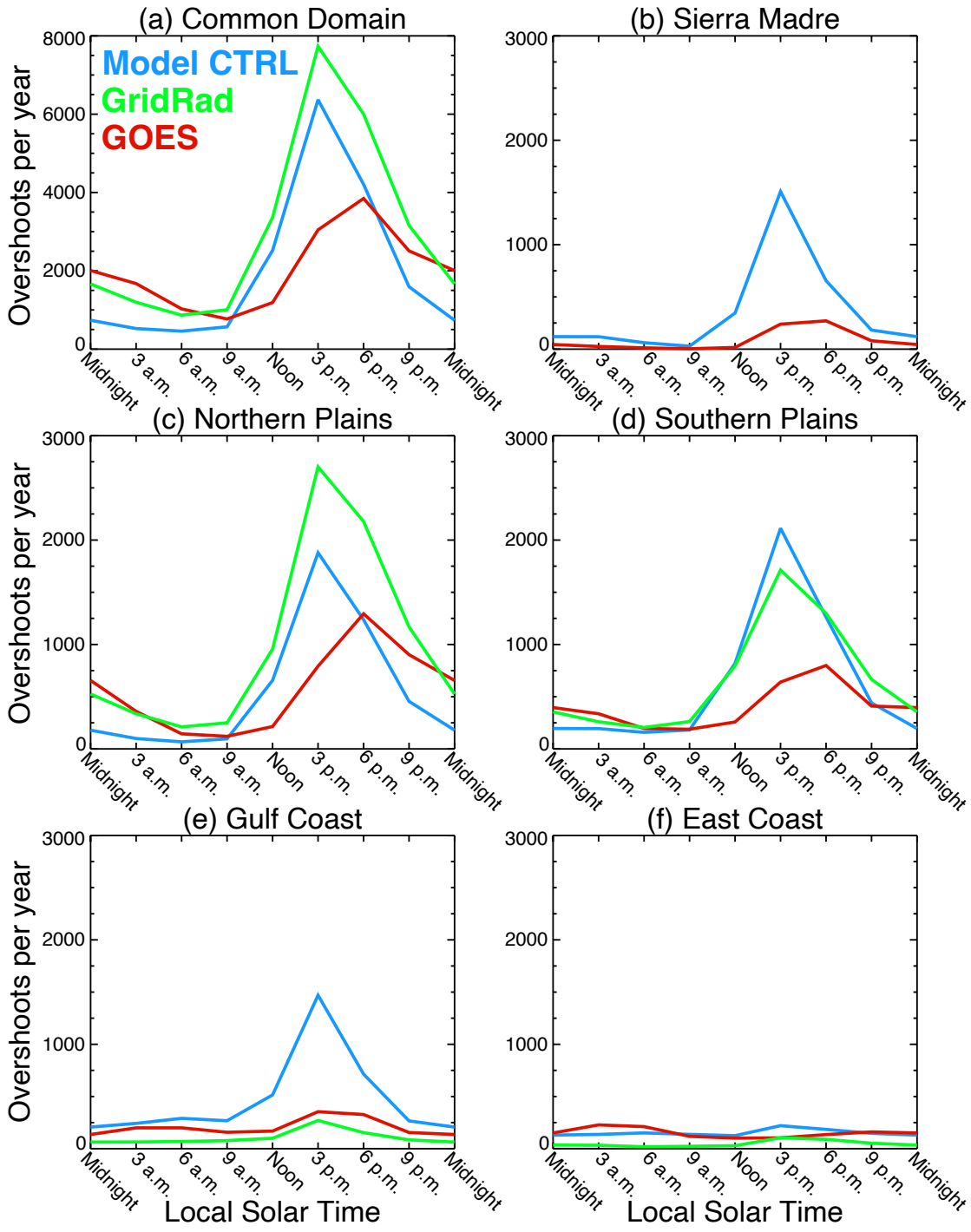

Figure 4.6: As in Fig. 4.5, but for the diurnal cycle.

to determine how much of this is a potential over-estimation by the model versus limitations in our observing capabilities over these regions. The regional diurnal cycles shown in Fig. 4.6 show patterns similar to that of the overall diurnal analysis in Fig. 4.3. Specifically, the model CTRL and GridRad are well aligned while the GOES cycle consistently trails behind by ∼3 hours. As noted previously, this is likely related to overshoot detection being more difficult in GOES with smaller developing overshoots.

Overall, the agreement between the historical model simulation and observations of overshooting from radar and satellite is encouraging. Discrepancies arising from variations in the domain bounds, observing resolutions, and detection methods among the datasets pose challenges to making a comprehensive comparison. However, the qualitative findings are clear: the WRF model effectively captures the regional distribution, annual cycle, and diurnal pattern of tropopause-overshooting convection in a way that is consistent with reality.

4.3.2 Overshoot Frequency

With confidence in the ability of the model to reproduce observed patterns and frequencies of overshooting, the projection of tropopause-overshooting convection in the PGW experiment can now be assessed. Figure 4.1d presents the number of overshoots in the PGW model run in comparison to GridRad, GOES, and the CTRL experiment, with dramatic results. A broad increase in overshoot count is apparent across virtually the entire domain. This is also demonstrated in Fig. 4.4, which shows the change in the number of overshoots per year from the CTRL to the PGW experiment. Only statistically significant changes are displayed, determined as where the PGW 10-year mean exceeds two or three standard deviations from the CTRL experiment. Substantial and

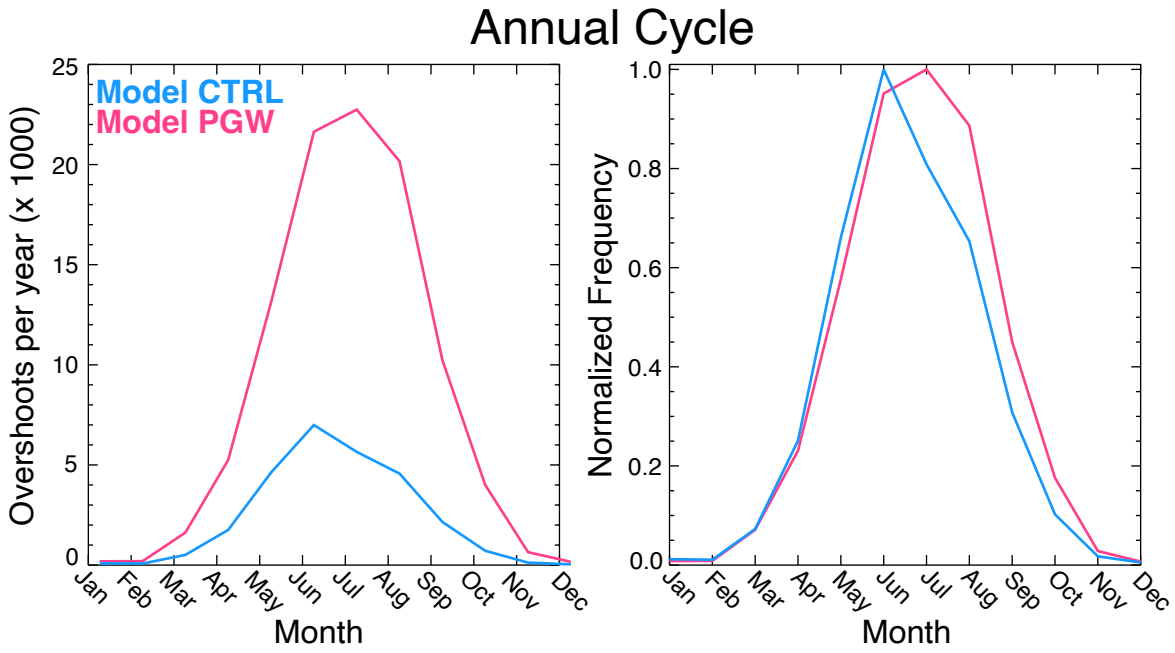

Figure 4.7: The average annual cycle of (blue) the CTRL experiment and (pink) the PGW experiment displayed as both the total counts of overshoots (left) and as normalized frequencies (right).

widespread increases are found throughout the model domain. These increases are further assessed by examining the annual cycle of both the CTRL and PGW simulations in Fig. 4.7. There is a robust increase in the number of overshoots throughout the entire annual cycle, which peaks at ∼23 000 overshoots per year in the PGW simulation compared to ∼7000 per year in the CTRL. Accumulated over the entire annual cycle, the PGW experiment projects a total of ∼1 000 000 overshoots per year across the domain, representing an increase of over 250% from the ∼273 000 total overshoots per year in the CTRL. In addition to the remarkable increase, a shift in the relative seasonal cycle is observed. The PGW annual cycle reaches its peak in July rather than June, indicating an apparent extension of the active overshooting season, with occurrences becoming more frequent in the latter half of the year. This result stands in contrast to results from previous studies that examined the severe weather response to climate

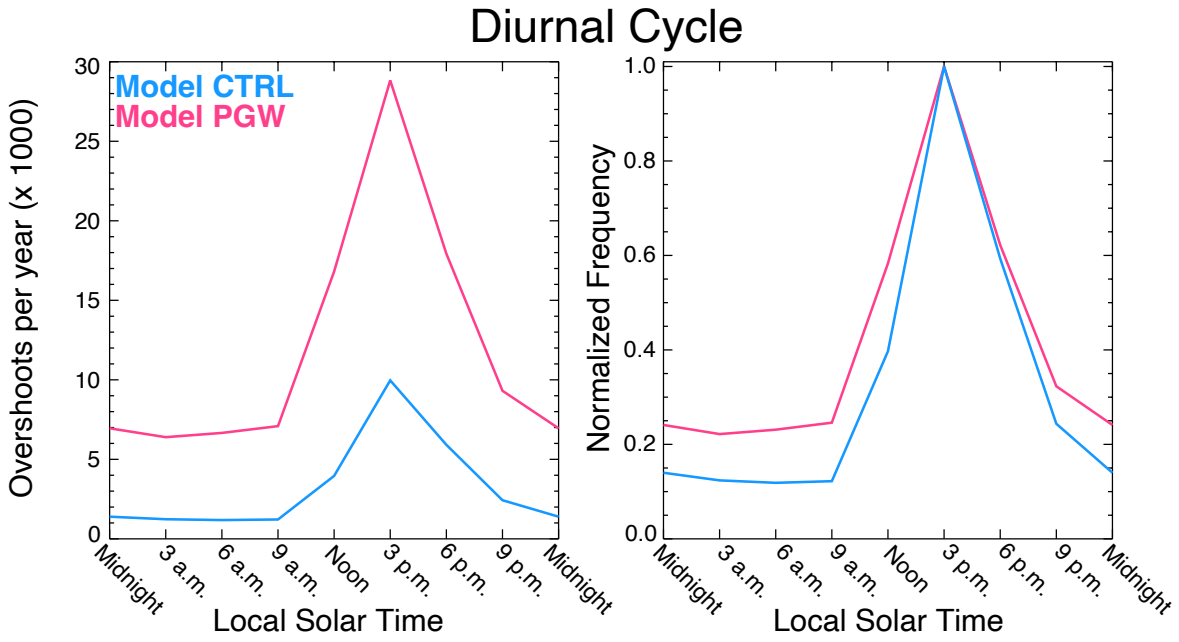

Figure 4.8: As in Fig. 4.7, but for the diurnal cycle.

change, which have projected an increase in the severe weather season that is primarily driven by events earlier in the year (e.g., Hoogewind et al. 2017). However, the PGW method does not account for climate-driven changes in synoptic patterns that would potentially impact these seasonal shifts. Finally, the diurnal cycles for the simulations are shown in Fig. 4.8, where the magnitude difference between the two simulations is still glaringly clear. However, the normalized cycle indicates that while the diurnal cycle remains largely consistent between the two simulations, the PGW simulation has a larger relative increase in the overnight and early morning hours. This indicates that strong nighttime tropopause-overshooting convection may become more frequent in a warming climate.

To determine if there are specific areas over North America driving these changes, the annual and diurnal cycles for the regions highlighted in Fig. 4.4 are once again examined. The annual cycles for these regions are shown in Fig. 4.9, where there are some discernible differences in the nature of the changes between regions. Specifically,

the projected increases can be categorized into two main components: amplification and seasonal extensions. In the Sierra Madre, the Northern Plains, and the East Coast, the changes primarily manifest as amplification, leaving the relative annual cycle mostly unchanged. Conversely, the shape of the cycles in the Southern Plains and Gulf Coast regions are slightly altered, with notable disproportionate increases in the number of overshoots in late summer and early to mid-summer, respectively. This regional analysis suggests that the overall extension of the common overshooting season within the model domain can be largely attributed to a combination of amplification occurring in the Sierra Madre and Gulf Coast regions and a late-summer seasonal extension in the Southern Plains. The diurnal analysis for each region in Fig. 4.10 is largely similar and consistent with the depiction of the diurnal cycle in Fig. 4.8, where there is a relative increase in the proportion of tropopause-overshooting convection events occurring in the overnight and early morning hours.

4.3.3 Tropopause and Overshoot Characteristics

The analysis above projects that the occurrence of tropopause-overshooting convection could more than double in a future climate scenario. This indicates that of the projected environmental changes, those that are conducive to tropopause-overshooting convection (like increased CAPE) outweigh those that would act to hinder overshooting convection, like an increase in tropopause height. Therefore, it is important to investigate how the model is representing changes in tropopause height in the simulations. The change in average tropopause altitude from the CTRL to the PGW experiment is shown in Fig. 4.11. On an annual basis, tropopause heights increase by $\sim$0.5 km from the CTRL to the PGW simulation across most of the domain, with larger increases occurring farther south. When the analysis is broken up by season, there are some

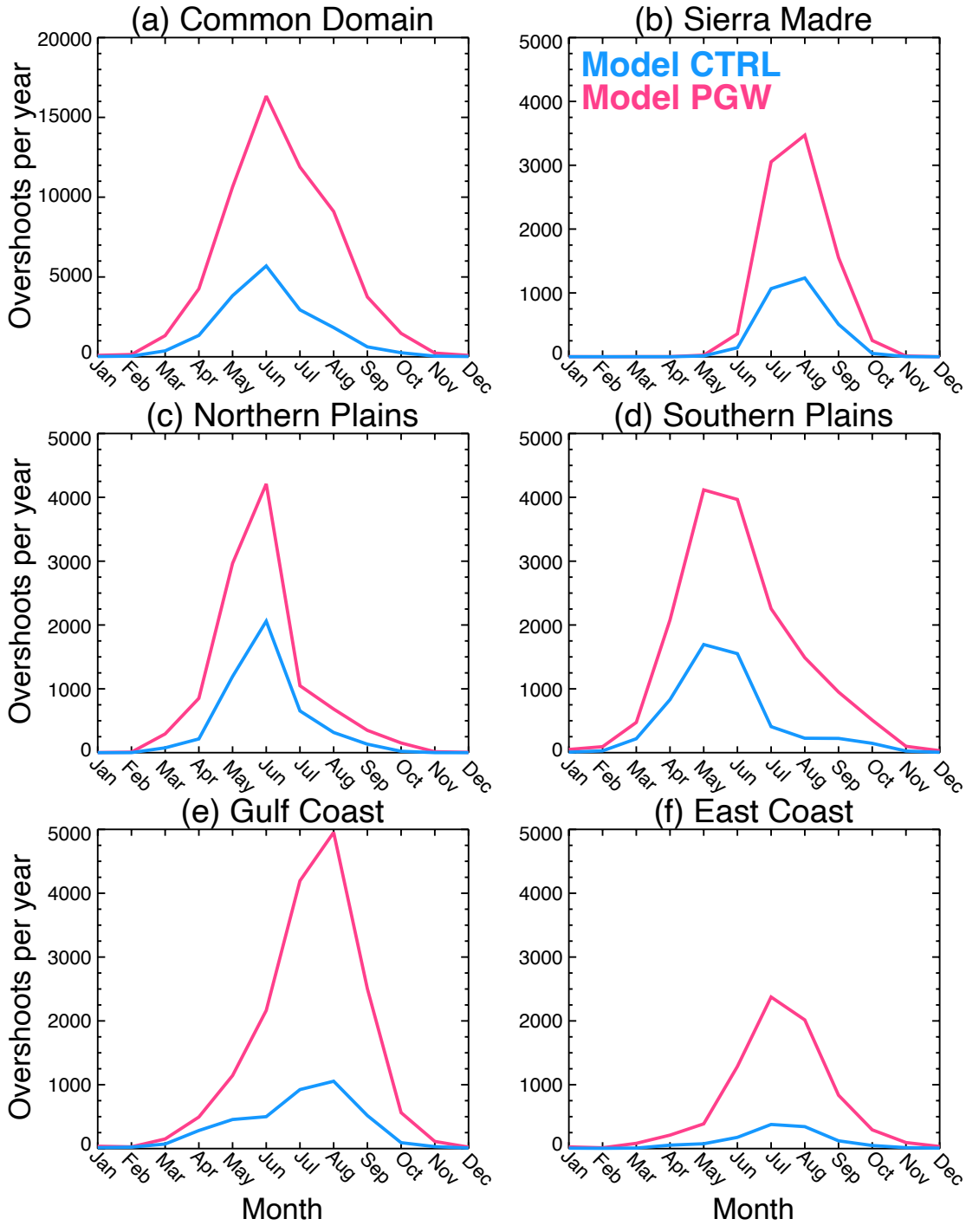

Figure 4.9: The average annual cycle of (blue) the CTRL experiment and (pink) the PGW experiment for the (a) Common Domain, (b) Sierra Madre, (c) Northern Plains, (d) Southern Plains, (e) Gulf Coast, and (f) East Coast regions as identified in Fig. 4.4.

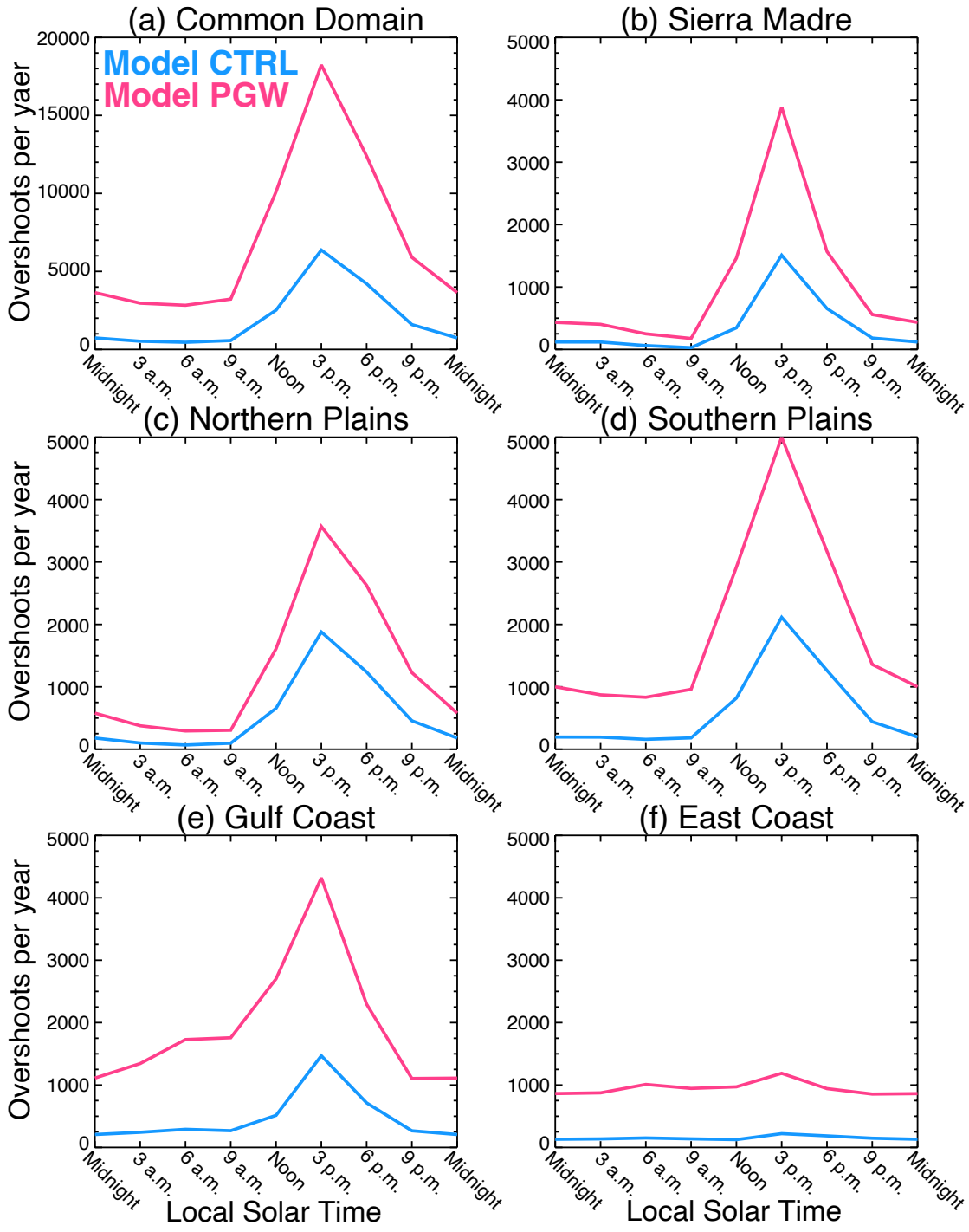

Figure 4.10: As in Fig. 4.9, but for the diurnal cycle.

variations in the location of greatest tropopause increase. Seasonal analysis reveals variations in the locations of the most significant tropopause increases. During winter and spring, the most substantial elevation changes are observed at the southern end of the domain, while during summer and fall, greater increases occur further northward. Notably, in each season, the most substantial tropopause increases align with the strongest north-south gradient in mean CTRL tropopause height. This suggests that the tropopause height changes would occur in the vicinity of the subtropical jet stream and accompanying discontinuity in tropopause height known as the "tropopause break" (Randel et al. 2007a). These results demonstrate that the PGW method is simulating tropopause height in ways that are consistent with previous work.

The analysis thus far suggests that despite increasing average tropopause heights, tropopause-overshooting convection will become more frequent in the future. This motivates further investigation into the characteristics of the overshoots, specifically if there are any projected changes in the average depth of overshoots or any projected changes in tropopause height during active overshooting events. Figure 4.12 shows the number of overshooting events at various depths throughout the CTRL and PGW simulations. Notably, the PGW experiment not only amplifies the occurrence of overshooting events but also escalates the probability of extreme overshoots. For example, overshoots of 4 km in depth are approximately a twice yearly event in the CTRL experiment (18 total overshoots of this depth in the ten year period) while the PGW experiment sees $\sim$5 overshoots at this depth per year. Overshoots with a depth of 5 km are a one-in-five-year event in the CTRL experiment (i.e. two events throughout the ten year period), while the PGW experiment simulates these approximately two

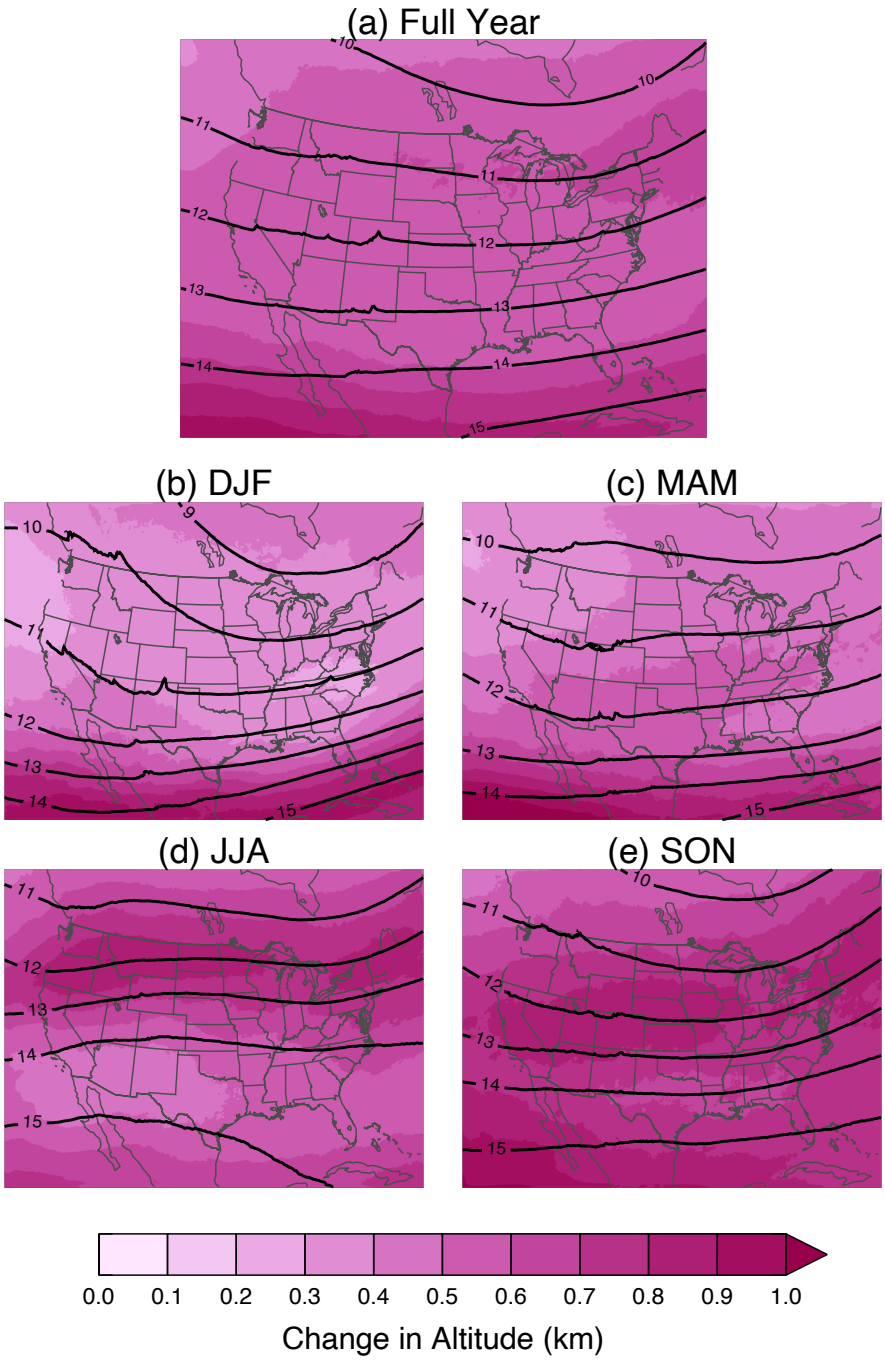

Figure 4.11: The change in average PTGT altitude from the CTRL experiment to the PGW experiment (color shading) with average CTRL PTGT heights overlaid as black contours for (a) the full year, (b) December, January, and Febuary (DJF), (c) March, April, May (MAM), (d) June, July, August (JJA), and (e) September, October, November (SON).

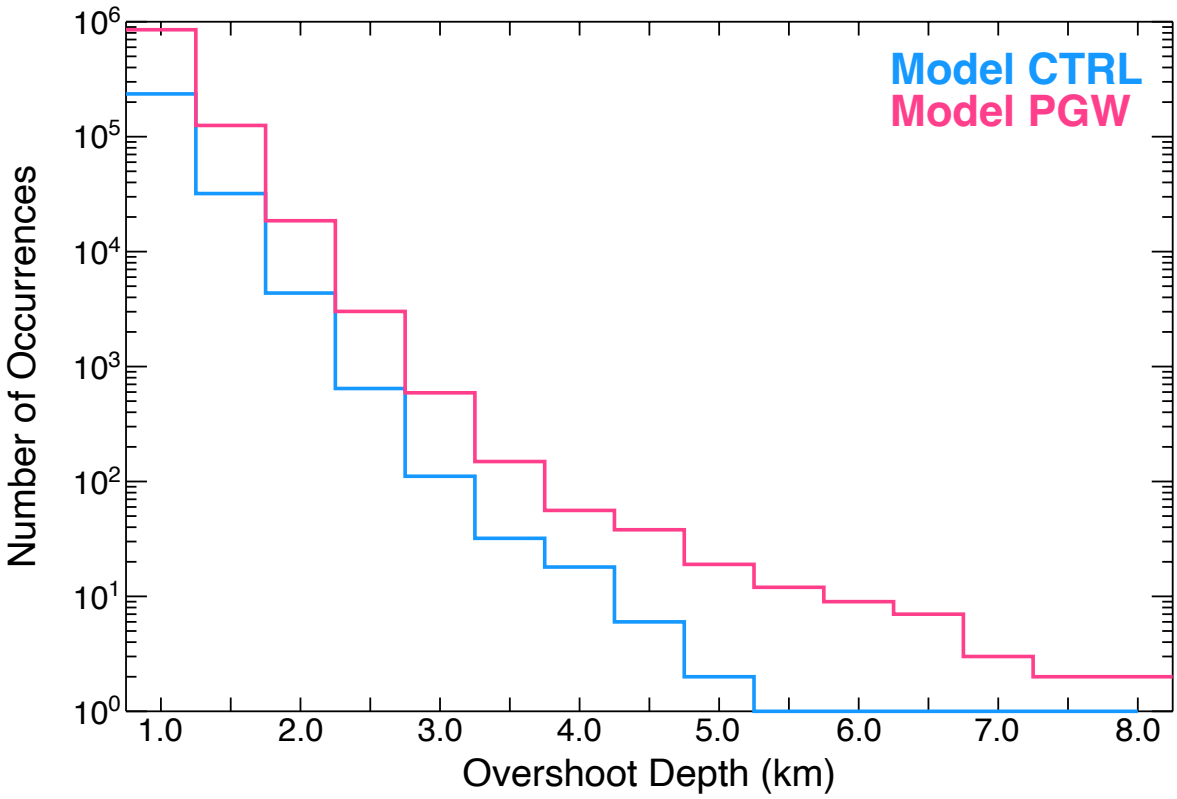

Figure 4.12: Histograms of overshooting depth for the CTRL experiment (blue) and the PGW experiment (pink), with 0.5 km bin sizes. Note that the ordinate is logarithmic.

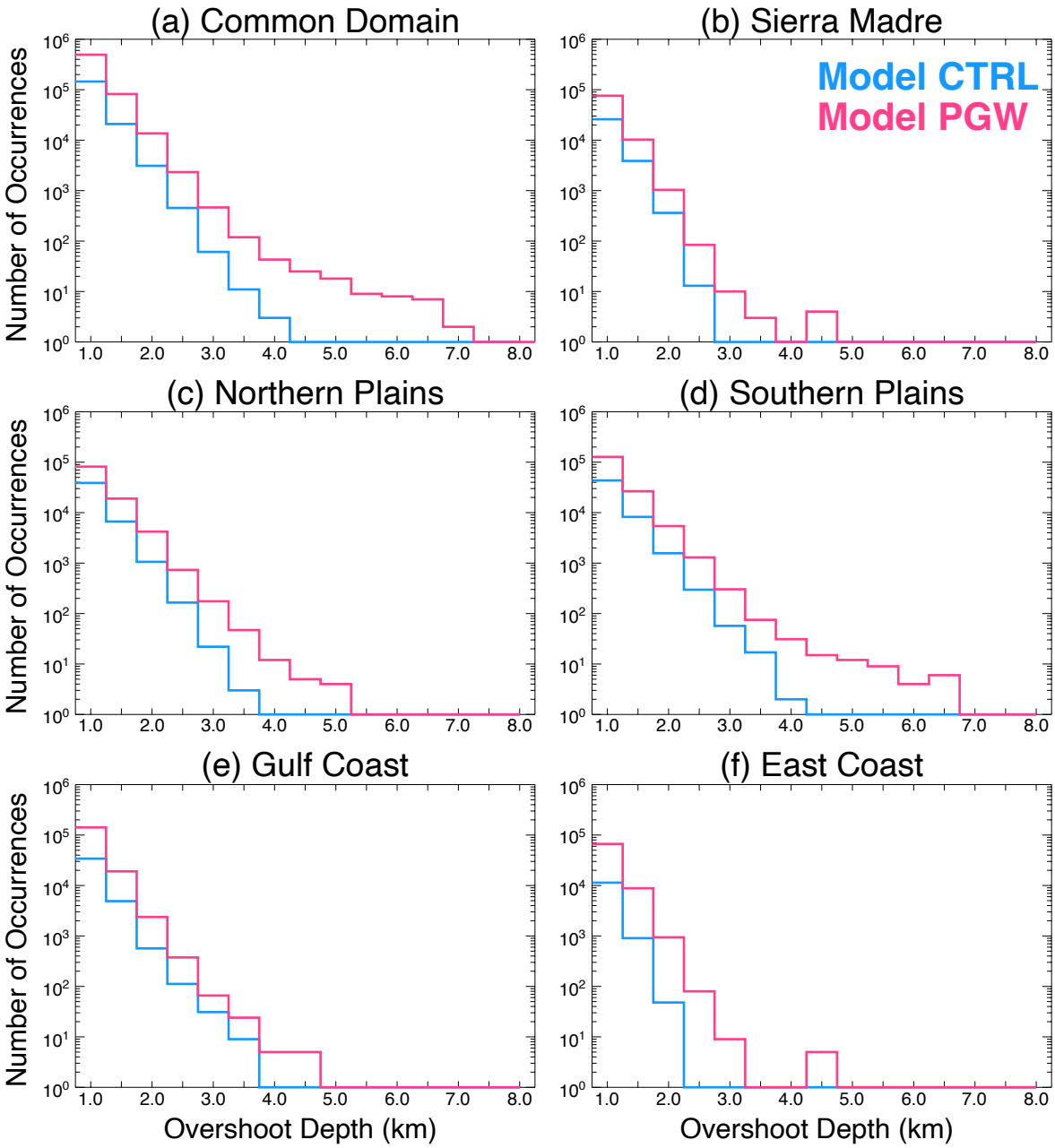

Figure 4.13: Histograms of overshooting depth for the CTRL experiment (blue) and the PGW experiment (pink), with 0.5 km bin sizes for the (a) Common Domain, (b) Sierra Madre, (c) Northern Plains, (d) Southern Plains, (e) Gulf Coast, and (f) East Coast regions as identified in Fig. 4.4. Note that the ordinates are logarithmic.

times a year. When this analysis is performed regionally (Fig. 4.13), it becomes apparent that the increase in extreme overshooting depths is largely driven by increases in the Plains regions, especially the Southern Plains.

To determine whether overshoots are becoming more frequent in lower tropopause environments or if overshoots are becoming more frequent in all environments, tropopause altitude distributions during overshoots only in both simulations are investigated (Fig. 4.14). In the CTRL experiment, there is a fairly symmetric distribution in tropopause altitudes centered around 14 km. In the PGW experiment, however, this distribution becomes largely skewed towards higher altitudes with a mode of 16 km occurring $\sim$30% of the time. This demonstrates that convection in a warmed climate scenario is able to regularly overshoot the increased tropopause heights; additionally, this analysis is not sensitive to regional variability.

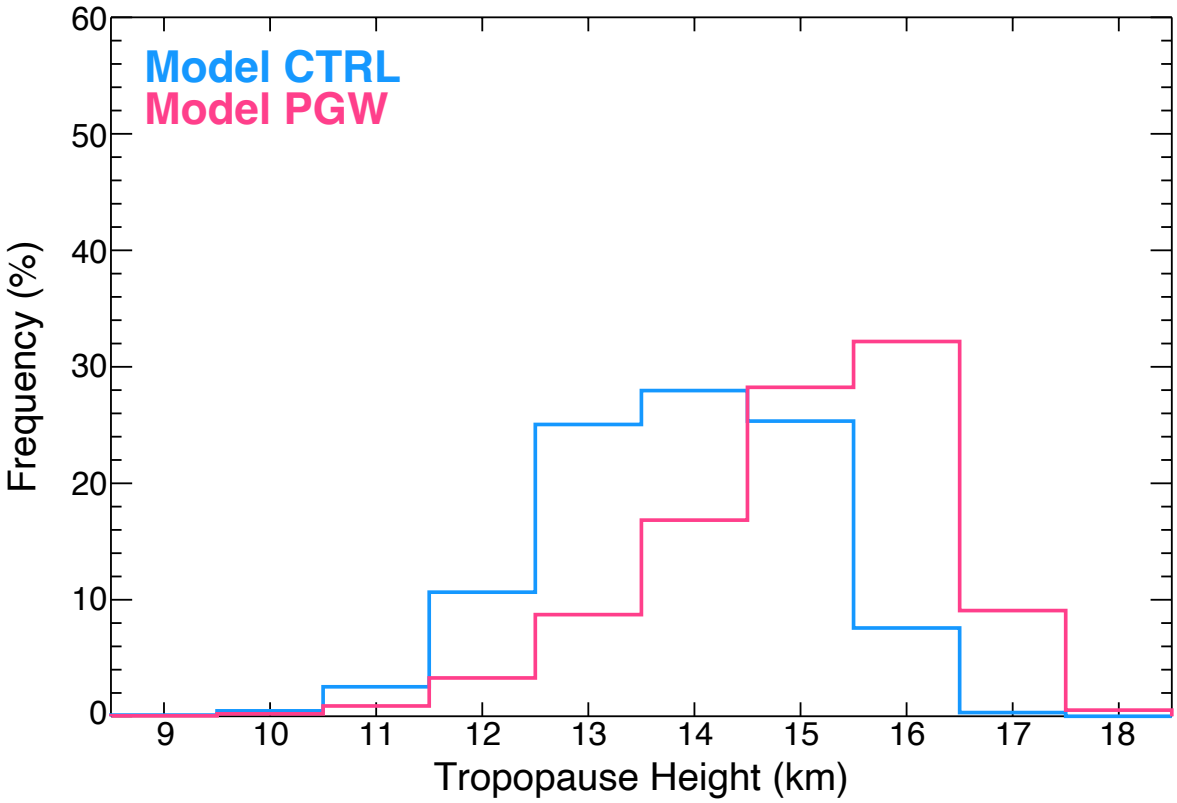

Figure 4.14: Frequency histograms of PTGT altitude during overshooting events for the CTRL experiment (blue) and the PGW experiment (pink), with 1 km bin sizes.

4.4 Discussion

The results presented here represent the first step in unraveling how climate change may impact tropopause-overshooting convection and its associated transport in the future. This analysis clearly demonstrates that there is a potential for significant increases in the frequency and depth of tropopause-overshooting convection in the future. This implies that extratropical convection may contribute additional water vapor to the lower stratosphere as the climate warms, indicating that it could be a critical component of the stratospheric water vapor feedback. Therefore, tropopause-overshooting convection should be studied thoroughly in future work regarding climate change and the UTLS.

The PGW method is a unique approach to investigating convective-scale phenomena in climate model output that has a number of inherent advantages and disadvantages. At its core, a PGW approach allows for the modification of state variables like temperature, moisture, and wind speed to reflect a potential future climate state in isolation from changes in large-scale baroclinity. It was therefore possible to investigate the competing environmental changes expected in a warming climate — that is, increasing instability and increasing tropopause altitude — which ultimately showed that the projected thermodynamic changes are largely favorable to tropopause-overshooting convection. However, this means that potential changes to the synoptic-scale environment are not accounted for. For example, even though changes in the frequency, strength, and storm track location of extratropical cyclones are likely in a warming climate (Arias et al. 2021) and are important for the forcing of widespread deep convection, the PGW method prevents this from influencing the model simulation. This likely contributes to some of the contrasting results of this study with previous work

focused on severe weather, which indicate that spring and early summer are more favorable for severe weather in a warming climate (e.g., Hoogewind et al. 2017; Gensini and Mote 2015), as opposed to the results presented here which show a frequency increase of deep convection in late summer (Figs. 4.7 and 4.9). Additionally, the PGW method prevents interannual variability in tropopause-overshooting convection from being evaluated, though Gensini (2021) reports that a substantial increase in the variability of severe weather may be associated with a warming climate.

Model simulations of tropopause-overshooting convection and its transport are sensitive to both the model resolution and the choice of microphysics parameterization (Phoenix et al. 2017; Homeyer 2015). Both the horizontal and the vertical resolution of the model can impact the representation of convection, the tropopause, and overshoot characteristics. Fortunately, the combination of 4 km horizontal grid spacing and 500–600 m vertical grid spacing used here has been shown to produce unbiased cloud top heights (Homeyer 2015). I attempt to account for the uncertainty in the model simulation through validation with radar and satellite observations, though limitations of current observational capabilities serve as obstacles to comprehensive comparison between the model, GridRad, and GOES. Despite these model sensitivities and validation challenges, the ability of the model to accurately represent the distribution, annual cycle, and diurnal cycle of tropopause-overshooting convection across the entire model domain is encouraging. It should also be emphasized that the CMIP5 model climate forcing used in this study represents a worst-case, RCP 8.5 emissions scenario. Therefore, the amplification of tropopause-overshooting convection may be exaggerated in comparison to a more moderate warming scenario. Additional work using various warming scenarios could help to identify the sensitivity of tropopause-overshooting convection to these changes and to better estimate the range of possible outcomes.

Finally, it is important to acknowledge that projected changes in the frequency of tropopause-overshooting convection is just one piece of a much larger puzzle. Changes to the climate system may also impact the efficiency of transport mechanisms associated with convection. For example, above anvil cirrus plumes have been shown to substantially impact the transport of water vapor and boundary layer air into the lower stratosphere during tropopause-overshooting convection (Gordon and Homeyer 2022; O'Neill et al. 2021; Homeyer et al. 2017). Above anvil cirrus plume production is largely controlled by lower stratospheric storm-relative winds (e.g., Homeyer et al. 2017), which may be altered in a warming climate. Furthermore, climate-driven changes in UTLS temperature and stability could serve as additional thermodynamic constraints on water vapor transport (Solomon et al. 2016; Homeyer et al. 2014). Additionally, it is not clear in the present study whether the increase in tropopause-overshooting convection is a result of an increase in the total amount of deep convection or an increase in the proportion of deep convection that is able to overshoot the tropopause, or both.

Chapter 5

Summary and Conclusions

5.1 Summary of Findings

5.1.1 Lowermost Stratosphere Water Vapor Extrema

MLS observations from 2005–2020 were used in conjunction with MERRA-2 reanalysis data to create a climatology of H_2O extrema (>8 ppmv) in the stratospheric overworld and in the total LS (overworld + LMS). This study showed that the frequency and distribution of H_2O extrema in the total LS (0.27% of MLS total LS observations globally) are dramatically different from that of the stratospheric overworld (0.08% of MLS overworld observations globally), revealing that the frequency of LS extrema increases by more than 300% when the LMS is included in the analysis. On both a yearly and seasonal basis, the frequency of extrema in the total LS analysis is substantially greater than that of the stratospheric overworld, but the magnitude of the difference varies by region (Figs. 2.1 and 2.2).

To provide additional context for this climatology, a statistical transport analysis was conducted by initializing isentropic trajectories at the latitude, longitude, and θ of H_2O extrema (Figs. 2.3–2.5, 2.7–2.11). The transport analysis reveals two main transport patterns: (1) air being traced to or confined within monsoon circulations (i.e. the CEA, SC, NA, and GC regions; Figs. 2.3, 2.5, 2.7, and 2.9) and (2) largely zonal transport along the tropopause break via subtropical jet streams (the NP, NA, SA,

SP, and SI regions; Figs. 2.4, 2.7, 2.8, 2.10, and 2.11). For all regions, the large-scale transport pathways indicate that the extrema air can be traced to regions of relatively frequent tropopause-overshooting convection. This analysis also reveals that, outside of monsoon-related circulations, meridional transport from the tropics to the observed H_2O extrema is infrequent. To further investigate the potential origins of H_2O extrema, the cross-tropopause nature of the isentropic trajectories was also investigated using the percentage of trajectories with recent history within the troposphere as a proxy for large-scale isentropic TST (Fig. 2.6). The percentage of trajectories classified as being related to large-scale TST is regionally dependent, notably showing low occurrences of large-scale TST over the NP, NA, and GC regions — providing further evidence of convection serving as the major source of H_2O extrema in those regions. In regions where large-scale TST is more frequent, it remains unknown whether convection upstream is coupled to such extrema. Namely, moist air that is transported isentropically to the LS may be related to upstream convective sources that acted to hydrate the upper troposphere prior to the large-scale TST.

Finally, the annual cycles of extrema frequency were investigated for regions encompassing AMA, NAMA, and SAMA (Fig. 2.12). The LS frequency of H_2O extrema in the AMA and NAMA regions was shown to be an order of magnitude larger than that of the SAMA. Additionally, while the AMA and NAMA have similar overworld extrema frequencies throughout the annual cycle, the magnitude and duration of peak extrema frequencies for NAMA increases substantially with the inclusion of the LMS in the total LS analysis, compared to a small increase for AMA. The results presented above highlight the importance of the including the LMS in analyses of LS composition. The frequency, geographic extent, and longevity of extrema are all substantially larger in the total LS analysis compared to the overworld only analysis. Additionally, the transport analysis strongly suggests that convection is a substantial contributor to

the occurrence of LS H_2O extrema, which may not have been clear if conducted for the overworld only.

5.1.2 The Potential Temperature Gradient Tropopause

This study examined long-term records of balloon-based observations of atmospheric temperature and composition to revisit stability-based definition of the tropopause. More than 7000 O_3 and temperature profiles observed in tropical, extratropical, and polar locations spanning all seasons and multiple decades were used to investigate composition-stability relationships near the tropopause (Figs. 3.1, 3.2, and 3.3). By analyzing coincident observations of O_3 concentrations and various stability metrics in both individual ozonesonde profiles (Fig. 3.4) as well as a statistical analysis of all observations (Fig. 3.5), it was shown that the vertical gradient of potential temperature ($\partial\theta/\partial z$) is the most consistent stability-based discriminator for the sharp composition change between troposphere and stratosphere in a wide variety of environments when compared to common alternatives such as the temperature lapse rate and Brunt-Väisälä frequency.

Based on the identified superiority of $\partial\theta/\partial z$ as a globally-consistent stability-based indicator of the tropopause transition layer, identification of a tropopause level via a PTGT definition is desired. Modeled after the LRT, the PTGT definition simply requires a potential temperature gradient threshold to be met across multiple depths. This PTGT algorithm offers a new globally- and universally-applicable stability-based tropopause definition for future UTLS studies and serves as an alternative to the LRT. Through comparison of PTGT and LRT altitudes in observations (Figs. 3.7 and 3.8) and reanalysis model output (Figs. 3.14 and 3.16), as well as the examination of PTGT- and LRT-relative O_3 concentrations (Figs. 3.9 and 3.10) and their locations in O_3–H_2O tracer–tracer space (Fig. 3.11), it was demonstrated that the PTGT resolves known

limitations of the LRT. Moreover, though the PTGT is often found within ∼1 km of the LRT (Fig. 3.8), when it differs greatly from the LRT it is more consistent in identifying the layer of greatest composition change in the UTLS, favoring the tropospheric end-point of the chemical mixing layer. Instances of the PTGT differing greatly from the LRT are most often negative, with the PTGT well below the LRT altitude. This result from a composition-informed stability-based tropopause definition (i.e., the PTGT) is consistent with findings in past studies using an ozone tropopause (e.g., Bethan et al. 1996).

Criteria for multiple tropopause identification using the potential temperature gradient were also included in the PTGT definition proposed here and modeled after the LRT —the only alternative definition that includes criteria for multiple tropopause identification. Instances of double tropopauses (DTs) were evaluated using the PTGT definition and compared to the LRT definition, as done for the primary tropopause altitude. It was demonstrated that 1) fewer double tropopauses are identified by the PTGT definition (Table 2 and Fig. 3.15), 2) when both the LRT and PTGT identify a DT, they are in close agreement (Fig. 3.13), and 3) cases where only the PTGT identifies a double tropopause are largely those where the primary PTGT falls well below the LRT, such that the LRT altitude closely coincides with the secondary PTGT.

The introduction of a new universal stability-based tropopause definition motivates revisiting past work built upon the LRT definition. In particular, future work with the PTGT should be dedicated toward important UTLS topics such as stratosphere–troposphere exchange, tropopause climatology, and long-term tropopause variability and change.

5.1.3 Overshooting Convection in a Warming Climate

In this study, the PGW method was employed to analyze the response of extratropical tropopause-overshooting convection to a changing climate for the first time. Investigation of 10-year periods of two downscaled WRF simulations — a control simulation (CTRL) and a future simulation (PGW) — showed more than a doubling of tropopause-overshooting convection over North America in response to projected climate change.

The model CTRL simulation was evaluated against radar (GridRad) and satellite (GOES) observations and was shown to effectively simulate the observed regional distribution, annual cycle, and diurnal cycle of tropopause-overshooting convection (Figs. 4.1–4.3, 4.5, 4.6). The projected changes between the CTRL and PGW simulations were then evaluated and found to be a more than 250% increase across the model domain (Fig. 4.4). The projected seasonal period of frequent tropopause-overshooting convection was shown to extend into late-summer, due to the combined impacts of changes over the Sierra Madre, Gulf Coast, and Southern Plains (Figs. 4.7, 4.9). Diurnally, an increase in the relative frequency of tropopause-overshooting convection occuring overnight and in the early morning hours across the domain was found (Figs. 4.8, 4.10).

The model representation of future tropopause height was also examined and projected increases on the order of $\sim$0.5 km across the domain during all seasons (Fig. 4.11). Though a high tropopause altitude can hinder the ability of convection to overshoot the tropopause, the model simulated convection was able to regularly overshoot higher tropopause heights in the PGW simulation (Fig. 4.14). Finally, the depth of the overshoots were evaluated and showed that overshoots of extreme tropopause-relative heights ($>$ 4 km) are more likely to occur in a warming climate (Figs. 4.12, 4.13).

The PGW method allowed for an in-depth analysis of the response of extratropical tropopause-overshooting convection to prescribed changes associated with projected global warming. This work demonstrates that tropopause-overshooting convection has the potential to become more frequent and intense in a warming climate and motivates future analysis using a multitude of approaches to holistically address this problem. Specifically, it is important to discern how additional factors that may influence the occurrence of tropopause-overshooting convection (i.e., baroclinity), or its efficiency in facilitating stratosphere-troposphere exchange (i.e., UTLS characteristics) may change in a warming climate.

5.2 Looking Forward

The major takeaway from the work presented in this dissertation can be summarized as this: tropopause-overshooting convection is an important contributor to stratospheric water vapor in the present, and it may become even more critical in the future. The lowermost stratosphere specifically is a region that has been understudied and is especially susceptible to impacts from tropopause-overshooting convection. Though it is dynamically complex and challenging to define in practice, Chapter 2 clearly demonstrates that the lowermost stratosphere is an important component of the UTLS that can not be ignored when conducting analysis on the lower stratosphere — as doing so has historically led to the underestimation of the importance of tropopause-overshooting convection in the midlatitudes. Improvements to our definition and understanding of the tropopause — like the potential temperature gradient tropopause presented in Chapter 3 — will be vital to ameliorate some of these challenges. Finally, the results presented in Chapter 4 regarding the response of tropopause-overshooting convection

to a changing climate represent only the first step in tackling this problem. The potential contribution that this poses to the stratospheric water vapor feedback motivates substantial work on this topic in the coming years.

Reference List

Añel, J. A., J. C. Antuña, L. de la Torre, J. M. Castanheira, and L. Gimeno, 2008: Climatological features of global multiple tropopause events. *J. Geophys. Res.*, **133**, D00B08, https://doi.org/10.1029/2007JD009697.

Arias, P., and Coauthors, 2021: *Climate Change 2021: The Physical Science Basis. Contribution of Working Group I to the Sixth Assessment Report of the Intergovernmental Panel on Climate Change*, 33144. Cambridge University Press, Cambridge, United Kingdom and New York, NY, USA, https://doi.org/10.1017/9781009157896.002.

Banerjee, A., G. Chiodo, M. Previdi, M. Ponater, A. J. Conley, and L. M. Polvani, 2019: Stratospheric water vapor: an important climate feedback. *Climate Dynamics*, **53**, 1697–1710, https://doi.org/10.1007/s00382-019-04721-4.

Bedka, K. M., J. Brunner, R. Dworak, W. Feltz, J. Otkin, and T. Greenwald, 2010: Objective satellite-based detection of overshooting tops using infrared window channel brightness temperature gradients. *Journal of Applied Meteorology and Climatology - J APPL METEOROL CLIMATOL*, **49**, 181–202, https://doi.org/10.1175/2009JAMC2286.1.

Bedka, K. M., E. M. Murillo, C. R. Homeyer, B. Scarino, and H. Mersiovsky, 2018: The above-anvil cirrus plume: An important severe weather indicator in visible and infrared satellite imagery. *Weather and Forecasting*, **33 (5)**, 1159 – 1181, https://doi.org/10.1175/WAF-D-18-0040.1.

Bergman, J. W., F. Fierli, E. J. Jensen, S. Honomichl, and L. L. Pan, 2013: Boundary layer sources for the asian anticyclone: Regional contributions to a vertical conduit. *Journal of Geophysical Research: Atmospheres*, **118 (6)**, 2560–2575, https://doi.org/https://doi.org/10.1002/jgrd.50142, URL https://agupubs.onlinelibrary.wiley.com/doi/abs/10.1002/jgrd.50142, https://agupubs.onlinelibrary.wiley.com/doi/pdf/10.1002/jgrd.50142.

Berthet, G., J. G. Esler, and P. H. Haynes, 2007: A Lagrangian perspective of the tropopause and the ventilation of the lowermost stratosphere. *J. Geophys. Res.*, **112**, D18 102, https://doi.org/10.1029/2006JD008295.

Bethan, S., G. Vaughan, and S. J. Reid, 1996: A comparison of ozone and thermal tropopause heights and the impact of tropopause definition on quantifying the ozone content of the troposphere. *Q. J. R. Meteorol. Soc.*, **122**, 929–944.

Birner, T., 2006: Fine-scale structure of the extratropical tropopause. *J. Geophys. Res.*, **111**, D04 104, https://doi.org/10.1029/2005JD006301.

Bowman, K. P., 1993: Large-scale isentropic mixing properties of the antarctic polar vortex from analyzed winds. *Journal of Geophysical Research: Atmospheres*, **98 (D12)**, 23 013–23 027, https://doi.org/10.1029/93JD02599.

Bowman, K. P., and G. D. Carrie, 2002: The mean-meridional transport circulation of the troposphere in an idealized gcm. *Journal of the Atmospheric Sciences*, **59 (9)**, 1502–1514, https://doi.org/10.1175/1520-0469(2002)059⟨1502:TMMTCO⟩2.0.CO;2.

Bowman, K. P., J. Lin, A. Stohl, R. Draxler, P. Konopka, A. Andrews, and D. Brunner, 2013: Input data requirements lagrangian trajectory models. *Bulletin of the American Meteorological Society*, **94**, 1051–1058, https://doi.org/10.1175/BAMS-D-12-00076.1.

Brogli, R., C. Heim, J. Mensch, S. L. Sørland, and C. Schär, 2023: The pseudo-global-warming (pgw) approach: methodology, software package pgw4era5 v1.1, validation, and sensitivity analyses. *Geoscientific Model Development*, **16 (3)**, 907–926, https://doi.org/10.5194/gmd-16-907-2023, URL https://gmd.copernicus.org/articles/16/907/2023/.

Brooks, H., J. W Lee, and J. P Craven, 2003: The spatial distribution of severe thunderstorm and tornado environments from global reanalysis data. *Atmospheric Research*, **67-68**, 73–94, https://doi.org/10.1016/S0169-8095(03)00045-0.

Browell, E. V., E. F. Danielsen, S. Ismail, G. L. Gregory, and S. M. Beck, 1987: Tropopause fold structure determined from airborne lidar in situ measurements. *J. Geophys. Res.*, **92 (D2)**, 2112–2120.

Carroll-Smith, D., R. J. Trapp, and J. M. Done, 2021: Exploring inland tropical cyclone rainfall and tornadoes under future climate conditions through a case study of hurricane ivan. *Journal of Applied Meteorology and Climatology*, **60 (1)**, 103 – 118, https://doi.org/https://doi.org/10.1175/JAMC-D-20-0090.1, URL https://journals.ametsoc.org/view/journals/apme/60/1/jamc-d-20-0090.1.xml.

Castanheira, J. M., J. A. Añel, C. A. F. Marques, J. C. Antuña, M. L. R. Liberato, L. de la Torre, and L. Gimeno, 2009: Increase of upper troposphere/lower stratosphere wave baroclinicity during the second half of the 20th century. *Atmos. Chem. Phys.*, **9 (23)**, 9143–9153.

Castanheira, J. M., and L. Gimeno, 2011: Association of double tropopause events with baroclinic waves. *J. Geophys. Res.*, **116**, D19 113, https://doi.org/10.1029/2011JD016163.

Chang, K.-W., K. P. Bowman, and A. D. Rapp, 2023: Transport and confinement of plumes from tropopause-overshooting convection over the contiguous united states during the warm season. *Journal of Geophysical Research: Atmospheres*, **128 (2)**, e2022JD037 020, https://doi.org/https://doi.org/

10.1029/2022JD037020, URL https://agupubs.onlinelibrary.wiley.com/doi/abs/10.1029/2022JD037020, e2022JD037020 2022JD037020, https://agupubs.onlinelibrary.wiley.com/doi/pdf/10.1029/2022JD037020.

Clapp, C., J. Smith, K. Bedka, and J. Anderson, 2019: Identifying source regions and the distribution of cross-tropopause convective outflow over north america during the warm season. *Journal of Geophysical Research: Atmospheres*, **124 (24)**, 13 750–13 762, https://doi.org/https://doi.org/10.1029/2019JD031382, URL https://agupubs.onlinelibrary.wiley.com/doi/abs/10.1029/2019JD031382, https://agupubs.onlinelibrary.wiley.com/doi/pdf/10.1029/2019JD031382.

Clapp, C. E., J. B. Smith, K. M. Bedka, and J. G. Anderson, 2021: Identifying outflow regions of north american monsoon anticyclone-mediated meridional transport of convectively influenced air masses in the lower stratosphere. *Journal of Geophysical Research: Atmospheres*, **126 (10)**, e2021JD034 644, https://doi.org/https://doi.org/10.1029/2021JD034644, URL https://agupubs.onlinelibrary.wiley.com/doi/abs/10.1029/2021JD034644, e2021JD034644 2021JD034644, https://agupubs.onlinelibrary.wiley.com/doi/pdf/10.1029/2021JD034644.

Cooney, J. W., K. M. Bedka, K. P. Bowman, K. V. Khlopenkov, and K. Itterly, 2021: Comparing tropopause-penetrating convection identifications derived from nexrad and goes over the contiguous united states. *Journal of Geophysical Research: Atmospheres*, **126 (14)**, e2020JD034 319, https://doi.org/https://doi.org/10.1029/2020JD034319, URL https://agupubs.onlinelibrary.wiley.com/doi/abs/10.1029/2020JD034319, e2020JD034319 2020JD034319, https://agupubs.onlinelibrary.wiley.com/doi/pdf/10.1029/2020JD034319.

Cooney, J. W., K. P. Bowman, C. R. Homeyer, and T. M. Fenske, 2018: Ten year analysis of tropopause-overshooting convection using gridrad data. *Journal of Geophysical Research: Atmospheres*, **123 (1)**, 329–343, https://doi.org/10.1002/2017JD027718.

Crum, T. D., and R. L. Alberty, 1993: The wsr-88d and the wsr-88d operational support facility. *Bull. Amer. Meteor. Soc.*, **74 (9)**, 1669–1688, https://doi.org/10.1175/1520-0477(1993)074⟨1669:TWATWO⟩2.0.CO;2.

Danielsen, E. F., 1959: The laminar structure of the atmosphere and its relation to the concept of a tropopause. *Arch. Meteorol. Geophys. Bioklimatol., Ser. A*, **11**, 293–332.

Danielsen, E. F., 1968: Stratospheric-tropospheric exchange based on radioactivity, ozone and potential vorticity. *J. Atmos. Sci.*, **25**, 502–518.

Dauhut, T., and C. Hohenegger, 2022: The contribution of convection to the stratospheric water vapor: The first budget using a global storm-resolving model. *Journal of Geophysical Research: Atmospheres*, **127 (5)**, e2021JD036 295, https://doi.org/https://doi.org/10.1029/2021JD036295, URL https://agupubs.onlinelibrary.wiley.

com/doi/abs/10.1029/2021JD036295, e2021JD036295 2021JD036295, https://agupubs.onlinelibrary.wiley.com/doi/pdf/10.1029/2021JD036295.

Dee, D. P., and Coauthors, 2011: The era-interim reanalysis: configuration and performance of the data assimilation system. *Quarterly Journal of the Royal Meteorological Society*, **137 (656)**, 553–597, https://doi.org/10.1002/qj.828.

Dessler, A. E., M. R. Schoeberl, T. Wang, S. M. Davis, and K. H. Rosenlof, 2013: Stratospheric water vapor feedback. *Proceedings of the National Academy of Sciences*, **110 (45)**, 18 087–18 091, https://doi.org/10.1073/pnas.1310344110, URL https://www.pnas.org/doi/abs/10.1073/pnas.1310344110, https://www.pnas.org/doi/pdf/10.1073/pnas.1310344110.

Dessler, A. E., and S. C. Sherwood, 2004: Effect of convection on the summertime extratropical lower stratosphere. *Journal of Geophysical Research: Atmospheres*, **109 (D23)**, https://doi.org/10.1029/2004JD005209.

Diffenbaugh, N., M. Scherer, and J. R. Trapp, 2013: Robust increases in severe thunderstorm environments in response to greenhouse forcing. *Proceedings of the National Academy of Sciences of the United States of America*, **110**, 16 361–16 366, https://doi.org/10.1073/pnas.1307758110.

Duran, P., and J. Molinari, 2019: Tropopause evolution in a rapidly intensifying tropical cyclone: A static stability budget analysis in an idealized axisymmetric framework. *Journal of the Atmospheric Sciences*, **76 (1)**, 209–229.

Fischer, H., and Coauthors, 2000: Tracer correlations in the northern high latitude lowermost stratosphere: Influence of cross-tropopause mass exchange. *Geophys. Res. Lett.*, **27 (1)**, 97–100.

Gelaro, R., and Coauthors, 2017: The Modern-Era Retrospective Analysis for Research and Applications, Version 2 (MERRA-2). *J. Clim.*, **30**, 5419–5454, https://doi.org/10.1175/JCLI-D-16-0758.1.

Gensini, V., and T. Mote, 2014: Estimations of hazardous convective weather in the united states using dynamical downscaling. *Journal of Climate*, **27**, 6581–6589, https://doi.org/10.1175/JCLI-D-13-00777.1.

Gensini, V., and T. Mote, 2015: Downscaled estimates of late 21st century severe weather from ccsm3. *Climatic Change*, **129**, https://doi.org/10.1007/s10584-014-1320-z.

Gensini, V. V. A., 2021: Chapter 4 - severe convective storms in a changing climate. *Climate Change and Extreme Events*, A. Fares, Ed., Elsevier, 39–56, https://doi.org/https://doi.org/10.1016/B978-0-12-822700-8.00007-X, URL https://www.sciencedirect.com/science/article/pii/B978012822700800007X.

Gettelman, A., P. Hoor, L. L. Pan, W. J. Randel, M. I. Hegglin, and T. Birner, 2011: The extratropical upper troposphere and lower stratosphere. *Rev. Geophys.*, **49**, RG3003, https://doi.org/10.1029/2011RG000355.

Gettelman, A., and T. Wang, 2015: Structural diagnostics of the tropopause inversion layer and its evolution. *J. Geophys. Res. Atmos.*, **120**, 46–62, https://doi.org/10.1002/2014JD021846.

Gordon, A. E., and C. R. Homeyer, 2022: Sensitivities of cross-tropopause transport in midlatitude overshooting convection to the lower stratosphere environment. *Journal of Geophysical Research: Atmospheres*, **127 (13)**, e2022JD036 713, https://doi.org/https://doi.org/10.1029/2022JD036713, URL https://agupubs.onlinelibrary.wiley.com/doi/abs/10.1029/2022JD036713, e2022JD036713 2022JD036713, https://agupubs.onlinelibrary.wiley.com/doi/pdf/10.1029/2022JD036713.

Hall, E. G., A. F. Jordan, D. F. Hurst, S. J. Oltmans, H. Vömel, B. Kühnreich, and V. Ebert, 2016: Advancements, measurement uncertainties and recent comparisons of the NOAA frost point hygrometer. *Atmos. Meas. Tech.*, **9**, 4295–4310, https://doi.org/10.5194/amt-9-4295-2016.

Hanisco, T. F., and Coauthors, 2007: Observations of deep convective influence on stratospheric water vapor and its isotopic composition. *Geophysical Research Letters*, **34 (4)**, https://doi.org/10.1029/2006GL027899.

Hegglin, M. I., C. D. Boone, G. L. Manney, and K. A. Walker, 2009: A global view of the extratropical tropopause transition layer from atmospheric chemistry experiment fourier transform spectrometer o-3, h2o, and co. *J. Geophys. Res.*, **114**, D00B11, https://doi.org/10.1029/2008JD009984.

Hegglin, M. I., and Coauthors, 2004: Tracing troposphere-to-stratosphere transport above a mid-latitude deep convective system. *Atmospheric Chemistry and Physics*, **4 (3)**, 741–756, https://doi.org/10.5194/acp-4-741-2004.

Herman, R. L., and Coauthors, 2017: Enhanced stratospheric water vapor over the summertime continental United States and the role of overshooting convection. *Atmos. Chem. Phys.*, **17**, 6113–6124, https://doi.org/10.5194/acp-17-6113-2017.

Hersbach, H., and Coauthors, 2020: The era5 global reanalysis. *Quarterly Journal of the Royal Meteorological Society*, **146 (730)**, 1999–2049, https://doi.org/https://doi.org/10.1002/qj.3803, URL https://rmets.onlinelibrary.wiley.com/doi/abs/10.1002/qj.3803, https://rmets.onlinelibrary.wiley.com/doi/pdf/10.1002/qj.3803.

Highwood, E. J., and B. J. Hoskins, 1998: The tropical tropopause. *Quarterly Journal of the Royal Meteorological Society*, **124 (549)**, 1579–1604, https://doi.org/https://doi.org/10.1002/qj.49712454911.

Hoerling, M. P., T. K. Schaack, and A. J. Lenzen, 1991: Global objective tropopause analysis. *Mon. Wea. Rev.*, **119**, 1816–1831.

Hoffmann, L., and R. Spang, 2022: An assessment of tropopause characteristics of the ERA5 and ERA-Interim meteorological reanalyses. *Atmos. Chem. Phys.*, **22**, 4019–4046, https://doi.org/10.5194/acp-22-4019-2022.

Hoinka, K. P., 1997: The tropopause: discovery, definition and demarcation. *Meteorol. Z.*, **6**, 281–303.

Holton, J. R., P. H. Haynes, M. E. McIntyre, A. R. Douglass, and L. Pfister, 1995: Stratosphere-troposphere exchange. *Rev. Geophys.*, **33 (4)**, 403–439.

Homeyer, C. R., 2015: Numerical simulations of extratropical tropopause-penetrating convection: Sensitivities to grid resolution. *J. Geophys. Res. Atmos.*, **120**, 7174–7188, https://doi.org/10.1002/2015JD023356.

Homeyer, C. R., and K. P. Bowman, 2013: Rossby wave breaking and transport between the tropics and extratropics above the subtropical jet. *Journal of the Atmospheric Sciences*, **70 (2)**, 607–626, https://doi.org/10.1175/JAS-D-12-0198.1.

Homeyer, C. R., and K. P. Bowman, 2017: Algorithm Description Document for Version 3.1 of the Three-Dimensional Gridded NEXRAD WSR-88D Radar (GridRad) Dataset. Available online at: http://gridrad.org/pdf/GridRad-v3.1-Algorithm-Description.pdf.

Homeyer, C. R., and K. P. Bowman, 2021: A 22-year evaluation of convection reaching the stratosphere over the united states. *Journal of Geophysical Research: Atmospheres*, **126 (13)**, e2021JD034 808, https://doi.org/https://doi.org/10.1029/2021JD034808, URL https://agupubs.onlinelibrary.wiley.com/doi/abs/10.1029/2021JD034808, e2021JD034808 2021JD034808, https://agupubs.onlinelibrary.wiley.com/doi/pdf/10.1029/2021JD034808.

Homeyer, C. R., K. P. Bowman, and L. L. Pan, 2010: Extratropical tropopause transition layer characteristics from high-resolution sounding data. *J. Geophys. Res.*, **115**, D13 108, https://doi.org/10.1029/2009JD013664.

Homeyer, C. R., K. P. Bowman, L. L. Pan, E. L. Atlas, R.-S. Gao, and T. L. Campos, 2011: Dynamical and chemical characteristics of tropospheric intrusions observed during start08. *Journal of Geophysical Research: Atmospheres*, **116 (D6)**, https://doi.org/https://doi.org/10.1029/2010JD015098.

Homeyer, C. R., J. D. McAuliffe, and K. M. Bedka, 2017: On the development of above-anvil cirrus plumes in extratropical convection. *Journal of the Atmospheric Sciences*, **74 (5)**, 1617–1633, https://doi.org/10.1175/JAS-D-16-0269.1.

Homeyer, C. R., and Coauthors, 2014: Convective transport of water vapor into the lower stratosphere observed during double-tropopause events. *Journal of Geophysical Research: Atmospheres*, **119 (18)**, 10,941–10,958, https://doi.org/10.1002/2014JD021485.

Homeyer, C. R., and Coauthors, 2023: Extreme altitudes of stratospheric hydration by midlatitude convection observed during the dcotss field campaign. *Geophysical Research Letters*, **50 (18)**, e2023GL104 914, https://doi.org/https://doi.org/10.1029/2023GL104914, URL https://agupubs.onlinelibrary.wiley.com/doi/abs/10.1029/2023GL104914, e2023GL104914 2023GL104914, https://agupubs.onlinelibrary.wiley.com/doi/pdf/10.1029/2023GL104914.

Honomichl, S. B., and L. L. Pan, 2020: Transport from the asian summer monsoon anticyclone over the western pacific. *Journal of Geophysical Research: Atmospheres*, **125 (13)**, e2019JD032 094, https://doi.org/https://doi.org/10.1029/2019JD032094, URL https://agupubs.onlinelibrary.wiley.com/doi/abs/10.1029/2019JD032094, e2019JD032094 2019JD032094, https://agupubs.onlinelibrary.wiley.com/doi/pdf/10.1029/2019JD032094.

Hoogewind, K. A., M. E. Baldwin, and R. J. Trapp, 2017: The impact of climate change on hazardous convective weather in the united states: Insight from high-resolution dynamical downscaling. *Journal of Climate*, **30 (24)**, 10 081–10 100, https://doi.org/10.1175/JCLI-D-16-0885.1.

Hoor, P., H. Fischer, L. Lange, J. Lelieveld, and D. Brunner, 2002: Seasonal variations of a mixing layer in the lowermost stratosphere as identified by the CO-O3 correlation from in situ measurements. *J. Geophys. Res.*, **107 (D5)**, 4044, https://doi.org/10.1029/2000JD000289.

Hoskins, B. J., 1991: Towards a pv- view of the general circulation. *Tellus B*, **43 (4)**, 27–35, https://doi.org/https://doi.org/10.1034/j.1600-0889.1991.t01-3-00005.x, URL https://onlinelibrary.wiley.com/doi/abs/10.1034/j.1600-0889.1991.t01-3-00005.x, https://onlinelibrary.wiley.com/doi/pdf/10.1034/j.1600-0889.1991.t01-3-00005.x.

Hou, A. Y., and Coauthors, 2014: The global precipitation measurement mission. *Bulletin of the American Meteorological Society*, **95 (5)**, 701 – 722, https://doi.org/https://doi.org/10.1175/BAMS-D-13-00164.1, URL https://journals.ametsoc.org/view/journals/bams/95/5/bams-d-13-00164.1.xml.

Hurst, D. F., S. J. Oltmans, H. Vömel, K. H. Rosenlof, S. M. Davis, E. A. Ray, E. G. Hall, and A. F. Jordan, 2011: Stratospheric water vapor trends over boulder, colorado: Analysis of the 30 year boulder record. *J. Geophys. Res.*, **116 (D2)**, https://doi.org/https://doi.org/10.1029/2010JD015065.

Jensen, E. J., and Coauthors, 2020: Assessment of observational evidence for direct convective hydration of the lower stratosphere. *Journal of Geophysical Research: Atmospheres*, **125 (15)**, e2020JD032 793, https://doi.org/10.1029/2020JD032793.

Khaykin, S. M., and Coauthors, 2022: Persistence of moist plumes from overshooting convection in the asian monsoon anticyclone. *Atmospheric Chemistry and Physics*, **22 (5)**, 3169–3189, https://doi.org/10.5194/acp-22-3169-2022, URL https://acp.copernicus.org/articles/22/3169/2022/.

Khlopenkov, K. V., K. M. Bedka, J. W. Cooney, and K. Itterly, 2021: Recent advances in detection of overshooting cloud tops from longwave infrared satellite imagery. *Journal of Geophysical Research: Atmospheres*, **126 (14)**, e2020JD034 359, https://doi.org/https://doi.org/10.1029/2020JD034359, URL https://agupubs.onlinelibrary.wiley.com/doi/abs/10.1029/2020JD034359, e2020JD034359 2020JD034359, https://agupubs.onlinelibrary.wiley.com/doi/pdf/10.1029/2020JD034359.

Kim, J.-E., and M. J. Alexander, 2015: Direct impacts of waves on tropical cold point tropopause structure. *Geophys. Res. Lett.*, **42**, 1584–1592, https://doi.org/10.1002/2014GL062737.

Kochanski, A., 1955: Cross sections of the mean zonal flow and temperature along 80°w. *J. Meteor.*, **12**, 95–106.

Konopka, P., J.-U. Grooß, G. Günther, F. Ploeger, R. Pommrich, R. Müller, and N. Livesey, 2010: Annual cycle of ozone at and above the tropical tropopause: observations versus simulations with the chemical lagrangian model of the stratosphere (clams). *Atmospheric Chemistry and Physics*, **10 (1)**, 121–132, https://doi.org/10.5194/acp-10-121-2010, URL https://acp.copernicus.org/articles/10/121/2010/.

Konopka, P., and L. L. Pan, 2012: On the mixing-driven formation of the Extratropical Transition Layer (ExTL). *J. Geophys. Res.*, **117**, D18 301, https://doi.org/10.1029/2012JD017876.

Konopka, P., M. Tao, F. Ploeger, D. F. Hurst, M. L. Santee, J. S. Wright, and M. Riese, 2022: Stratospheric moistening after 2000. *Geophysical Research Letters*, **49 (8)**, e2021GL097 609, https://doi.org/https://doi.org/10.1029/2021GL097609, URL https://agupubs.onlinelibrary.wiley.com/doi/abs/10.1029/2021GL097609, e2021GL097609 2021GL097609, https://agupubs.onlinelibrary.wiley.com/doi/pdf/10.1029/2021GL097609.

Kunz, A., P. Konopka, R. Müller, and L. L. Pan, 2011: Dynamical tropopause based on isentropic potential vorticity gradients. *J. Geophys. Res.*, **116**, D01 110, https://doi.org/10.1029/2010JD014343.

Langille, J., A. Bourassa, L. L. Pan, D. Letros, B. Solheim, D. Zawada, and D. Degenstein, 2020: Observational evidence of moistening the lowermost stratosphere via isentropic mixing across the subtropical jet. *Atmospheric Chemistry and Physics*, **20 (9)**, 5477–5486, https://doi.org/10.5194/acp-20-5477-2020, URL https://acp.copernicus.org/articles/20/5477/2020/.

Lasher-Trapp, S., S. A. Orendorf, and R. J. Trapp, 2023: Investigating a derecho in a future warmer climate. *Bulletin of the American Meteorological Society*, https://doi.org/https://doi.org/10.1175/BAMS-D-22-0173.1, URL https://journals.ametsoc.org/view/journals/bams/aop/BAMS-D-22-0173.1/BAMS-D-22-0173.1.xml.

Li, F., and P. Newman, 2020: Stratospheric water vapor feedback and its climate impacts in the coupled atmosphere–ocean goddard earth observing system chemistry-climate model. *Climate Dynamics*, **55 (5)**, 1585–1595, https://doi.org/10.1007/s00382-020-05348-6, URL https://doi.org/10.1007/s00382-020-05348-6.

Liu, C., and E. Barnes, 2018: Synoptic formation of double tropopauses. *J. Geophys. Res. Atmos.*, **123**, 693–707, https://doi.org/10.1002/2017JD027941.

Liu, C., and E. J. Zipser, 2005: Global distribution of convection penetrating the tropical tropopause. *Journal of Geophysical Research: Atmospheres*, **110 (D23)**, https://doi.org/10.1029/2005JD006063.

Liu, C., E. J. Zipser, D. J. Cecil, S. W. Nesbitt, and S. Sherwood, 2008: A cloud and precipitation feature database from nine years of trmm observations. *Journal of Applied Meteorology and Climatology*, **47 (10)**, 2712 – 2728, https://doi.org/https://doi.org/10.1175/2008JAMC1890.1, URL https://journals.ametsoc.org/view/journals/apme/47/10/2008jamc1890.1.xml.

Liu, C., and Coauthors, 2017: Continental-scale convection-permitting modeling of the current and future climate of north america. *Climate Dynamics*, **49 (1)**, 71–95, https://doi.org/10.1007/s00382-016-3327-9, URL https://doi.org/10.1007/s00382-016-3327-9.

Liu, N., and C. Liu, 2016: Global distribution of deep convection reaching tropopause in 1year gpm observations. *Journal of Geophysical Research: Atmospheres*, **121 (8)**, 3824–3842, https://doi.org/10.1002/2015JD024430.

Liu, N., C. Liu, and L. Hayden, 2020: Climatology and detection of overshooting convection from 4 years of GPM precipitation radar and passive microwave observations. *J. Geophys. Res. Atmos.*, **125**, e2019JD032 003, https://doi.org/10.1029/2019JD032003.

Livesey, N. J., and Coauthors, 2020: Earth Observing System (EOS) Aura Microwave Limb Sounder (MLS): Version 4.2x Level 2 data quality and description document. Available online at: https://mls.jpl.nasa.gov/data/v4-2_data_quality_document.pdf.

Lorenz, D. J., and E. T. DeWeaver, 2007: Tropopause height and zonal wind response to global warming in the ipcc scenario integrations. *Journal of Geophysical Research: Atmospheres*, **112 (D10)**, https://doi.org/https://doi.org/10.1029/2006JD008087, URL https://agupubs.onlinelibrary.wiley.com/doi/abs/10.1029/2006JD008087, https://agupubs.onlinelibrary.wiley.com/doi/pdf/10.1029/2006JD008087.

Maddox, E. M., and G. L. Mullendore, 2018: Determination of best tropopause definition for convective transport studies. *Journal of the Atmospheric Sciences*, **75 (10)**, 3433–3446, https://doi.org/10.1175/JAS-D-18-0032.1.

Manney, G. L., and Coauthors, 2017: Reanalysis comparisons of upper tropospheric-lower stratospheric jets and multiple tropopauses. *Atmos. Chem. Phys.*, **17**, 11 541–11 566, https://doi.org/10.5194/acp-17-11541-2017.

Meng, L., J. Liu, D. W. Tarasick, W. J. Randel, A. K. Steiner, H. Wilhelmsen, L. Wang, and L. Haimberger, 2021: Continous rise of the tropopause in the Northern Hemisphere over 1980–2020. *Sci. Adv.*, **7**, eabi8065, https://doi.org/10.1126/sciadv.abi8065.

Miloshevich, L. M., A. Paukkunen, H. Vömel, and S. J. Oltmans, 2004: Development and validation of a time-lag correction for vaisala radiosonde humidity measurements. *J. Atmos. Oceanic Technol.*, **21**, 1305–1327.

Mote, P. W., and Coauthors, 1996: An atmospheric tape recorder: The imprint of tropical tropopause temperatures on stratospheric water vapor. *Journal of Geophysical Research: Atmospheres*, **101 (D2)**, 3989–4006, https://doi.org/https://doi.org/10.1029/95JD03422, URL https://agupubs.onlinelibrary.wiley.com/doi/abs/10.1029/95JD03422, https://agupubs.onlinelibrary.wiley.com/doi/pdf/10.1029/95JD03422.

Mullendore, G. L., D. R. Durran, and J. R. Holton, 2005: Cross-tropopause tracer transport in midlatitude convection. *Journal of Geophysical Research: Atmospheres*, **110 (D6)**, https://doi.org/https://doi.org/10.1029/2004JD005059, URL https://agupubs.onlinelibrary.wiley.com/doi/abs/10.1029/2004JD005059, https://agupubs.onlinelibrary.wiley.com/doi/pdf/10.1029/2004JD005059.

Munchak, L. A., and L. L. Pan, 2014: Separation of the lapse rate and the cold point tropopauses in the tropics and the resulting impact on cloud top-tropopause relationships. *Journal of Geophysical Research: Atmospheres*, **119 (13)**, 7963–7978, https://doi.org/https://doi.org/10.1002/2013JD021189, URL https://agupubs.onlinelibrary.wiley.com/doi/abs/10.1002/2013JD021189, https://agupubs.onlinelibrary.wiley.com/doi/pdf/10.1002/2013JD021189.

NASA, 2022a: Costa Rica water vapor and ozonesondes, last accessed january 2022. NASA Network for the Detection of Atmospheric Composition Change, URL https://www-air.larc.nasa.gov/missions/ndacc/data.html.

NASA, 2022b: Southern hemisphere ADitional OZonesondes (SHADOZ), last accessed january 2022. NASA Goddard Space Flight Center, URL https://tropo.gsfc.nasa.gov/shadoz/.

Nesbitt, S. W., E. J. Zipser, and D. J. Cecil, 2000: A census of precipitation features in the tropics using trmm: Radar, ice scattering, and lightning observations. *Journal of Climate*, **13 (23)**, 4087 – 4106, https://doi.org/https://doi.org/10.1175/1520-0442(2000)013⟨4087:ACOPFI⟩2.0.CO;2, URL https://journals.ametsoc.org/view/journals/clim/13/23/1520-0442_2000_013_4087_acopfi_2.0.co_2.xml.

Newman, P. A., and M. R. Schoeberl, 1995: A reinterpretation of the data from the NASA stratosphere-troposphere exchange project. *Geophys. Res. Lett.*, **22 (18)**, 2501–2504.

NOAA, 2021: Ozone and water vapor sondes, last accessed november 2021. NOAA Earth System Research Laboratories Global Monitoring Laboratory, URL https://gml.noaa.gov/aftp/data/ozwv/.

Nowack, P., and Coauthors, 2023: Response of stratospheric water vapour to warming constrained by satellite observations. *Nature Geoscience*, **16 (7)**, 577–583, https://doi.org/10.1038/s41561-023-01183-6, URL https://doi.org/10.1038/s41561-023-01183-6.

Olsen, M. A., A. R. Douglass, P. A. Newman, J. C. Gille, B. Nardi, V. A. Yudin, D. E. Kinnison, and R. Khosravi, 2008: HIRDLS observations and simulation of a lower stratospheric intrusion of tropical air to high latitudes. *Geophys. Res. Lett.*, **35**, L21 813, https://doi.org/10.1029/2008GL035514.

O'Neill, M. E., L. Orf, G. M. Heymsfield, and K. Halbert, 2021: Hydraulic jump dynamics above supercell thunderstorms. *Science*, **373 (6560)**, 1248–1251, https://doi.org/10.1126/science.abh3857, URL https://www.science.org/doi/abs/10.1126/science.abh3857, https://www.science.org/doi/pdf/10.1126/science.abh3857.

Palmén, E., 1948: On the distribution of temperature and wind in the upper westerlies. *J. Meteorol.*, **5**, 20–27.

Pan, L. L., S. B. Honomichl, T. V. Bui, T. Thornberry, A. Rollins, E. Hintsa, and E. J. Jensen, 2018: Lapse rate or cold point: The tropical tropopause identified by in situ trace gas measurements. *Geophys. Res. Lett.*, **45**, 10,756–10,763, https://doi.org/10.1029/2018GL079573.

Pan, L. L., S. B. Honomichl, D. E. Kinnison, M. Abalos, W. J. Randel, J. W. Bergman, and J. Bian, 2016: Transport of chemical tracers from the boundary layer to stratosphere associated with the dynamics of the asian summer monsoon. *Journal*

of Geophysical Research: Atmospheres, **121 (23)**, 14,159–14,174, https://doi.org/https://doi.org/10.1002/2016JD025616, URL https://agupubs.onlinelibrary.wiley.com/doi/abs/10.1002/2016JD025616, https://agupubs.onlinelibrary.wiley.com/doi/pdf/10.1002/2016JD025616.

Pan, L. L., and L. A. Munchak, 2011: Relationship of cloud top to the tropopause and jet structure from calipso data. *Journal of Geophysical Research: Atmospheres*, **116 (D12)**, https://doi.org/10.1029/2010JD015462.

Pan, L. L., L. C. Paulik, S. B. Honomichl, L. A. Munchak, J. Bian, H. B. Selkirk, and H. Vömel, 2014: Identification of the tropical tropopause transition layer using the ozone-water vapor relationship. *J. Geophys. Res. Atmos.*, **119**, 3586–3599, https://doi.org/10.1002/2013JD020558.

Pan, L. L., W. J. Randel, B. L. Gary, M. J. Mahoney, and E. J. Hintsa, 2004: Definitions and sharpness of the extratropical tropopause: A trace gas perspective. *J. Geophys. Res.*, **109**, D23 103, https://doi.org/10.1029/2004JD004982.

Pan, L. L., and Coauthors, 2009: Tropospheric intrusions associated with the secondary tropopause. *J. Geophys. Res.*, **114**, D10 302, https://doi.org/10.1029/2008JD011374.

Pan, L. L., and Coauthors, 2022: A multimodel investigation of asian summer monsoon utls transport over the western pacific. *Journal of Geophysical Research: Atmospheres*, **127 (24)**, e2022JD037 511, https://doi.org/https://doi.org/10.1029/2022JD037511, URL https://agupubs.onlinelibrary.wiley.com/doi/abs/10.1029/2022JD037511, e2022JD037511 2022JD037511, https://agupubs.onlinelibrary.wiley.com/doi/pdf/10.1029/2022JD037511.

Peevey, T. R., J. C. Gille, C. R. Homeyer, and G. L. Manney, 2014: The double tropopause and its dynamical relationship to the tropopause inversion layer in storm track regions. *J. Geophys. Res. Atmos.*, **119**, 10,194–10,212, https://doi.org/10.1002/2014JD021808.

Peevey, T. R., J. C. Gille, C. E. Randall, and A. Kunz, 2012: Investigation of double tropopause spatial and temporal global variability utilizing High Resolution Dynamics Limb Sounder temperature observations. *J. Geophys. Res.*, **117**, D01 105, https://doi.org/10.1029/2011JD016443.

Phoenix, D. B., and C. R. Homeyer, 2021: Simulated impacts of tropopause-overshooting convection on the chemical composition of the upper troposphere and lower stratosphere. *Journal of Geophysical Research: Atmospheres*, **126 (21)**, e2021JD034 568, https://doi.org/https://doi.org/10.1029/2021JD034568, URL https://agupubs.onlinelibrary.wiley.com/doi/abs/10.1029/2021JD034568, e2021JD034568 2021JD034568, https://agupubs.onlinelibrary.wiley.com/doi/pdf/10.1029/2021JD034568.

Phoenix, D. B., C. R. Homeyer, and M. C. Barth, 2017: Sensitivity of simulated convection-driven stratosphere-troposphere exchange in wrf-chem to the choice of physical and chemical parameterization. *Earth and Space Science*, **4 (8)**, 454–471, https://doi.org/https://doi.org/10.1002/2017EA000287, URL https://agupubs.onlinelibrary.wiley.com/doi/abs/10.1002/2017EA000287, https://agupubs.onlinelibrary.wiley.com/doi/pdf/10.1002/2017EA000287.

Ploeger, F., and Coauthors, 2013: Horizontal water vapor transport in the lower stratosphere from subtropics to high latitudes during boreal summer. *Journal of Geophysical Research: Atmospheres*, **118 (14)**, 8111–8127, https://doi.org/https://doi.org/10.1002/jgrd.50636, URL https://agupubs.onlinelibrary.wiley.com/doi/abs/10.1002/jgrd.50636, https://agupubs.onlinelibrary.wiley.com/doi/pdf/10.1002/jgrd.50636.

Prather, M. J., X. Zhu, Q. Tang, J. Hsu, and J. L. Neu, 2011: An atmospheric chemist in search of the tropopause. *J. Geophys. Res.*, **116**, D04 306, https://doi.org/10.1029/2010JD014939.

Randel, W., and M. Park, 2019: Diagnosing observed stratospheric water vapor relationships to the cold point tropical tropopause. *Journal of Geophysical Research: Atmospheres*, **124 (13)**, 7018–7033, https://doi.org/https://doi.org/10.1029/2019JD030648, URL https://agupubs.onlinelibrary.wiley.com/doi/abs/10.1029/2019JD030648, https://agupubs.onlinelibrary.wiley.com/doi/pdf/10.1029/2019JD030648.

Randel, W. J., E. Moyer, M. Park, E. Jensen, P. Bernath, K. Walker, and C. Boone, 2012: Global variations of hdo and hdo/h2o ratios in the upper troposphere and lower stratosphere derived from ace-fts satellite measurements. *Journal of Geophysical Research: Atmospheres*, **117 (D6)**, https://doi.org/10.1029/2011JD016632.

Randel, W. J., M. Park, L. Emmons, D. Kinnison, P. Bernath, K. A. Walker, C. Boone, and H. Pumphrey, 2010: Asian monsoon transport of pollution to the stratosphere. *Science*, **328 (5978)**, 611–613, https://doi.org/10.1126/science.1182274, URL https://www.science.org/doi/abs/10.1126/science.1182274, https://www.science.org/doi/pdf/10.1126/science.1182274.

Randel, W. J., D. J. Seidel, and L. L. Pan, 2007a: Observational characteristics of double tropopauses. *J. Geophys. Res.*, **112**, D07 309, https://doi.org/10.1029/2006JD007904.

Randel, W. J., F. Wu, and P. Forster, 2007b: The extratropical tropopause inversion layer: Global observations with GPS data, and a radiative forcing mechanism. *J. Atmos. Sci.*, **64**, 4489–4496.

Rasmussen, R., and C. Liu, 2017: High resolution wrf simulations of the current and future climate of north america. Research Data Archive at the National Center for

Atmospheric Research, Computational and Information Systems Laboratory, Boulder CO, URL https://doi.org/10.5065/D6V40SXP.

Rasmussen, R., and Coauthors, 2011: High-resolution coupled climate runoff simulations of seasonal snowfall over colorado: A process study of current and warmer climate. *Journal of Climate*, **24 (12)**, 3015 – 3048, https://doi.org/https://doi.org/10.1175/2010JCLI3985.1, URL https://journals.ametsoc.org/view/journals/clim/24/12/2010jcli3985.1.xml.

Reed, R. J., 1955: A study of a characteristic type of upper-level frontogenesis. *J. Meteorol.*, **12**, 226–237.

Roiger, A., and Coauthors, 2011: In-situ observation of asian pollution transported into the arctic lowermost stratosphere. *Atmospheric Chemistry and Physics*, **11 (21)**, 10 975–10 994, https://doi.org/10.5194/acp-11-10975-2011, URL https://acp.copernicus.org/articles/11/10975/2011/.

Santer, B. D., and Coauthors, 2003: Contributions of anthropogenic and natural forcing to recent tropopause height changes. *Science*, **301 (5632)**, 479–483, https://doi.org/10.1126/science.1084123.

Schwartz, M. J., G. L. Manney, M. I. Hegglin, N. J. Livesey, M. L. Santee, and W. H. Daffer, 2015: Climatology and variability of trace gases in extratropical double-tropopause regions from MLS, HIRDLS, and ACE-FTS measurements. *J. Geophys. Res. Atmos.*, **120**, 843–867, https://doi.org/10.1002/2014JD021964.

Schwartz, M. J., W. G. Read, M. L. Santee, N. J. Livesey, L. Froidevaux, A. Lambert, and G. L. Manney, 2013: Convectively injected water vapor in the north american summer lowermost stratosphere. *Geophysical Research Letters*, **40 (10)**, 2316–2321, https://doi.org/10.1002/grl.50421.

Seidel, D. J., and W. J. Randel, 2006: Variability and trends in the global tropopause estimated from radiosonde data. *J. Geophys. Res.*, **111**, D21 101, https://doi.org/10.1029/2006JD007363.

Seidel, D. J., R. J. Ross, J. K. Angell, and G. C. Reid, 2001: Climatological characteristics of the tropical tropopause as revealed by radiosondes. *J. Geophys. Res.*, **106 (D8)**, 7857–7878.

Shapiro, M. A., 1980: Turbulent mixing within tropopause folds as a mechanism for the exchange of chemical constituents between the stratosphere and troposphere. *J. Atmos. Sci.*, **37**, 994–1004.

Shepherd, T. G., 2002: Issues in stratosphere-troposphere coupling. *J. Meteorol. Soc. Japan*, **80 (4B)**, 769–792, https://doi.org/10.2151/jmsj.80.769.

Škerlak, B., M. Sprenger, and H. Wernli, 2014: A global climatology of stratosphere-troposphere exchange using the ERA-Interim data set from 1979 to 2011. *Atmos. Chem. Phys.*, **14**, 913–937, https://doi.org/10.5194/acp-14-913-2014.

Skofronick-Jackson, G., and Coauthors, 2017: The global precipitation measurement (gpm) mission for science and society. *Bulletin of the American Meteorological Society*, **98 (8)**, 1679 – 1695, https://doi.org/https://doi.org/10.1175/BAMS-D-15-00306.1, URL https://journals.ametsoc.org/view/journals/bams/98/8/bams-d-15-00306.1.xml.

Smith, J. B., and Coauthors, 2017: A case study of convectively sourced water vapor observed in the overworld stratosphere over the united states. *Journal of Geophysical Research: Atmospheres*, **122 (17)**, 9529–9554, https://doi.org/10.1002/2017JD026831.

Solomon, D. L., K. P. Bowman, and C. R. Homeyer, 2016: Tropopause-penetrating convection from three-dimensional gridded nexrad data. *Journal of Applied Meteorology and Climatology*, **55 (2)**, 465–478, https://doi.org/10.1175/JAMC-D-15-0190.1.

Solomon, S., K. H. Rosenlof, R. W. Portmann, J. S. Daniell, S. M. Davis, T. J. Sanford, and G.-K. Plattner, 2010: Contributions of stratospheric water vapor to decadal changes in the rate of global warming. *Science*, **327 (5970)**, 1219–1223, https://doi.org/10.1126/science.1182488.

Son, S.-W., and L. M. Polvani, 2007: Dynamical formation of an extra-tropical tropopause inversion layer in a relatively simple circulation model. *Geophys. Res. Lett.*, **34**, L17 806, https://doi.org/10.1029/2007GL030564.

Sprenger, M., M. C. Maspoli, and H. Wernli, 2003: Tropopause folds and cross-tropopause exchange: A global investigation based upon ECMWF analyses for the time period March 2000 to February 2001. *J. Geophys. Res.*, **108 (D12)**, 8518, https://doi.org/10.1029/2002JD002587.

Sterling, C. W., and Coauthors, 2018: Homogenizing and estimating the uncertainty in NOAA's long-term vertical ozone profile records measured with the electrochemical concentration cell ozonesonde. *Atmos. Meas. Tech.*, **11**, 3661–3687, https://doi.org/10.5194/amt-11-3661-2018.

Stohl, A., 2001: A 1-year lagrangian "climatology" of airstreams in the northern hemisphere troposphere and lowermost stratosphere. *Journal of Geophysical Research: Atmospheres*, **106 (D7)**, 7263–7279, https://doi.org/https://doi.org/10.1029/2000JD900570, URL https://agupubs.onlinelibrary.wiley.com/doi/abs/10.1029/2000JD900570, https://agupubs.onlinelibrary.wiley.com/doi/pdf/10.1029/2000JD900570.

Stohl, A., H. Wernli, P. James, M. Bourqui, C. Forster, M. A. Liniger, P. Seibert, and M. Sprenger, 2003: A new perspective of stratosphere-troposphere exchange. *Bull. Amer. Meteorol. Soc.*, **84 (11)**, 1565–1573.

Stohl, A., G. Wotawa, P. Seibert, and H. Kromp-Kolb, 1995: Interpolation errors in wind fields as a function of spatial and temporal resolution and their impact on different types of kinematic trajectories. *Journal of Applied Meteorology (1988-2005)*, **34 (10)**, 2149–2165, https://doi.org/10.1175/1520-0450(1995)034⟨2149:IEIWFA⟩2.0.CO;2.

Thompson, A. M., R. M. Stauffer, K. Wargan, J. C. Witte, D. E. Kollonige, and J. R. Ziemke, 2021: Regional and seasonal trends in tropical ozone from SHADOZ profiles: Reference for models and satellite products. *J. Geophys. Res. Atmos.*, **126**, e2021JD034 691, https://doi.org/10.1029/2021JD034691.

Thompson, A. M., and Coauthors, 2017: First reprocessing of southern hemisphere additional ozonesondes (SHADOZ) profile records (1998–2016): 2. comparisons with satellite and ground-based instruments. *J. Geophys. Res. Atmos.*, **122**, 13,000–13,025, https://doi.org/10.1002/2017JD027406.

Tilmes, S., and Coauthors, 2010: An aircraft-based upper troposphere and lower stratosphere O_3, CO, and H_2O climatology for the Northern Hemisphere. *J. Geophys. Res.*, **115**, D14 303, https://doi.org/10.1029/2009JD012731.

Tinney, E. N., and C. R. Homeyer, 2021: A 13-year trajectory-based analysis of convection-driven changes in upper troposphere lower stratosphere composition over the united states. *Journal of Geophysical Research: Atmospheres*, **126 (3)**, e2020JD033 657, https://doi.org/https://doi.org/10.1029/2020JD033657.

Tinney, E. N., and C. R. Homeyer, 2023: Climatology, sources, and transport characteristics of observed water vapor extrema in the lower stratosphere. *Atmospheric Chemistry and Physics*, **23 (22)**, 14 375–14 392, https://doi.org/10.5194/acp-23-14375-2023, URL https://acp.copernicus.org/articles/23/14375/2023/.

Tinney, E. N., C. R. Homeyer, L. Elizalde, D. F. Hurst, A. M. Thompson, R. M. Stauffer, H. Vömel, and H. B. Selkirk, 2022: A modern approach to a stability-based definition of the tropopause. *Monthly Weather Review*, **150 (12)**, 3151 – 3174, https://doi.org/https://doi.org/10.1175/MWR-D-22-0174.1, URL https://journals.ametsoc.org/view/journals/mwre/150/12/MWR-D-22-0174.1.xml.

Trapp, R. J., N. S. Diffenbaugh, and A. Gluhovsky, 2009: Transient response of severe thunderstorm forcing to elevated greenhouse gas concentrations. *Geophysical Research Letters*, **36 (1)**, https://doi.org/10.1029/2008GL036203.

Trapp, R. J., and K. A. Hoogewind, 2016: The realization of extreme tornadic storm events under future anthropogenic climate change. *Journal of Climate*, **29 (14)**, 5251–5265, https://doi.org/10.1175/JCLI-D-15-0623.1.

Ueyama, R., M. Schoeberl, E. Jensen, L. Pfister, M. Park, and J.-M. Ryoo, 2023: Convective impact on the global lower stratospheric water vapor budget. *Journal of Geophysical Research: Atmospheres*, **128 (6)**, e2022JD037 135, https://doi.org/https://doi.org/10.1029/2022JD037135, URL https://agupubs.onlinelibrary.wiley.com/doi/abs/10.1029/2022JD037135, e2022JD037135 2022JD037135, https://agupubs.onlinelibrary.wiley.com/doi/pdf/10.1029/2022JD037135.

Vaughan, G., and C. Timmis, 1998: Transport of near-tropopause air into the lower midlatitude stratosphere. *Q. J. R. Meteorol. Soc.*, **124**, 1559–1578.

Vincent, D. G., 1994: The south pacific convergence zone (spcz): A review. *Monthly Weather Review*, **122 (9)**, 1949 – 1970, https://doi.org/https://doi.org/10.1175/1520-0493(1994)122⟨1949:TSPCZA⟩2.0.CO;2, URL https://journals.ametsoc.org/view/journals/mwre/122/9/1520-0493_1994_122_1949_tspcza_2_0_co_2.xml.

Vömel, H., D. E. David, and K. Smith, 2007: Accuracy of tropospheric and stratospheric water vapor measurements by the cryogenic frost point hygrometer: Instrument details and observations. *J. Geophys. Res.*, **112**, D08 305, https://doi.org/10.1029/2006JD007224.

Vömel, H., T. Naebert, R. Dirksen, and M. Sommer, 2016: An update on the uncertainties of water vapor measurements using cryogenic frost point hygrometers. *Atmos. Meas. Tech.*, **9**, 3755–3768, https://doi.org/10.5194/amt-9-3755-2016.

Wang, S., and L. M. Polvani, 2011: Double tropopause formation in idealized baroclinic life cycles: The key role of an initial tropopause inversion layer. *J. Geophys. Res.*, **116**, D05 108, https://doi.org/10.1029/2010JD015118.

Wang, Y., H. Su, J. H. Jiang, N. J. Livesey, M. L. Santee, L. Froidevaux, W. G. Read, and J. Anderson, 2017: The linkage between stratospheric water vapor and surface temperature in an observation-constrained coupled general circulation model. *Climate Dynamics*, **48 (7)**, 2671–2683, https://doi.org/10.1007/s00382-016-3231-3, URL https://doi.org/10.1007/s00382-016-3231-3.

Weisman, M. L., W. C. Skamarock, and J. B. Klemp, 1997: The resolution dependence of explicitly modeled convective systems. *Monthly Weather Review*, **125 (4)**, 527–548, https://doi.org/10.1175/1520-0493(1997)125⟨0527:TRDOEM⟩2.0.CO;2.

Werner, F., M. J. Schwartz, N. J. Livesey, W. G. Read, and M. L. Santee, 2020: Extreme outliers in lower stratospheric water vapor over north america observed by mls: Relation to overshooting convection diagnosed from colocated aqua-modis data. *Geophysical Research Letters*, **47 (24)**, e2020GL090 131, https://doi.org/https://doi.org/10.1029/2020GL090131, URL https://agupubs.onlinelibrary.wiley.com/doi/abs/10.1029/2020GL090131, e2020GL090131 10.1029/2020GL090131, https://agupubs.onlinelibrary.wiley.com/doi/pdf/10.1029/2020GL090131.

Wernli, H., and M. Bourqui, 2002: A Lagrangian "1-year climatology" of (deep) cross-tropopause exchange in the extratropical Northern Hemisphere. *J. Geophys. Res.*, **107 (D2)**, 4021, https://doi.org/10.1029/2001JD000812.

Witte, J. C., A. M. Thompson, H. G. J. Smit, H. Vömel, F. Posny, and R. Stübi, 2018: First reprocessing of Southern Hemisphere ADditional OZonesondes profile records: 3. uncertainty in ozone profile and total column. *J. Geophys. Res. Atmos.*, **123**, 3243–3268, https://doi.org/10.1002/2017JD027791.

Witte, J. C., and Coauthors, 2017: First reprocessing of Southern Hemisphere ADditional OZonesondes (SHADOZ) profile records (1998–2015): 1. methodology and evaluation. *J. Geophys. Res. Atmos.*, **122**, 6611–6636, https://doi.org/10.1002/2016JD026403.

World Meteorological Organization, 1957: *A three-dimensional science: Second session of the commission for aerology.*

Xian, T., and C. R. Homeyer, 2019: Global tropopause altitudes in radiosondes and reanalyses. *Atmospheric Chemistry and Physics*, **19 (8)**, 5661–5678, https://doi.org/10.5194/acp-19-5661-2019.

Zahn, A., and C. A. M. Brenninkmeijer, 2003: New directions: A chemical tropopause defined. *Atmos. Environ.*, **37**, 439–440.

Zängl, G., and K. P. Hoinka, 2001: The tropopause in the polar regions. *J. Clim.*, **14**, 3117–3139.